

PARYLENE AS A NEW MEMBRANE MATERIAL FOR BIOMEMS APPLICATIONS

Thesis by

Bo Lu

In Partial Fulfillment of the Requirements
for the Degree of

Doctor of Philosophy



California Institute of Technology

Pasadena, California

2012

(Defended April 26th, 2012)

© 2012

Bo Lu

All Rights Reserved

Acknowledgements

All the work in this thesis would definitely not be possible without the remarkable guidance from my Ph.D. research advisor, Dr. Yu-Chong Tai. Frequently, I feel I have been so lucky to be able to work with him in the past five years at Caltech. He has taught me how to think and behave like a Ph.D. What I have learned from him is not only limited to research, but also includes many interpersonal skills. Whenever I got inspired and proposed new ideas, he gave me encouragement and strong support. Whenever I met difficulties, he helped me analyze the problem and find the solutions. Whenever I made a mistake, he was always very tolerant, pointing out my mistake first and then helping me correct it, patiently. I ought to give most credit to him for my research achievements so far, and for possibly more in the future.

I will never forget the tremendous help from all the previous and current members at Dr. Tai's Caltech MEMS Group, including the previous members Dr. Siyang Zheng, Dr. Changlin Pang, Dr. Wen Li, Dr. Po-Jui (PJ) Chen, Dr. Nick Lo, Dr. Jason Shih, Dr. Mike Liu, Dr. Quoc (Brandon) Quach, Dr. Ray Huang, Dr. Luca Giacchino, Dr. Jeffrey Chun-Hui Lin, Ms. Yingying Wang, and Mr. Zhao Liu, and the current group members Mandheerej (Monty) Nandra, Justin Young-Hyun Kim, Wendian Shi, Penvipha (Yok) Satsanarukkit, Jay Han-Chieh Chang, Yu Zhao, Charles DeBoer, Dongyang Kang, Yang Liu, Nick Scianmarello, and Shell Zhang. They are not only my colleagues but also my friends. I also appreciate our lab manager Trevor Roper and group assistant Christine

Garske. Without Trevor, the cleanroom would be down; without Christine, our group would be unorganized.

The multidisciplinary nature of my research enabled me to gain plenty of biological, medical, and surgical knowledge from my collaborators at the Norris Cancer Center and the Doheny Eye Institute of the University of Southern California. I would like to thank Dr. Mark S. Humayun, Dr. David Hinton, Dr. Biju Thomas, Dr. Amir Goldkorn, Dr. Tong Xu, Dr. Danhong Zhu, Ms. Laura Liu, Dr. Yuntao Hu, Dr. Jing Xu, and Mr. Kaijie He for their helps and suggestions on my research. I would also like to thank my friend, Mr. Kuang Shen from the Chemistry Department of Caltech, who helped me a lot on the material studies, as well as Mr. Guoan Zheng from Electrical Engineering of Caltech, who helped me a lot with the optics.

Moreover, I would like to thank my Ph.D. candidacy and defense committee members, including Dr. Changhuei Yang, Dr. Hyuck Choo, Dr. Joel W. Burdick, and Dr. Chin-Lin Guo.

I am deeply grateful to my parents, grandma, and uncle. They have always stood firmly with me and backed me up throughout my life. Last, but the most important, special thanks are due to my fiancée, Jie Zhu. Her love and support helped me overcome difficulties along the way.

Abstract

Parylene as a New Membrane Material for BioMEMS Applications

Thesis by

Bo Lu

Doctor of Philosophy in Electrical Engineering

California Institute of Technology

The work in this thesis aims to use MEMS and microfabrication technologies to develop two types of parylene membrane devices for biomedical applications. The first device is the parylene membrane filter for cancer detection. The presence of circulating tumor cells (CTC) in patient blood is an important sign of cancer metastasis. However, currently there are two big challenges for CTC detection. First, CTCs are extremely rare, especially at the early stage of cancer metastasis. Secondly, CTCs are very fragile, and are very likely to be damaged during the capturing process. By using size-based membrane filtration through the specially designed parylene filters, together with a constant-pressure filtration system, we are able to capture the CTCs from patient blood

with high capture efficiency, high viability, moderate enrichment, and high throughput. Both immunofluorescence enumeration and telomerase activity detection have been used to detect and differentiate the captured CTCs. The feasibility of further cell culture of the captured CTCs has also been demonstrated, which could be a useful way to increase the number of CTCs for future studies. Models of the time-dependent cell membrane damage are developed to predict and prevent CTC damage during this detection process. The results of clinical trials further demonstrate that the parylene membrane filter is a promising device for cancer detection.

The second device is the parylene artificial Bruch's membrane for age-related macular degeneration (AMD). AMD is usually characterized by an impaired Bruch's membrane with much lowered permeability, which impedes the transportation of nutrients from choroid vessels to nourish the retinal pigment epithelial (RPE) cells and photoreceptors. Parylene is selected as a substitute material because of its good mechanical properties, transparency, biocompatibility, and machinability. More importantly, it is found that the permeability of submicron parylene is very similar to that of healthy human Bruch's membrane. A mesh-supported submicron parylene membrane structure has been designed and its feasibility as an artificial Bruch's membrane has been demonstrated by diffusion experiments, cell perfusion culture, and pressure deflection tests. RPE cells are able to adhere, proliferate and develop into normal *in vivo*-like morphology and functions. Currently this artificial membrane is under clinical trials.

Table of Contents

Chapter 1: Introduction	1
1.1 Parylene: An Ideal Material for BioMEMS	1
1.2 Latest Achievements in Parylene BioMEMS.....	2
1.3 Parylene Membrane Devices.....	4
1.4 Parylene Processing Technologies	7
1.4.1 Parylene dry etching.....	8
1.4.2 Parylene adhesion consideration.....	9
1.4.3 Parylene molding technique.....	11
1.4.4 Parylene channel formation	12
1.4.5 Parylene fill-in technique.....	15
1.5 Layout of the Dissertation	16
1.6 References	16
Chapter 2: Characterizations of Parylene Membranes	19
2.1 Overview	19
2.2 Mechanical Characterization.....	20
2.2.1 A comparison of normal and ultrathin membranes.....	20
2.2.2 Strategy to enhance the strength of ultrathin membrane.....	21
2.3 Semipermeability of Submicron Parylene Membranes.....	22
2.3.1 Measurements of the diffusion coefficients	23
2.3.2 Molecular weight/radius exclusion limits	26
2.4 Parylene Autofluorescence.....	27
2.4.1 Motivation.....	27
2.4.2 Comparisons of parylene with other polymers/plastics	29
2.4.3 Autofluorescence behaviors during UV illumination	32
2.4.4 The mechanism of autofluorescence in parylene-C/D/N films.....	36

2.4.5	Parylene-HT: A better choice for autofluorescence concerns	41
2.4.6	Autofluorescence induced in microfabrication process	43
2.5	Hydrophilic and Hydrophobic Parylene Membranes	45
2.5.1	The importance of surface hydrophilicity/hydrophobicity	45
2.5.2	Plasma treatments and their effects on parylene surfaces	46
2.5.3	Superhydrophobic parylene membrane	48
2.6	Summary	54
2.7	References	54
Chapter 3:	Parylene Membrane Filters for Cancer Detection	59
3.1	Overview	59
3.2	Current Technologies for CTC Detection	61
3.2.1	Enriching methods	61
3.2.2	Detection methods	64
3.3	Parylene Membrane Filters	65
3.3.1	Parylene: An ideal membrane filter material	65
3.3.2	1 st generation: 2D pore filter	66
3.3.3	2 nd generation: 3D pore filter	68
3.3.4	3 rd generation: 3D gap filter	72
3.3.5	4 th generation: 2D slot filter	77
3.4	Experiment Results and Clinical Trials	81
3.4.1	Immunofluorescence method	81
3.4.2	Telomerase activity detection	84
3.5	Discussion: Further Optimizations	88
3.5.1	Enrichment improvement	88
3.5.2	Sensitivity improvement	89
3.5.3	Viability improvement	90
3.5.4	Throughput improvement	91

3.6	CTC Culture After Capture	91
3.7	A Biomechanical Study of Cell Membrane Damage	97
3.7.1	Motivation.....	97
3.7.2	Experiment approach	98
3.7.3	Cell modeling.....	99
3.7.4	Simulation	100
3.7.5	Time-dependent viability drop.....	101
3.7.6	Molecular membrane failure model.....	103
3.7.7	Griffith’s membrane failure model	105
3.7.8	Comparison of models	107
3.7.9	Prediction of the safe “golden zone”.....	108
3.8	Summary	109
3.9	References	110
Chapter 4:	Parylene Artificial Bruch’s Membrane	115
4.1	Overview	115
4.2	Existing Therapies for AMD	117
4.3	Parylene Artificial Bruch’s Membrane.....	118
4.3.1	Submicron parylene: A potential candidate	118
4.3.2	Perfusion cell-culture experiments.....	120
4.3.3	Mesh-supported submicron parylene.....	122
4.3.4	Mechanical optimization.....	124
4.3.5	RPE cell culture on the MSPM.....	126
4.3.6	Comparison of MSPM and porous membrane.....	128
4.4	Animal Trials.....	130
4.4.1	The “lollipop” design.....	130
4.4.2	Mechanical implantation platform.....	131
4.4.3	Microfluidic implantation tool.....	133

4.4.4	Post-implantation staining and imaging.....	136
4.5	RPE Cage.....	137
4.5.1	Motivation.....	137
4.5.2	Cage design and fabrication.....	138
4.5.3	Cage assembling	141
4.5.4	Preliminary results	142
4.6	Summary	143
4.7	References.....	144
Chapter 5:	Conclusions	147

List of Figures

Figure 1-1: Chemical structures of major members in the parylene family	2
Figure 1-2: Gold coated parylene membrane with gratings for SPR application	5
Figure 1-3: The concept and operation method of the parylene-based cell origami ...	6
Figure 1-4: The concept and operation procedure of the selective patterning of cells or proteins using parylene membranes as peeling masks	7
Figure 1-5: Parylene molding technique used in forming a parylene membrane with gratings for SPR application.....	11
Figure 1-6: Parylene molding technique for superhydrophobic films	12
Figure 1-7: Fabrication process flow of surface-micromachined parylene channels with sacrificial photoresist.....	13
Figure 1-8: The fabrication process of an embedded parylene channel	14
Figure 1-9: Illustration of the parylene fill-in process	15
Figure 2-1: Stress-strain curves of parylene films with different thicknesses, measured by DMA at room temperature	20
Figure 2-2: (a) The membrane deflection test setup; (b) Uniform submicron parylene is broken at a low pressure load; (c) The composited membrane is broken at a much higher pressure load.....	22
Figure 2-3: Schematic of the diffusivity measurement with blind-well chambers ...	24
Figure 2-4: Diffusion coefficients of dextran molecules in submicron parylene-C membranes with different thicknesses.....	25
Figure 2-5: Molecular weight exclusion limits of submicron parylene-C	26

Figure 2-6: Strong autofluorescence in parylene-C based dual-layer membrane CTC microfilter	28
Figure 2-7: Structure of parylene-C, -D, -N, -HT films	29
Figure 2-8: Comparisons of relative initial autofluorescence intensities of parylene-C with other polymers and plastics	31
Figure 2-9: Enhanced blue, green, and red autofluorescence of parylene-C film after 2 minutes short-time UV illumination.....	33
Figure 2-10: Quantitative fluorescence intensity variations of parylene films during continuous short-time UV illumination.....	34
Figure 2-11: Quantitative blue fluorescence intensity variations of parylene films during continuous long-time UV illumination	36
Figure 2-12: Fluorescence spectra of parylene-C film, under 280 nm excitation, measured by fluorimeter.....	38
Figure 2-13: Infrared spectra of parylene-C film	38
Figure 2-14: Fluorescence spectra of parylene-HT dimer and film	42
Figure 2-15: Comparisons of autofluorescence of unpatterned parylene-C film and parylene-C based devices	44
Figure 2-16: The effects of fluorine plasma treatment.....	47
Figure 2-17: AFM evaluation of the rms surface roughness	48
Figure 2-18: Fabrication process of two types of superhydrophobic films.....	50
Figure 2-19: SEM images of the superhydrophobic films	50
Figure 2-20: Water droplet on a superhydrophobic film (lotus leaf).....	51
Figure 2-21: Water droplet on a superhydrophobic film (rose petal).....	52

Figure 2-22: Advantages of parylene superhydrophobic film.....	53
Figure 3-1: SEM images of 2D pore filters.....	67
Figure 3-2: Cells were partially damaged or totally lysed after filtration.....	68
Figure 3-3: 3D pore filter design.....	69
Figure 3-4: Fabrication process flow of the 3D pore filter.....	69
Figure 3-5: Photos of the fabricated 3D microfilter.....	70
Figure 3-6: Device is assembled inside a housing cassette.....	70
Figure 3-7: Comparison of 2D and 3D filters with unfixed MCF-7 cells.....	71
Figure 3-8: SEM image of a MCF-7 cell captured on the 3D pore filter.....	72
Figure 3-9: Comparison of “pore capture” and “gap capture” mechanisms.....	73
Figure 3-10: Fabrication process flow of the 3D gap filter.....	73
Figure 3-11: Photos of the 3D gap filter.....	74
Figure 3-12: Filtration setup using constant pressure driving.....	74
Figure 3-13: Fluorescent image of a model system testing.....	75
Figure 3-14: Release of trapped tumor cells from filter using a brush.....	76
Figure 3-15: The low enrichment of the 3D pore filter.....	77
Figure 3-16: Constant-pressure-driven filtration system, the filter assembly, and the SEM image of fabricated slot filter.....	78
Figure 3-17: 2D slot filter characterization.....	80
Figure 3-18: Cancer cells captured on the slot filter.....	80
Figure 3-19: On-filter immunofluorescence staining of captured CTCs.....	83
Figure 3-20: Histogram demonstrating performance comparison of membrane	

microfilter vs. CellSearch® assay in clinical samples	84
Figure 3-21: Detection of telomerase activity from live cancer cells captured on a slot microfilter	85
Figure 3-22: Single-cell telomerase measurement	87
Figure 3-23: CTC filtration and enumeration experiments with parylene-C and parylene-HT membrane filters	89
Figure 3-24: On-filter (a) and off-filter (b) cell culture of captured PC-3 cells from human blood after 3 days and 6 days in RPMI complete medium.....	92
Figure 3-25: Parylene surface treatments and their influences on cell adherence	93
Figure 3-26: Parylene-C/HT filter fabrication process.....	94
Figure 3-27: Operation procedure of 3D on-filter culture.....	95
Figure 3-28: 3D on-filter cultured tumor growth rate and viability	96
Figure 3-29: Immuno-staining of cultured 3D tumor.....	96
Figure 3-30: Cortical-shell/liquid-core model of a cell captured on a slot	99
Figure 3-31: COMSOL simulation results	101
Figure 3-32: Time-dependent viability drop at different drive pressures.....	102
Figure 3-33: Schematic of nanopore formation in lipid bilayer membrane	104
Figure 3-34: Relations between the mean cell lysis time τ and the membrane tension σ for (a) the molecular membrane failure model and (b) the Griffith's membrane failure model.....	106
Figure 3-35: The safe “golden zones” predicted by (a) the molecular membrane failure model and (b) the Griffith's membrane failure model	109
Figure 4-1: Schematics of the Bruch's membrane and RPE cells.....	116

Figure 4-2: Comparisons of the permeability of submicron parylene, human Bruch's membranes, lens capsule and collagen film in terms of the diffusion flux	119
Figure 4-3: Perfusion cell viability tests.....	121
Figure 4-4: Fabrication process of the MSPM	122
Figure 4-5: SEM images of (a) the front side, (b) the back side, and (c) the cross section of a MSPM with 0.30 μm ultrathin parylene	123
Figure 4-6: Membrane deflection experiment.....	124
Figure 4-7: A wrinkled MSPM (a) and a broken MSPM (b).....	125
Figure 4-8: Yielding pressures and breakdown pressures for different MSPMs.....	125
Figure 4-9: H9-RPE cell culture on the MSPM	127
Figure 4-10: Porous parylene substrate with through holes (1 μm in diameter).....	129
Figure 4-11: Comparisons of morphologies of RPE cells on different substrates ..	129
Figure 4-12: Current designs of rat's and pig's lollipops and their dimensions.....	131
Figure 4-13: Diagrammatic sketch of the implantation tool	132
Figure 4-14: Fabrication process flow of the microfluidic implantation tool	134
Figure 4-15: The microfluidic implantation tool.....	134
Figure 4-16: Implantation of a lollipop device into a rat's eye	135
Figure 4-17: Hematoxylin-eosin staining one week after implantation	136
Figure 4-18: Immunofluorescence staining of the of RPE cells	136
Figure 4-19: The concept of the RPE cage.....	138
Figure 4-20: Cell migration experiments. The inset shows the transwell setup.....	139
Figure 4-21: Fabrication process flow of the cage's top cover	140

Figure 4-22: SEM image of the cover and a close-up view of the opening	140
Figure 4-23: The assembling and operation procedure of the cage for in vitro cell culture.....	141
Figure 4-24: RPE cell culture experiments inside the 3D cage.....	142

List of Tables

Table 1-1: Percentage of papers related to parylene in recent conferences.....	3
Table 2-1: Comparison of the mechanical strength between the uniform submicron parylene membrane and the composited membrane	22
Table 2-2: Molecular radius exclusion limits of submicron parylene-C membranes	27
Table 3-1: Comparisons of various CTC enriching technologies	64
Table 3-2: Capture efficiency with different gap sizes.....	76
Table 3-3: Comparison of 2D slot filters with different open factors	88
Table 3-4: Fitting parameters of experimental data in our work on cancer cells by filtration, Rand's work on RBCs by micropipette aspiration, and Taupin's work on RBCs by osmotic expansion.....	108

CHAPTER 1

INTRODUCTION

1.1 Parylene: An Ideal Material for BioMEMS

Parylene is the tradename for a variety of poly(p-xylylene) polymers. Fig. 1-1 shows the chemical structures of the major members in the parylene family. Among them, parylene-C is the most popular choice in various applications. In recent years, parylene-C has become a widely used material in the BioMEMS field. As a biocompatible polymer with the highest USP (U.S. Pharmacopeia) class VI approval, parylene-C has found numerous applications in cell sorting and manipulation, microfluidics, biomedical microdevices, and bioimplantable devices. This mechanically strong and flexible material has a Young's modulus of 2.8–4 GPa and high malleability that can withstand up to 200% elongation. Its high chemical resistance is also desirable

as a microfluidics and μ TAS chip material. It is optically transparent in the visible light range, which enables optical detection. More importantly, parylene-C has the unique feature of room-temperature, pinhole-free conformal chemical vapor deposition (CVD). It is machinable by MEMS-compatible fabrication technologies, and can be dry etched with oxygen plasma. These attractive properties make parylene-C an increasingly popular choice in building BioMEMS devices. Most of this dissertation is related to parylene-C. Unless specially pointed out, parylene-C will be abbreviated as parylene. However, there will be a section discussing other parylenes, including parylene-D, parylene-N, and parylene-HT (Section 2.4).

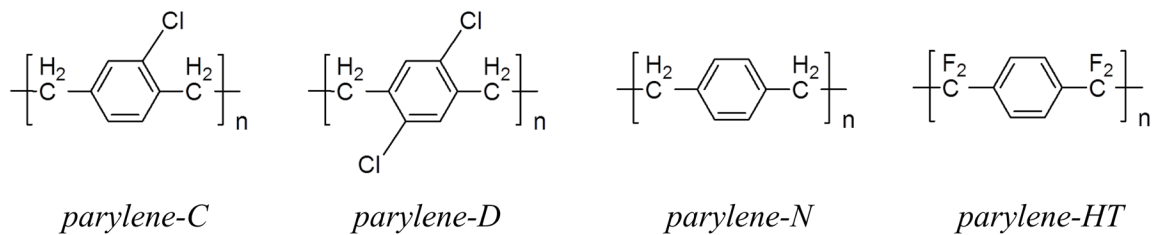


Figure 1-1: Chemical structures of major members in the parylene family

1.2 Latest Achievements in Parylene BioMEMS

Recently, in the most prestigious conferences in the MEMS field (MEMS and Transducers international conferences and Hilton Head workshop), a large percentage of papers (9%–15%) were related to the use of parylene (Table 1-1). Most of these papers were for biomedical applications. For example, in the latest MEMS 2012 conference, 52 out of 346 papers reported on devices using parylene as substrates, structural layers or protective coatings. For neural applications, Yu et al. reported parylene-coated nickel microprobes with parylene cables [1]. Yen et al. presented a pneumatic neural probe

fabricated by parylene thermal bonding technique [2]. Kim et al. showed a parylene-based electrochemical force sensor array for assessing neural probe insertion mechanics [3]. Parylene was also used in cell handling and manipulation. For example, a 3D parylene cage was used to culture retinal pigment epithelial cells for the stem-cell therapy of age-related macular degeneration [4]. A very interesting cell origami technique was based on the self-folding of the parylene substrates caused by cell traction force [5]. A parylene sensor encased inside a soft hydrogel contact lens was presented for the monitoring of tear glucose [6]. Johnson et al. reported a fully batch-fabricated cochlear array, which included a self-curing parylene substrate and a parylene ringed-channel, for cochlear prostheses to restore hearing [7]. Silicone oil and parylene film coating were adopted in the packaging process to create a sensor which was able to directly measure the breathing characteristics at the air passage in mice [8]. A parylene-based high-density packaging technique was used to integrate the IC chip with a parylene cable for a retinal prosthesis [9].

Table 1-1: Percentage of papers related to parylene in recent prestigious conferences

	<i>Total paper number</i>	<i>Papers related to parylene</i>	<i>Total appearance of "parylene"</i>	<i>Percentage of papers related to parylene</i>
<i>MEMS 2012</i>	346	52	649	15.0%
<i>Transducers 2011</i>	739	69	837	9.3%
<i>MEMS 2011</i>	346	39	462	11.3%
<i>Hilton Head 2010</i>	132	13	166	9.8%

From the observations at the MEMS 2012 conference, it can be seen that parylene-based devices have already found many applications in various biomedical fields. Novel therapies employing parylene devices are advantageous in many aspects compared to the traditional therapies, including their small volume, high efficiency, high integration, flexibility, and low cost.

1.3 Parylene Membrane Devices

Although there are many types of parylene-based membrane devices, in most cases, parylene is used as a protective coating layer, an encapsulation, a supporting layer, the microfluidic channel wall or a flexible substrate for other components. A parylene membrane device is usually defined to be a device made of a free-standing parylene membrane as the major structural layer. To date, the number of such parylene membrane devices is still very limited. Three types of parylene membrane devices will be introduced in this section.

The first example is a gold-coated parylene grating for the surface plasmon resonance (SPR) coupling and scanning (Fig. 1-2) [10], which can be used for molecule sensing. The grating patterns on the parylene membrane were created with the parylene molding technique. Briefly, e-beam lithography was first used to create the fine patterns of gratings on a silicon substrate, followed by parylene deposition on this silicon mold. Another silicon wafer with a central opening and surface parylene coating was bonded to the parylene-coated silicon mold under high pressure at 160°C. After removing the e-beam photoresist and releasing the silicon mold, a free-standing parylene membrane with replicated grating patterns was formed on a silicon frame. The parylene grating surface

was further coated with gold. By loading the pressure from the cavity underneath, the pitch of the grating changed accordingly. Besides the SPR application described in this paper, this type of device may also be used as a pressure sensor with high sensitivity. By measuring the laser spot movement when the membrane is deflected under pressure loading, the pressure can be calibrated and calculated.

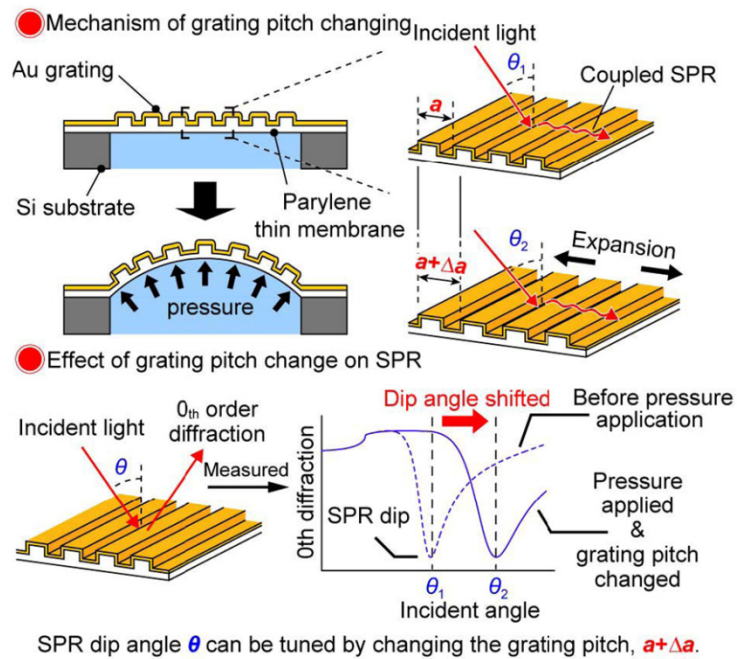


Figure 1-2: Gold coated parylene membrane with gratings for SPR application [10]

The next example is a self-folding cell origami (Fig. 1-3) [5]. It is generally believed that when cells are adhering and growing on a flexible substrate, the traction force of the cells can stretch and deform the underlying substrate. This substrate consisted of many small rigid plates and flexible joint hinges connecting the plates. The bottom was a parylene layer. Photolithography was used to create many SU-8

microplates on the bottom parylene, followed by the second parylene deposition and selective dry etching to pattern the parylene. The parylene-SU-8-parylene sandwich structures provided many local small rigid plates, which would be the structural layers in the origami. The joint connections contained only parylene, making them flexible; they served as the hinge later on. Fibronectin (FN) coating was performed prior to the cell seeding. During the proliferation of cells, the traction force caused the deformation of the hinges, resulting in the 3D construction of the microplates.

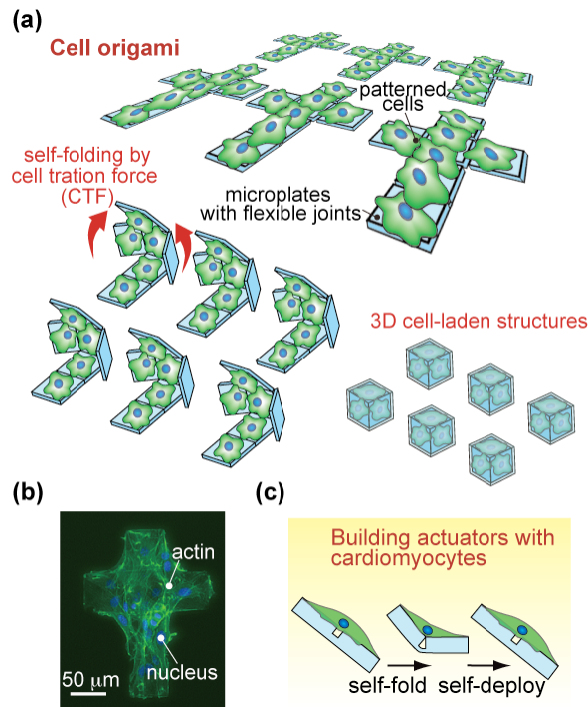


Figure 1-3: The concept and operation method of the parylene-based cell origami [5]

The last example uses parylene as peeling masks for the selective patterning of cells and proteins (Fig. 1-4) [11,12]. Parylene was deposited onto a silicon substrate layer by layer and etched into different patterns with through holes. The interface between two parylene layers was treated with microdetergent to reduce their adhesion.

Various cells or proteins were loaded onto the surface of the parylene. After peeling off the parylene membrane, the cells or proteins previously loaded into the wells were left, while the parts loaded on the parylene membrane were removed. By repeating this loading-peeling process, cells and proteins were finally selectively patterned on the designated regions on the substrate. It was claimed that these parylene membranes were reusable. This technique is very helpful in forming co-culture of different types of cells in designated regions.

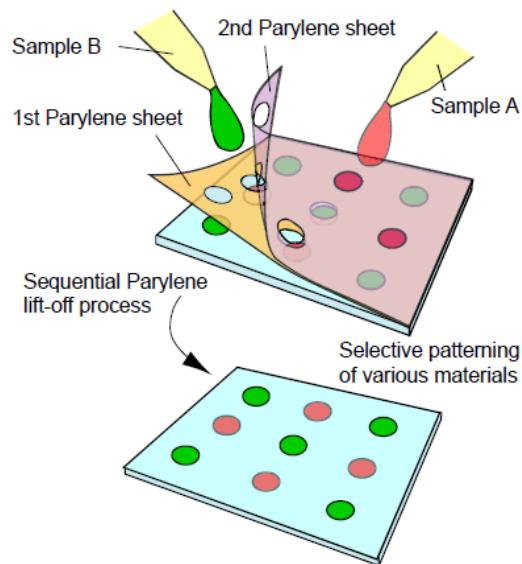


Figure 1-4: The concept and operation procedure of the selective patterning of cells or proteins using parylene membranes as peeling masks [11]

1.4 Parylene Processing Technologies

Compared to other polymers or plastics, one advantage of parylene is its machinability. MEMS fabrication technologies are generally applicable to the fabrication of parylene-based devices. A detailed description of general MEMS processing

technologies can be found in [13]. In this section, our primary goal is to introduce, review and discuss some fabrication technologies specific to parylene devices. Some of these technologies have been practiced and used in the fabrication of parylene membrane biomedical devices in the following chapters.

1.4.1 Parylene dry etching

Since parylene is inert to most chemical reagents, oxygen plasma dry etching is usually used to pattern parylene. Photoresist is the most commonly used mask for parylene dry etching. The etching rate ratio between parylene and AZ-series photoresist is 1:1.6 for soft-baked only photoresist. To etch thick parylene exceeding 10 μm , aluminum can be used as an alternative long-lasting mask. Moreover, sometimes if the pattern dimension is relatively small compared to the parylene thickness, a metal mask may be necessary. An example is given for etching an 8 μm diameter circular through-hole in 10 μm thick parylene. If using photoresist as the etching mask, given the selective ratio provided above, the photoresist layer should be thicker than 16 μm . However, patterning an 8 μm diameter hole in 16 μm thick photoresist is a difficult task that is beyond most university cleanrooms' capability. Alternatively, 1500–2000 \AA aluminum is good enough as a mask for the removal of parylene. Only a thin photoresist is required to transfer the mask pattern onto the aluminum layer through lithography and wet etching.

Plasma etching, reactive ion etching (RIE) and deep reactive ion etching (DRIE) are three choices for parylene removal. In plasma etching, the vertical and lateral etching rates are similar, resulting in an isotropic profile. For fine patterns with critical side-wall

profile, RIE is the preferred choice. When using 400 W and 200 mTorr as the settings in RIE, the vertical etching rate is about four times that of the lateral etching rate [14]. Decreasing the pressure can increase the mean-free path of electrons and ions, thus increasing the anisotropy. However, this increase in aspect ratio is at the expense of reducing the etching rate. The etching rate can be enhanced if a mixture of gas, rather than pure O_2 , is used as the plasma source. For example, adding CF_4 to O_2 is thought to increase oxygen atom concentration compared to pure O_2 plasma and to increase the etching rate, or to produce HF and leave unsaturated or radical sites for oxygen attack [14].

If pure O_2 plasma is used for DRIE, the etching profile is similar to that of RIE. However, DRIE can greatly increase the aspect ratio by using switched chemical etching [14]. For chemical-switching DRIE, in each loop, C_4F_8 plasma first deposits a fluorocarbon passivation layer on the bottom and side walls of a trench. The bottom passivation layer is then removed by the bombardment of argon plasma. Finally, O_2 plasma is able to etch only the bottom parylene of the trench, resulting in a combinatory effect of high-aspect-ratio parylene etching.

1.4.2 Parylene adhesion consideration

The study of adhesion of parylene to silicon, parylene to parylene, and parylene to other materials (such as SU-8) are of great importance. It is generally believed that parylene deposited on a hydrophobic surface shows good adhesion, while having poor adhesion on a hydrophilic surface. Poor adhesion is undesirable during device fabrication, because the parylene-to-silicon interface can easily be delaminated by

chemical attacks. However, for most parylene membrane devices requiring a free-standing parylene membrane, the last step of the process flow is often peeling the parylene from the substrate, in which case poor adhesion is clearly preferable.

There are several methods that can enhance the adhesion between parylene and silicon. Some chemicals, such as A-174 (provided by the Specialty Coating Systems), are designed to enhance adhesion by chemical methods. It has also been found that parylene shows better adhesion on a rougher surface. A roughened surface or anchoring designs both contribute to enhanced adhesion [15].

Parylene shows poor adhesion on oxidized silicon surface due to its surface hydrophilicity. Hexamethyldisiloxane (HMDS) is the most frequently used chemical to reduce parylene-to-silicon adhesion. It is believed the poor adhesion results from the weak Van der Waals force. Microdetergent or soap can also effectively reduce parylene-to-silicon adhesion.

Propylene carbonate coating has been found to be the most promising treatment for enhancing parylene-to-parylene adhesion [16]. Microdetergent or soap also works on the poor adhesion between two parylene layers, as demonstrated in the previous example using a parylene peeling mask for selective patterning [11,12]. A moderate parylene-to-parylene adhesion is achieved by buffered HF cleaning prior to the second parylene deposition. This moderate adhesion ensures that no parylene delamination will happen during the fabrication process, but that the parylene layers can be easily detached later on by mechanical force [17].

A parylene/SU-8 hybrid structure is frequently used in microfluidics and other applications. The adhesion between parylene and SU-8 greatly depends on the baking

protocol used for the SU-8. A long-time hard bake of SU-8 can enhance the adhesion and ensure there is no leakage of the channel even when high fluid pressure is applied. On the contrary, in the absence of the hard-bake step, SU-8 can easily be peeled off from parylene. This poor adhesion has also found its application in the SU-8 peeling mask for dry lift-off metallization on parylene [18].

1.4.3 Parylene molding technique

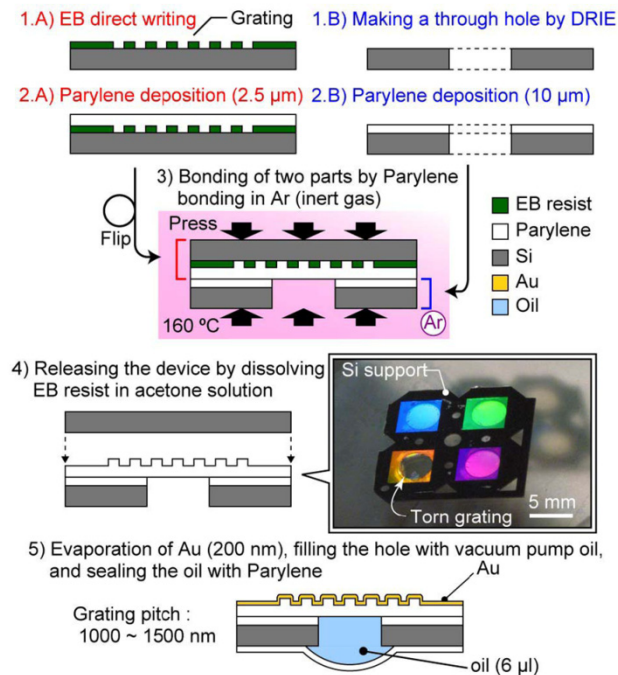


Figure 1-5: Parylene molding technique used in forming a parylene membrane with gratings for SPR application [10]

Parylene molding technique can be used to create parylene replicas from a silicon mold. In the previous example shown in [10], the grating patterns on parylene were formed by this replication process from a silicon mold (Fig. 1-5). Due to its conformal

coating property, parylene reproduced the fine features on the silicon substrate with e-beam photoresist. After dissolving the e-beam photoresist in acetone, the grating patterns were transferred onto the parylene membrane.

Another example of the parylene molding technique is the fabrication of parylene superhydrophobic films [19]. Micropillars were first created on silicon wafer by DRIE. HMDS was applied onto the silicon mold to reduce the adhesion between parylene and silicon. Parylene was then coated onto the silicon mold. After several other steps, the film was peeled off from the substrate, with an exact replica of the mold. The SEM images show that there was no damage observable during this molding and peeling process.

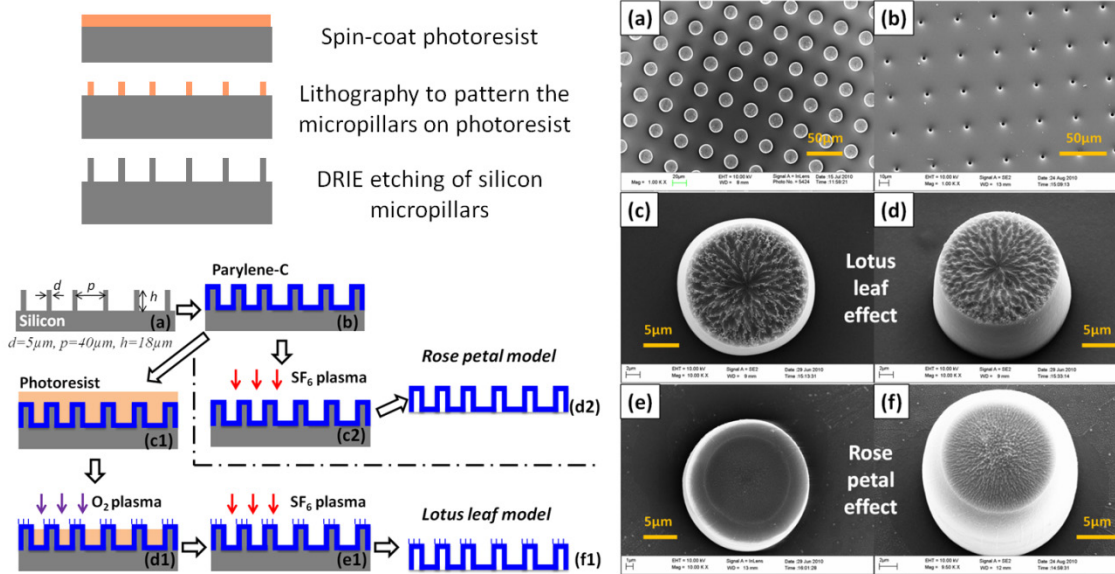


Figure 1-6: Parylene molding technique for the fabrication of superhydrophobic films [19]

1.4.4 Parylene channel formation

As a popular material in microfluidics, parylene channel formation is of great interest. In this section, two kinds of parylene channels will be introduced. The first type of parylene channel is formed by micromachining technologies with sacrificial photoresist layers. An example is shown in Fig. 1-7 [20]. Briefly, the fabrication process started with the bottom parylene deposition, followed by the sacrificial photoresist patterning. The second parylene was deposited and patterned by RIE. For multilayer channel applications, a second sacrificial photoresist was patterned. After the third parylene deposition and patterning, SU-8 is used to strengthen the channels. Following the patterning of the inlet/outlet, sacrificial photoresist was released to finish the parylene channel.

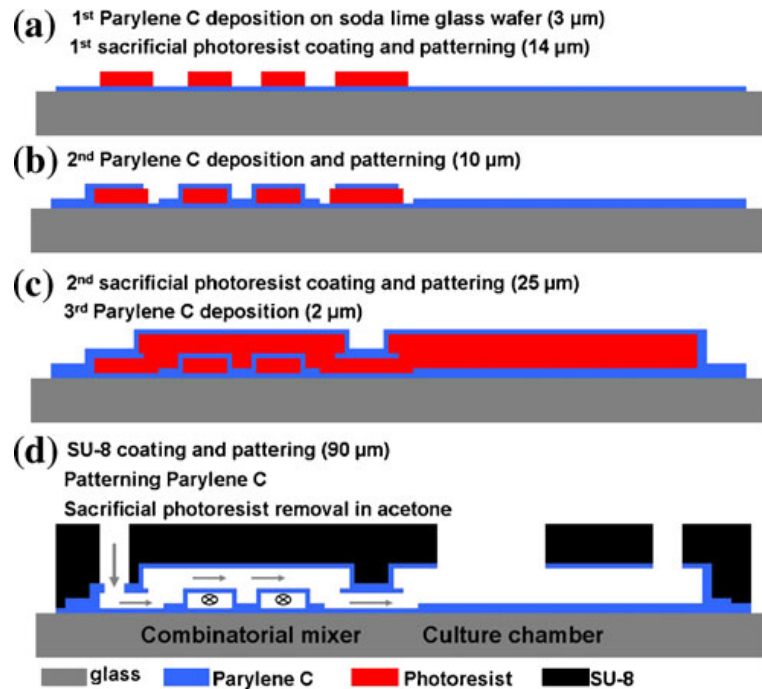


Figure 1-7: Fabrication process flow of surface-micromachined parylene channels with sacrificial photoresist [20]

One problem with the surface micromachined parylene channel is that a supporting layer, such as SU-8, is required to flatten the channel surface. Without this flattening layer, it is hard to couple inlets/outlets to outside flow sources.

Another type of parylene channel is the embedded channel [21]. Fig. 1-8 (a) shows the design and fabrication of the embedded channel. The process started with growing a 0.5 μm thermal oxide on a silicon wafer. Through a photoresist mask, the oxide was patterned by using buffered HF to define layout of the channels. After oxide patterning, xenon difluoride (XeF_2) was used to isotropically etch exposed silicon. Finally, a parylene layer was conformally deposited on the wafer. The parylene coating completely sealed the oxide opening on top of the etched cavities so that embedded channels were formed. Fig. 1-8(b) shows the fabricated single-mask, single-layer, quasi-hemi-circular monolithic embedded parylene channel.

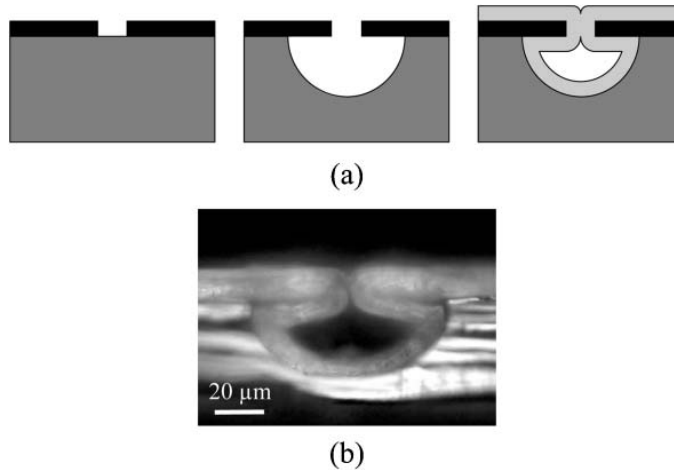


Figure 1-8: The fabrication process of an embedded parylene channel [21]

1.4.5 Parylene fill-in technique

Parylene membranes with through holes have wide applications in the BioMEMS field. Some applications require small holes with diameter down to 1 μm , or even into the submicron range. In these cases, direct etching of the holes is very difficult. An alternative method to form such small holes in a parylene layer is called the parylene fill-in technique. The fabrication process is very straightforward and illustrated in Fig. 1-9. The conformal coating property of parylene ensures the good edge profile of the filled-in holes. An example of this fill-in technique is the parylene nanopore for stable planar lipid bilayer membranes [22], where an 800 nm-diameter pore was created in a parylene layer.

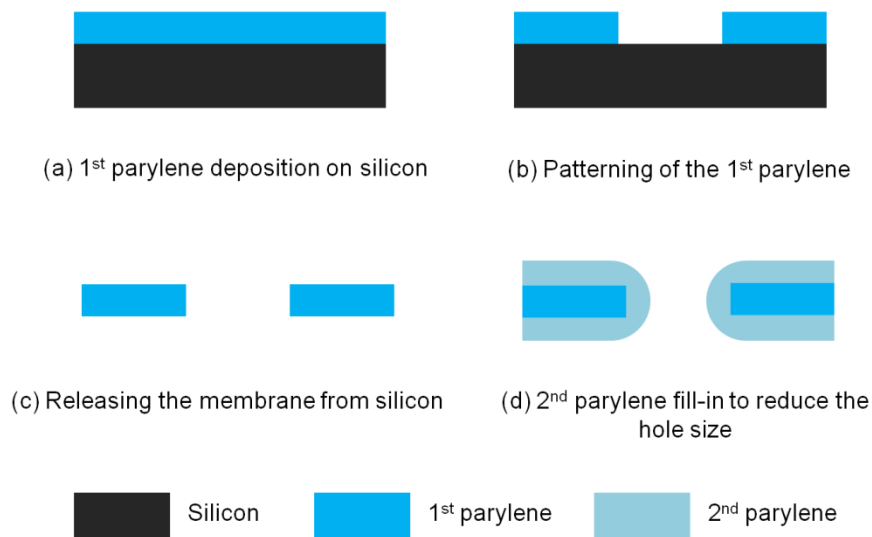


Figure 1-9: Illustration of the parylene fill-in process

1.5 Layout of the Dissertation

My dissertation focuses on the design, fabrication, testing, and applications of parylene membrane devices. In Chapter 1, after a brief introduction of parylene BioMEMS devices, the concept of parylene membrane devices is defined and three examples of membrane devices are discussed. The major fabrication processes and techniques for working with parylene membrane devices are then briefly reviewed. Without deep understanding of the properties of parylene itself, no parylene devices can be successful. Therefore, Chapter 2 will focus on the material studies of parylene, including its mechanical properties, permeability, autofluorescence, and surface hydrophobicity. The material properties studied in Chapter 2 will provide solid support to the discussion of devices in the following chapters. In Chapter 3 and Chapter 4, two kinds of parylene membrane devices — parylene membrane filters for cancer detection and parylene artificial Bruch's membrane for age-related macular degeneration, will be described and discussed in detail. Conclusions and future works will be included in Chapter 5.

1.6 References

- [1] H. Yu, S. Wang, W. Wang and Z. Li, Fabrication of electroplated nickel multielectrode microprobes with flexible parylene cable, *Proc. of MEMS 2012*, Paris, France, 2012, pp. 239–242
- [2] Y.C. Yen, Y.T. Lee, Y.C. Chang and W. Fang, A pneumatic neural probe structure fabricated by parylene thermal bonding technique, *Proc. of MEMS 2012*, Paris, France, 2012, pp. 381–384

- [3] B.J. Kim, C.A. Gutierrez, G.A. Gerhardt and E. Meng, Parylene-based electrochemical-MEMS force sensor array for assessing neural probe insertion mechanics, *Proc. of MEMS 2012*, Paris, France, 2012, pp. 124–127
- [4] B. Lu, D. Zhu, D. Hinton, M.S. Humayun and Y.C. Tai, A 3D parylene scaffold cage for culturing retinal pigment epithelial cells, *Proc. of MEMS 2012*, Paris, France, 2012, pp. 741–744
- [5] K. Kuribayashi-Shigetomi, H. Onoe and S. Takeuchi, Self-folding cell origami: batch process of self-folding 3D cell-laden microstructures actuated by cell traction force, *Proc. of MEMS 2012*, Paris, France, 2012, pp. 72–75
- [6] H. Yao, C. Marcheselli, A. Afanasiev, I. Lahdesmaki and B.A. Parviz, A soft hydrogel contact lens with an encapsulated sensor for tear glucose monitoring, *Proc. of MEMS 2012*, Paris, France, 2012, pp. 769–772
- [7] A.C. Johnson and K.D. Wise, A self-curling monolithically-backed active high-density cochlear electrode array, *Proc. of MEMS 2012*, Paris, France, 2012, pp. 914–917
- [8] T. Shikano, M. Shikano, M. Matsushima, T. Kawabe and K. Sato, Measurement of breathing characteristic in mouse during inhaling drug, *Proc. of MEMS 2012*, Paris, France, 2012, pp. 969–972
- [9] J.H.C. Chang, D. Kang and Y.C. Tai, High yield packaging for high-density multi-channel chip integration on flexible parylene substrate, *Proc. of MEMS 2012*, Paris, France, 2012, pp. 353–356
- [10] T. Kan, K. Matsumoto and I. Shimoyama, Tunable SPR coupler by flexible polymer grating, *Proc. of MEMS 2008*, Tucson, AZ, USA, 2008, pp. 774–777
- [11] K. Kuribayashi, Y. Hiratsuka, T. Yamamura and S. Yakeuchi, Sequential parylene lift-off process for selective patterning of biological materials, *Proc. of MEMS 2007*, Kobe, Japan, 2007, pp. 501–504
- [12] C.L. Chen, S. Jinno, H. Moller, B. Rajalingam, S.H. Chao, S. Selvarasah, A. Khademhosseini and M.R. Dokmeci, Multilayer parylene-C stencils for dynamically controlling cell interactions, *Proc. of MEMS 2008*, Tucson, AZ, USA, 2008, pp. 276–279

- [13] L. Giacchino, MEMS electrolytic inchworms for movable neural probe applications, Ph. D. Thesis, California Institute of Technology, 2011
- [14] E. Meng, P.Y. Li and Y.C. Tai, Plasma removal of parylene-C, *Journal of Micromechanics and Microengineering*, vol. 18, pp. 045004, 2008
- [15] R. Huang and Y.C. Tai, Parylene to silicon adhesion enhancement, *Proc. of Transducers 2009*, Denver, CO, USA, 2009, pp. 1027–1030
- [16] J.H.C. Chang, B. Lu and Y.C. Tai, Adhesion-enhancement surface treatments for parylene deposition, *Proc. of Transducers 2011*, Beijing, China, 2011, pp. 390–393
- [17] B. Lu, S. Zheng, S. Xie and Y.C. Tai, Live capture of circulating tumor cells from human blood by a splittable 3D parylene membrane filtration device, *Proc. of μ TAS 2009*, Jeju, Korea, 2009, pp. 588–590
- [18] J.H.C. Chang, D. Kang and Y.C. Tai, Dry mechanical liftoff technology for metallization on parylene-C using SU-8, *Proc. of NEMS 2012*, Kyoto, Japan, 2012.
- [19] B. Lu, J.C.H. Lin, Z. Liu, Y.K. Lee and Y.C. Tai, Highly flexible, transparent and patternable parylene-C superhydrophobic films with high and low adhesion, *Proc. of MEMS 2011*, Cancun, Mexico, 2011, pp. 1143–1146
- [20] M.C. Liu and Y.C. Tai, A 3-D microfluidic combinatorial cell array, *Biomedical Microdevices*, vol. 13, pp. 191–201, 2011
- [21] P.J. Chen, C.Y. Shih and Y.C. Tai, Design, fabrication and characterization of monolithic embedded parylene microchannels in silicon substrate, *Lab on a Chip*, vol. 6, pp. 803–810, 2006
- [22] R. Kawano, T. Osaki and S. Takeuchi, A parylene nanopore for stable planar lipid bilayer membranes, *Proc. of MEMS 2010*, Hong Kong, China, 2010, pp. 923–926

CHAPTER 2

CHARACTERIZATIONS OF PARYLENE MEMBRANES

2.1 Overview

In order to design a parylene microdevice with the desired performance, we must first have a deep understanding of the material properties of parylene itself. Although various properties of parylene have been studied and compared with other common polymers or plastics [1], there are still many unknowns. For example, will the stress-strain curve be different between a 10- μm -thick parylene film and a 0.1- μm -thick parylene film? Will the permeability of parylene change when its thickness is reduced into the submicron range, thus losing its barrier property? Will any properties of parylene be altered by continuous UV illumination or thermal process? How can the surface properties of parylene be modified to enhance or reduce cell adherence? These

questions are closely related to the devices mentioned in Chapters 3 and 4. In this chapter, a series of experiments, measurements, and analyses will be described to explore such interesting topics.

2.2 Mechanical Characterization

2.2.1 A comparison of normal and ultrathin membranes

Mechanical characterization of parylene membranes can be carried out with various technologies, including pressure-loading membrane-deflection tests [2], pulling tests [3], and tensile tests by dynamic mechanical analysis (DMA) machine [4,5]. In most BioMEMS applications, parylene films thicker than 1 μm are used as protective coating or structural layers. It was found that the stress-strain curves are very similar for different parylene films with thicknesses ranging from 10 μm to 20 μm [5]. However, when the thickness of parylene film is reduced to the submicron range, its Young's modulus decreases.

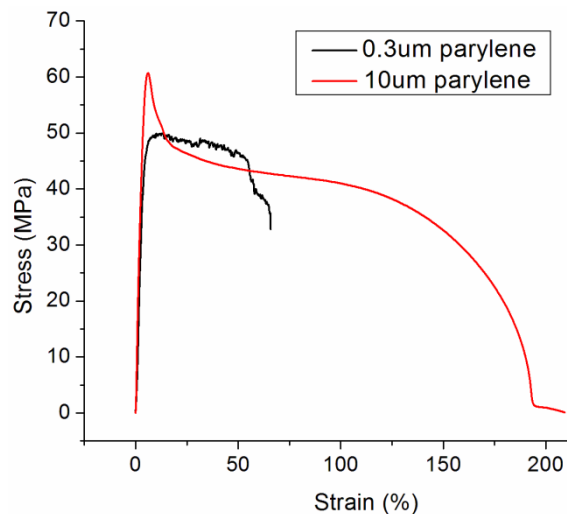


Figure 2-1: Stress-strain curves of parylene films with different thicknesses, measured by DMA at room temperature

Fig. 2-1 shows the stress-strain curves of the 10 μm parylene and 0.3 μm parylene films measured by DMA at room temperature. Compared to thick parylene film with ~ 2.67 GPa Young's modulus and ~ 60 MPa yielding strength, the submicron parylene film has ~ 1.3 GPa Young's modulus and ~ 50 MPa yielding strength. More remarkably, the submicron parylene breaks when the strain is about 75%, while the thick film can withstand an elongation up to 200%. Although the underlying mechanism of these differences is still not clear at this point, special attention must be paid to devices employing submicron parylene as structural layers.

2.2.2 Strategy to enhance the strength of ultrathin membrane

In the applications where a submicron parylene membrane is used as a structural layer, such as the diffusion region in the parylene artificial Bruch's membrane discussed in Chapter 4, a thick parylene mesh support can be used to improve the mechanical strength of the entire membrane. For such composited membranes, a thick parylene mesh frame is first created and then the submicron parylene is deposited onto the frame. As an example, mechanical properties were compared between a uniform 0.3 μm membrane and a composited membrane with 0.3 μm submicron regions and a 6- μm -thick mesh frame. Both membranes had the same overall diameter of 1.8 mm. Membranes were loaded onto the pressure deflection testing setup (Fig. 2-2). The observed yielding pressure and breaking pressure are shown in Table 2-1. The composited membrane exhibits much improved mechanical strength, which is clearly preferable in device

handling and operation. The ratio of the thin part can be adjusted in different applications according to the mechanical requirements.

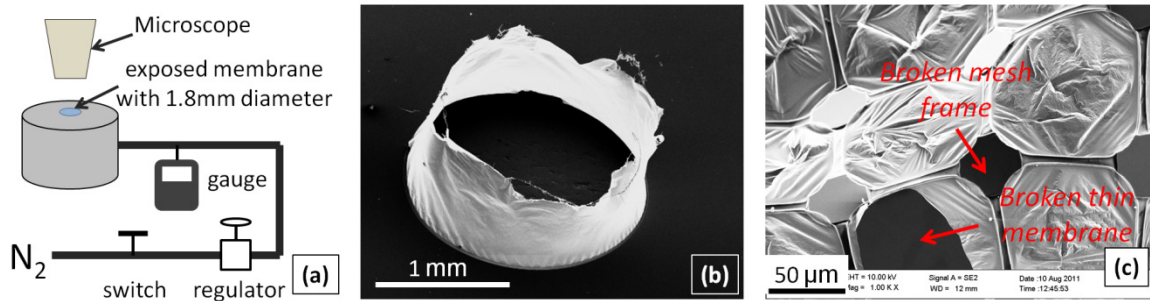


Figure 2-2: (a) The membrane deflection test setup; (b) Uniform submicron parylene is broken at a low pressure load; (c) The composited membrane is broken at a much higher pressure load.

Table 2-1: Comparison of the mechanical strength between the uniform submicron parylene membrane and the composited membrane

<i>Membrane types (overall diameter is 1.8 mm)</i>	<i>Ratio of thin part</i>	<i>Yielding pressure</i>	<i>Breaking pressure</i>
Uniform 0.3 μm membrane	100%	1.50 psi	3.32 psi
Composited membrane	53%	4.88 psi	19.94 psi

2.3 Semipermeability of Submicron Parylene Membranes

Parylene is usually believed to be a good barrier material because of its low permeability to water vapor and biological or chemical molecules. For example, the integrated circuit (IC) industry has been using parylene as a moisture-protective layer for IC chip packaging [1]. In BioMEMS applications, parylene protective coating is especially important for implantable biomedical devices in order to isolate corrosive body

fluids [6–8]. However, when the thickness of parylene is reduced to the submicron range, it becomes semipermeable to macromolecules.

2.3.1 Measurements of the diffusion coefficients

The permeability of submicron parylene-C was evaluated by measuring the diffusion coefficients of fluorescein isothiocyanate (FITC)-dextran molecules (Sigma-Aldrich Co.). The FITC-dextran diffusion model was previously demonstrated to be a good model in studying the permeability of Bruch's membrane and other substitute membranes [9]. The diffusivity measurements were performed in blind-well chambers (Neuro Probe, Inc.) with a MSPM clamped in between (Fig. 2-3(a)). FITC-dextran molecules with different MWs (4 K–250 KDa) were initiated in the lower chamber and diffused across the membrane to the upper chamber, which was initially filled with phosphate buffered saline (PBS). All experiments were performed at 37°C. Concentration of dextran diffused into the upper chamber was measured by monitoring the fluorescence intensity versus time. For each measurement, a small volume (4 μ L) of solution was drawn out from the upper chamber and injected into a chambered microscope slide (KOVA Glasstic® Slide 10 with Grids, Hycor Biomedical, Inc.). The fluorescence intensity was measured with a Nikon E800 epifluorescence microscope (Nikon, Inc.), and analyzed by a custom-coded MATLAB program (V6.1.0.450, The Mathworks, Inc.).

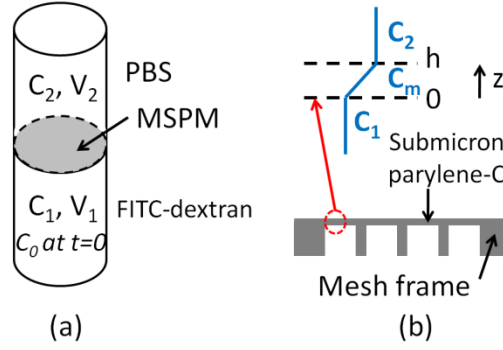


Figure 2-3: Schematic of the diffusivity measurement with blind-well chambers

Methodology for deriving the diffusion coefficient for a single membrane has been reported before [9]. Here, slight modifications were made. The diffusion coefficient can be calculated from the following equation,

$$C_2 = \frac{C_0 V_1}{V_1 + V_2} (1 - \exp(-\frac{Dt}{\tau})), \quad (2-1)$$

where

$$\tau = \frac{(V_1 + A_{eff}h/2)(V_2 + A_{eff}h/2)}{A_{eff}(V_1 + V_2)},$$

with all parameters illustrated in Fig. 2-3(b). C_0 is the initial concentration of FITC-dextran in the lower chamber, and C_2 is the concentration in the upper chamber at time t . The initial concentration in the upper chamber is 0. The volumes of bottom (V_1) and top (V_2) chambers are both 200 μ L. h is the thickness of the submicron membrane. The total exposed area (i.e., the cross-sectional area of the chamber) is $A_{total} = 18 \text{ mm}^2$. However, in this experiment, the effective diffusion area (i.e., the submicron membrane region) is $A_{eff} = 0.35A_{total}$. Several assumptions have been made here. First, the diffusion coefficient D is not a function of time or concentration. Secondly, since the thickness of the submicron membrane is negligible compared to the chamber height, the

volume of dextran contained in the membrane is neglected. In addition, since the sampling volume (4 μL) is small enough compared to the chamber volume, we assume V_2 to be constant during the experiment.

Fluorescence intensities of samples from the upper wells were recorded at different times. The diffusion coefficients of FITC-dextran molecules (4, 10, 40, 70, 125 and 250 KDa) for the ultrathin parylene-C of different thicknesses ranging from 0.15 to 0.80 μm were calculated according to Eq. 2-1 (Fig. 2-4). As expected, smaller molecules in thinner parylene-C membranes have larger effective diffusion coefficients. The calculated diffusion coefficients of various molecules in the submicron parylene-C are in the range of $10^{-10} \sim 10^{-13} \text{ cm}^2/\text{s}$.

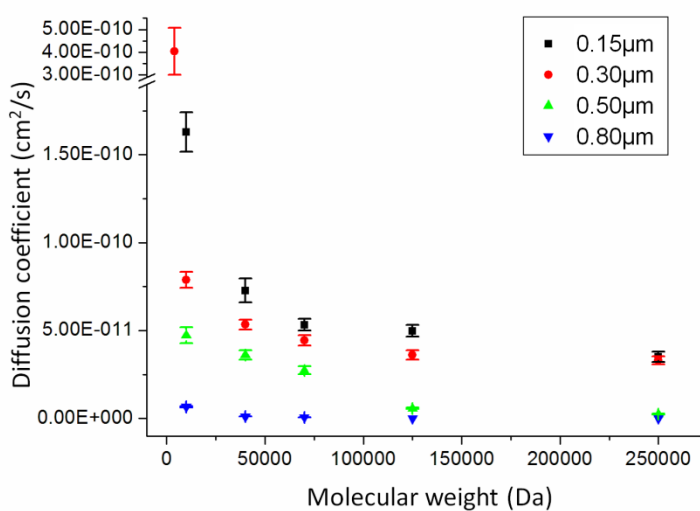


Figure 2-4: Diffusion coefficients of dextran molecules in submicron parylene-C membranes with different thicknesses

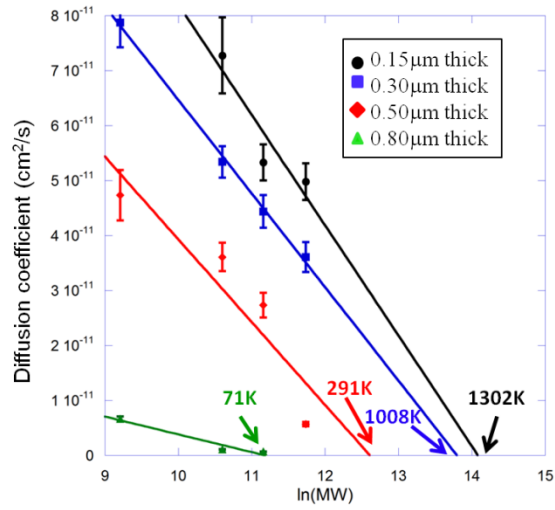


Figure 2-5: Molecular weight exclusion limits of submicron parylene-C membranes

2.3.2 Molecular weight/radius exclusion limits

The theoretical MW exclusion limit is calculated by extrapolating the linear relationship between the diffusion coefficient and $\ln(MW)$ (Fig. 2-5), according to the method reported in [10]. The linear semi-log fitting for the MW exclusion limit uses only the linear regimes of the plot, which correspond to the mid-molecular weights (10–125 KDa). Exclusion limits are determined as the MW at $D = 0$. It is shown that all the membranes thinner than 0.80 μm have MW exclusion limits greater than 70 KDa and therefore can allow the passage of most proteins in serum.

Given the MW exclusion limit, the molecular radius exclusion limit can also be determined [11]. The hydrodynamic radius R_h of the dextran molecule is calculated according to the Einstein viscosity relation:

$$R_h = \left(\frac{3[\eta]M}{10\pi N} \right)^{1/3} \quad (2-2)$$

where M is the molecular weight, N is Avogadro's number, and $[\eta]$ is the intrinsic viscosity, which is related to the MW by the empirical Mark-Houwink equation:

$$[\eta] = KM^a \quad (2-3)$$

where K and a are constants. For dextran, the values of K and a can be obtained from previous literature [11]. Using Eqs. 2-2 and 2-3, we estimated the molecular radius exclusion limits (i.e., the maximum molecule size allowed for passage) (Table 2-2). This molecular radius exclusion limit also indicates the porosity of the submicron parylene-C membranes. As the thickness decreases, parylene-C membranes have increasing nanopore sizes (Table 2-2).

Table 2-2: Molecular radius exclusion limits of submicron parylene-C membranes

<i>Thickness</i> (μm)	<i>Exclusion MW</i> (KDa)	<i>Exclusion radius</i> (nm)
0.15	1,302	25.60
0.30	1,008	22.62
0.50	291	12.39
0.80	71	6.25

2.4 Parylene Autofluorescence

2.4.1 Motivation

For a large number of biomedical applications, on-chip fluorescence detection has been the golden standard. Many of them require precise detection of small fluorescence signals due to the small sample volume and low concentration of fluorophores [12–14]. In these cases, autofluorescence of the chip material itself becomes important, since it may interfere or even overwhelm the signals of interest. However, it is well known that many polymers and plastics are fluorescent when excited by UV or even visible light [15,16].

Unfortunately, this problem also exists in parylene-based devices. The undesired autofluorescence of parylene-C can sometimes be a major obstacle for its use in devices with fluorescence detection, especially for those that require ultraviolet (UV) light illumination. For instance, the strong autofluorescence in our previously reported parylene-C microfilters prevented us from using common chemical dyes, such as DAPI (4', 6-diamidino-2-phenylindole) (excitation maximum (ex): 358 nm; emission maximum (em): 461 nm) or Hoechst 33342 (ex: 350 nm; em: 461 nm), and fluorophore (especially blue) conjugated antibodies for circulating tumor cell (CTC) enumeration after on-chip enrichment from patient blood samples (Fig. 2-6) [12]. Strong blue autofluorescence was also found in the parylene-C probe for neural prosthesis application, when observing Hoechst-stained neural stem cells [13]. Although the autofluorescence influence is less severe when detecting long wavelength fluorescence signals (e.g., green or red) [14,17], it may still disturb the detection if the target fluorescence signal itself is very small, such as with on-chip real-time PCR or on-chip flow cytometer applications [18].

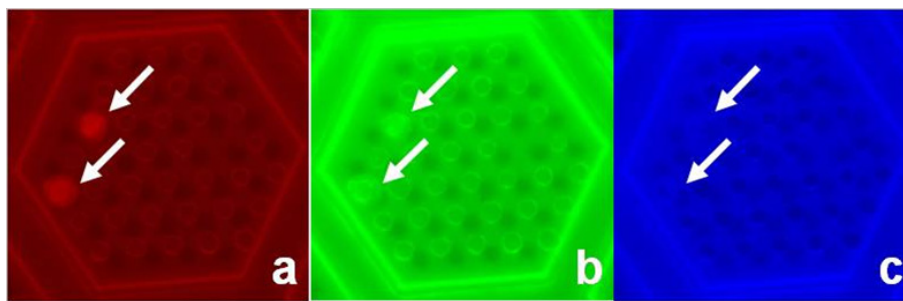


Figure 2-6: Strong autofluorescence in parylene-C-based dual-layer membrane CTC microfilter. Captured prostate cancer cells were doubly immunofluorescence stained with red and green fluorescence dye conjugated anti-CK (a) and anti-PSA (b). The cell nucleus was stained with DAPI (c). Red and green autofluorescence greatly disturbed the cell detection, while blue autofluorescence totally overwhelmed the stained cells.

In this section, an in-depth study was carried out on the fluorescence mechanisms of different kinds of parylene films. Parylene-C was compared with other commercially available polymers and plastics for their autofluorescence. Variation of autofluorescence intensity of parylene-C film during continuous UV illumination was found to be related to both dehydrogenation and photo-oxidation. The influence of microfabrication process on parylene-C autofluorescence was also evaluated and discussed. Enhanced autofluorescence during microscope observation, fluorescence detection or fabrication process makes parylene-C non-ideal for applications where autofluorescence is a concern. Several other commercialized parylene materials, parylene-D, parylene-N, and parylene-HT (Fig. 2-7) were also studied.

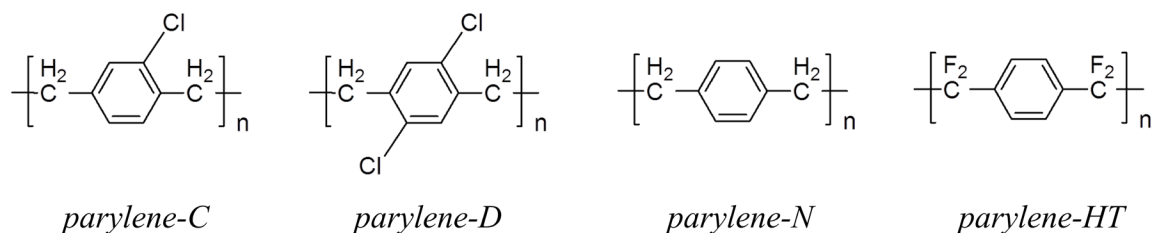


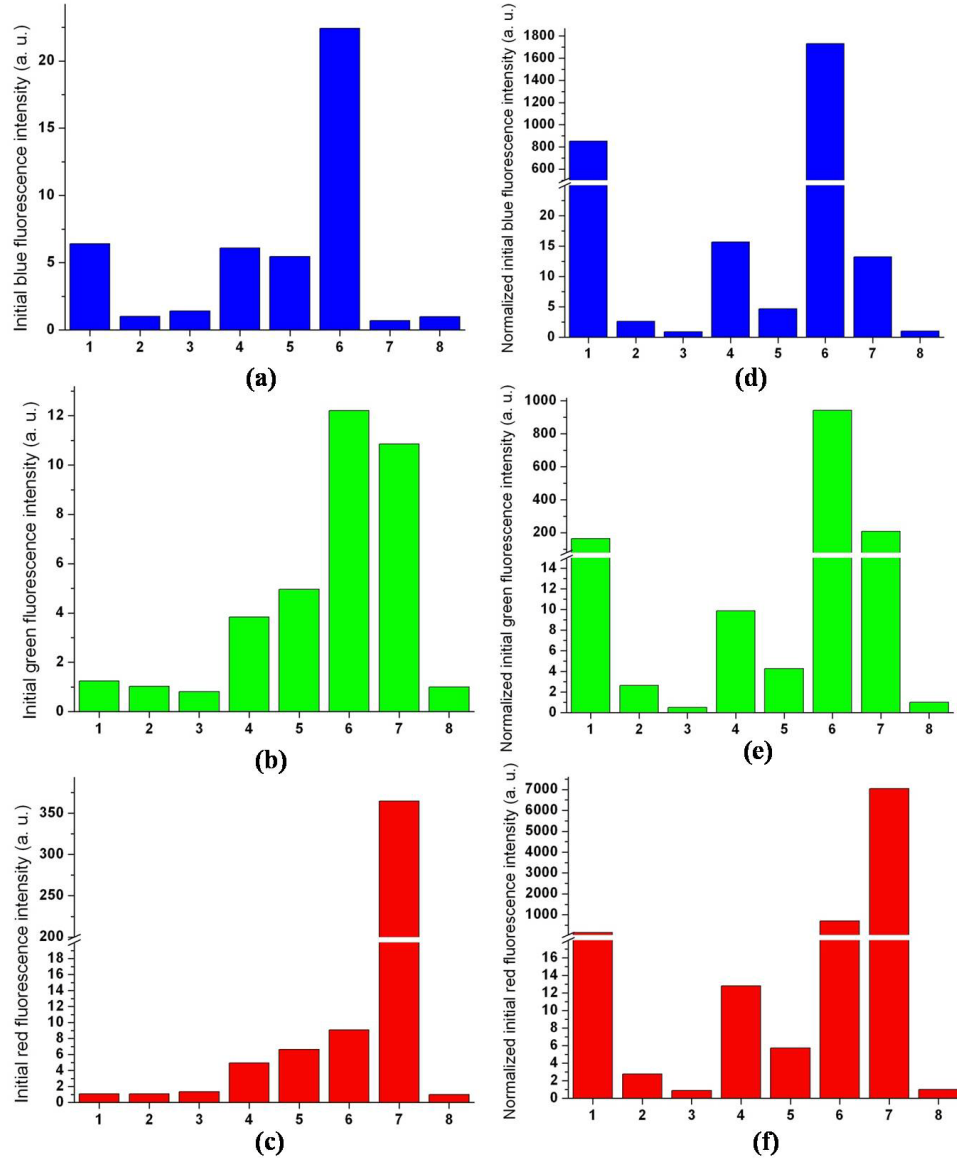
Figure 2-7: Structure of parylene-C, parylene-D, parylene-N, and parylene-HT films

2.4.2 Comparisons of parylene with other polymers/plastics

To compare fluorescence properties of parylene with other commonly used polymers and plastics, following commercial materials were purchased: 1.52 mm poly(methylmethacrylate) sheet (PMMA, McMaster-Carr), 0.38 mm polycarbonate film (PC, McMaster-Carr), 50 μm polyimide film (McMaster-Carr), 13 μm PET polyester film (McMaster-Carr), poly(dimethylsiloxane) (PDMS) (PDMS, Dow Corning Sylgard 184 kit), and 1.14 mm polystyrene tissue culture dish (Becton Dickinson Labware). 0.38

mm PDMS sheets were made by mixing the base to curing agent at a 10:1 ratio, degassing, spin coating, and baking according to manufacturer's instruction. A 0.98 mm Corning[®] glass microscope slide (Corning Inc.) was used as an autofluorescence reference.

Fluorescence was observed under a Nikon E800 epifluorescence microscope (Nikon Inc.). Excitation light came from a USH-102DH 100W mercury arc lamp source (Ushio Inc.), and passed through a dichromatic mirror and one of the following band-pass filters: UV-2E/C, B-2E/C, or G-2E/C, with excitation wavelengths of 340–380 nm, 465–495 nm, and 528–553 nm, and emission wavelengths of 435–485 nm (blue fluorescence), 515–555 nm (green fluorescence), and 590–650 nm (red fluorescence), respectively. Experiments were done with a 20x objective. Continuous UV illumination was carried out by using UV-2E/C filter. Images were taken with a CCD camera (RT-KE color 3-shot, Diagnostic Instruments). The “exposure time” refers to the collecting time the CCD camera used to take an image. To avoid saturation of the image, sometimes the exposure time had to be adjusted for different samples. The images were then transferred into 8-bit grayscale images and the fluorescence intensity distributions were calculated using a custom-coded MATLAB (V6.1.0.450, The Mathworks, Inc.) program. In order to evaluate the variations from the mercury arc lamp, fluorescence from the Corning[®] glass microscope slide was used as an internal reference and measured before each experiment and during long-time illumination. Both UV illumination and fluorescence measurement were performed under atmosphere at room temperature.



(1): 5 μm parylene-C; (2): 380 μm PDMS; (3): 1.52 mm PMMA; (4): 380 μm polycarbonate; (5): 1.14 mm polystyrene; (6): 12.7 μm polyester; (7): 50.8 μm polyimide; (8): 980 μm Corning[®] glass slide (control)

Figure 2-8: Comparisons of relative initial autofluorescence intensities of parylene-C with other polymers and plastics. Autofluorescence of Corning[®] glass microscope slide was set as 1 (a.u.), and all the other fluorescence intensities were relative to this reference. (a)—(c) show blue, green and red autofluorescence of materials with different thicknesses. (d)—(f) show blue, green and red autofluorescence of materials normalized to 5 μm thickness. All measurements were carried out with a 20x objective. Exposure time: blue (1 s), green (10 s), red (10 s)

Fig. 2-8(a)–(c) show the comparison of initial autofluorescence intensities of 5- μm -thick as-deposited parylene-C film with other commonly used, commercially available polymer and plastic materials, including PDMS, PMMA, polycarbonate, polystyrene, polyester, and polyimide, as measured by the epifluorescence microscope. Since it is reasonable to assume the intensity was approximately proportional to material thickness [15], the intensities of materials were normalized to 5 μm thickness and also compared in Fig. 2-8(d)–(f). Among the selected materials, parylene-C has strong initial autofluorescence per unit thickness, although it is not the worst one. For parylene-C, blue fluorescence intensity was much higher than green or red fluorescence. For applications requiring high sensitivity, extremely small fluorescence signals may be easily buried within this undesired autofluorescence noise.

2.4.3 Autofluorescence behaviors during UV illumination

For many applications involving optical detection or observation, the polymer and plastic microchips will be illuminated for a period of time, thus the trend and variation of autofluorescence under continuous illumination, rather than the initial autofluorescence, are more important. Previous reports showed that a lot of polymers and plastics—including PDMS, PMMA, polycarbonate, polyester, and polystyrene—had decreasing autofluorescence under continuous illumination, with complex kinetics which are still not fully understood [15,16]. For all four kinds of parylene films studied here, continuous blue or green light illumination under fluorescence microscope did not cause observable green or red autofluorescence intensity variation. Surprisingly, for blue fluorescence under UV excitation, the initial intensity of parylene-C film dramatically increased during

a 2 min, short-time UV illumination from the microscope light source (Fig. 2-9(a)). After UV illumination, green and red fluorescence intensities of the exposed area were also enhanced (Fig. 2-9(b)-(c)). The same phenomenon was also found in parylene-C film deposited from diX-C dimer (data not shown). Fig. 2-10 shows the quantitative measurements of fluorescence variations during short-time UV illumination. Parylene-D film exhibited the same behaviors of enhanced autofluorescence as did parylene-C. Autofluorescence intensities of parylene-N film followed a similar trend but slightly increased. However, parylene-HT film showed a reverse trend, with clearly decreasing tendency for blue, green, and red fluorescence (Fig. 2-9(d) and Fig. 2-10).

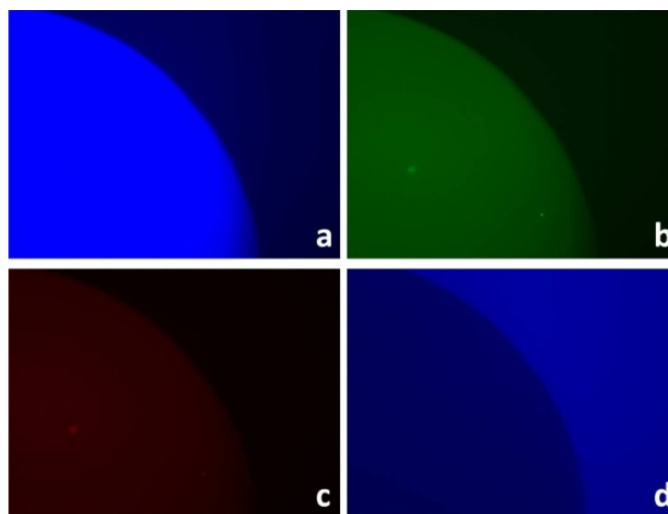


Figure 2-9: (a)—(c): Enhanced blue (a), green (b), and red (c) autofluorescence of parylene-C film after 2 minutes short-time UV illumination. The brighter area was the exposed area under the microscope objective. The darker area was the unexposed area. (d): Reduced blue autofluorescence of parylene-HT film after 2 minutes short-time UV illumination. The darker area was the exposed area. Images for reduced green or red autofluorescence were not shown here because the brightness changes were too small for visual discretion. Experiments were carried out with a 20x objective. Exposure time: blue (500 ms), green (10 s), red (10 s)

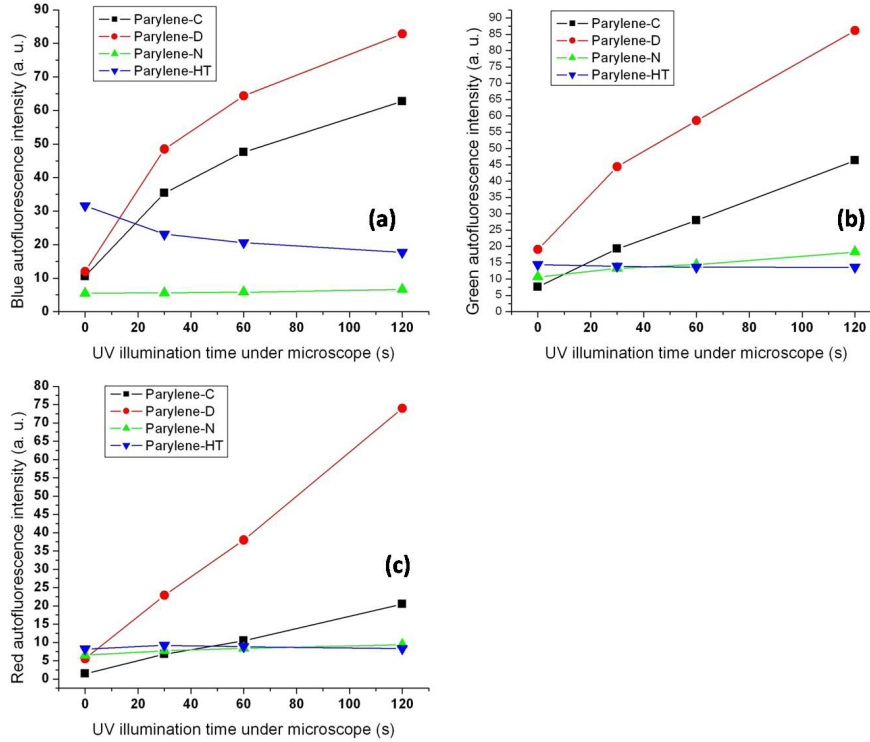


Figure 2-10: Quantitative fluorescence intensity variations of parylene films during continuous short-time UV illumination. (a) Blue fluorescence; (b) green fluorescence; (c) red fluorescence. For all kinds of parylene, film thickness was 5 μm . Experiments were carried out with a 20x objective. Exposure time: blue (500 ms), green (10 s), red (10 s)

To study the fluorescence mechanism of parylene films, we extended the UV illumination experiments to a long period of up to 1000 min and recorded the blue fluorescence intensity variations. Both parylene-C and parylene-D showed a two-stage fluorescence behavior. During initial short-time UV illumination, blue fluorescence increased dramatically (stage 1, Fig. 2-11(a)-(b) insets). However, after reaching its maximum value, the fluorescence intensity started to decay gradually in the following long-time UV illumination (stage 2). Although the magnitudes of initial and maximum fluorescence intensities were similar, parylene-D had faster intensity variations. For parylene-N, during the 1000 min illumination, only the increasing stage was observed

(Fig. 2-11(c)). The long-time illumination of parylene-C, parylene-D, and parylene-N were accompanied by a yellow discoloration of the film. Parylene-D had the fastest rate and largest extent of discoloration, while parylene-N had the slowest rate and only slight discoloration, even for a longer illumination time. Interestingly, although parylene-HT had the largest initial fluorescence intensity, it decreased exponentially from the beginning, with a small time constant upon illumination (Fig. 2-11(d)), and without any sign of yellow discoloration. Three conclusions can be readily drawn from the analysis: (1) During microscope observation or optical detection where UV light is involved, strong autofluorescence of parylene-C and parylene-D can be quickly induced within the first several minutes. Although the increase of parylene-N autofluorescence is much slower, it lasts for a long time. (2) For parylene-C and parylene-D, once the autofluorescence is induced, it takes a long time to reduce the autofluorescence back to the initial level, accompanied by the degradation of films. (3) In contrast, UV illumination can efficiently bleach the autofluorescence of parylene-HT to a very low level within a short time period.

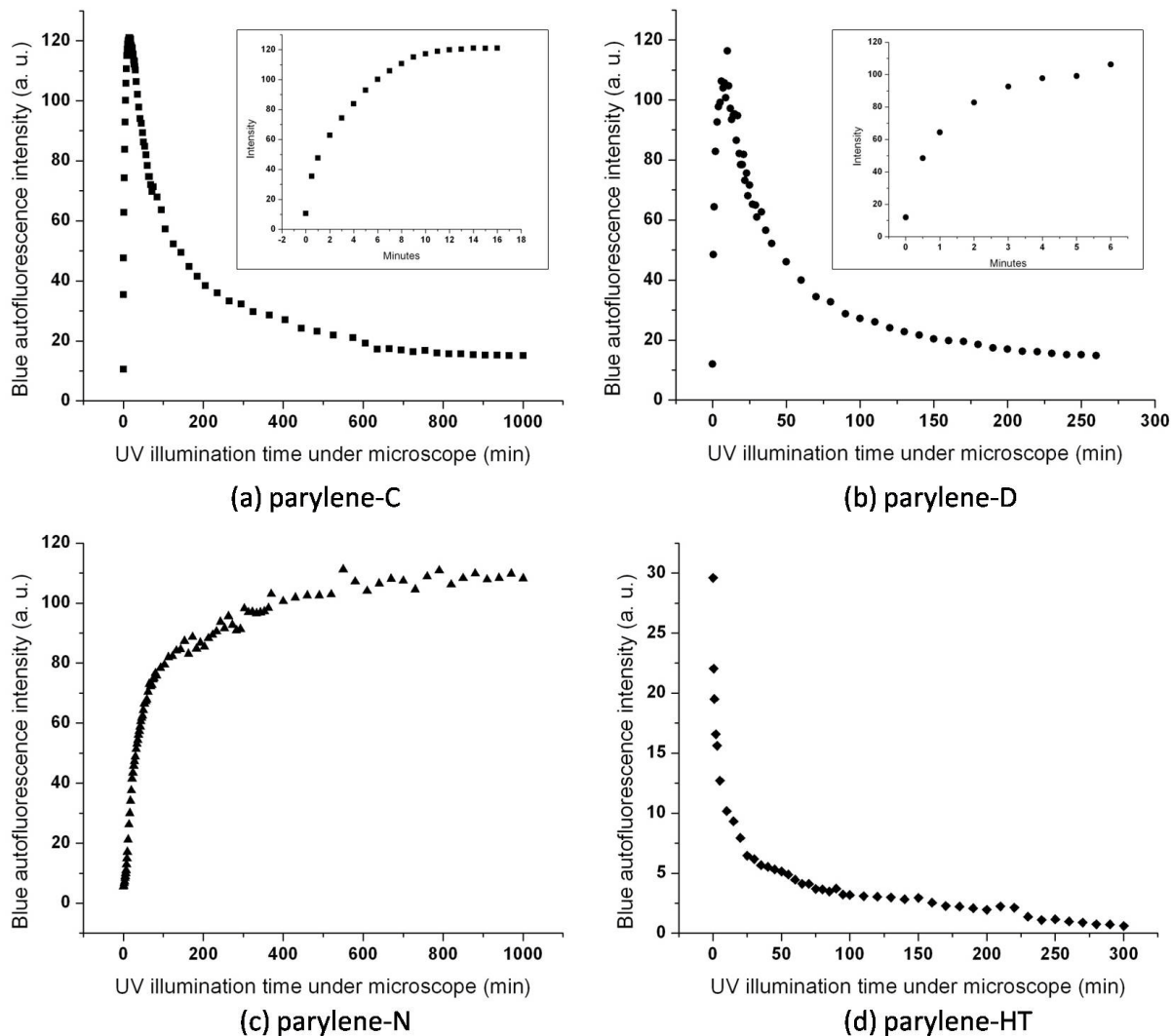


Figure 2-11: Quantitative blue fluorescence intensity variations of parylene films during continuous long-time UV illumination. (a) parylene-C film; (b) parylene-D film; (c) parylene-N film; (d) parylene-HT film. The insets in (a) and (b) show the increasing stage of the curves. For all kinds of parylene, film thickness was 5 μm . Experiments were carried out with a 20x objective. To prevent saturation, exposure time was 100 ms.

2.4.4 The mechanism of autofluorescence in parylene-C/D/N films

To find the mechanism of parylene autofluorescence, material analysis tools such as a fluorimeter and FTIR were also used. The fluorescence spectra of both parylene film and dimer were measured by a Jobin-Yvon JY3D spectrofluorimeter (HORIBA Jobin

Yvon, Inc.). To measure the spectra of the dimer, the dimer was dissolved in methanol first and the solution was placed inside a 3-Q-10 quartz fluorometer cuvette (Starna Cells, Inc.). The IR spectra of parylene films were recorded by a Nicolet 6700 FT-IR Spectrometer (Thermo Fisher Scientific, Inc.). UV illumination of samples for these spectra experiments were prepared by a UV-ozone (UVO) instrument (1.12 mW/cm², 253.7 nm, Jelight Company, Inc.) in the air environment (ozone was not used here), which could uniformly produce photo-chemically modified films with large size.

In order to extract the possible fluorescent contaminants and find the mechanism of fluorescence, parylene films were soaked in methanol, toluene, and methylene dichloride solvents, accompanied by ultrasonic agitation.

Fluorescence spectra of parylene-C film showed that the emission band was red shifted from the UV range to the visible range during short-time UV illumination, resulting in the enhanced fluorescence in the visible range (Fig. 2-12). Corresponding infrared (IR) spectra of parylene-C film are shown in Fig. 2-13. The peaks in the region of 1450 ~ 1610 cm⁻¹ could be attributed to C=C double-bond stretching vibrations. After 5 min illumination, an increase of the absorption peak around 1560 cm⁻¹ occurred, which could be interpreted as the increasing amount of C=C bonds in the chain adjacent to the benzene ring. This change of chemical structure is likely to be a sign of the scission of chain C-H bonds and the occurrence of dehydrogenation. During the long-time UV illumination, however, a reduction of emission band magnitude was observed from fluorescence spectra, with unchanged spectra shape and peak location (Fig. 2-12). In IR spectra, C=C absorption decreased, while C-O (1250 cm⁻¹) band and C=O (1700 cm⁻¹)

peak appeared and increased (Fig. 2-13). This evidence indicates that oxidation happened during long-time illumination.

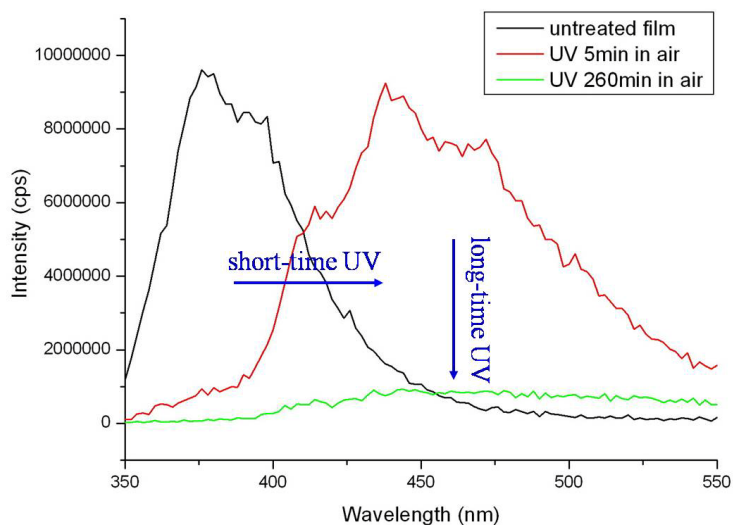


Figure 2-12: Fluorescence spectra of parylene-C film, under 280 nm excitation, measured by fluorimeter

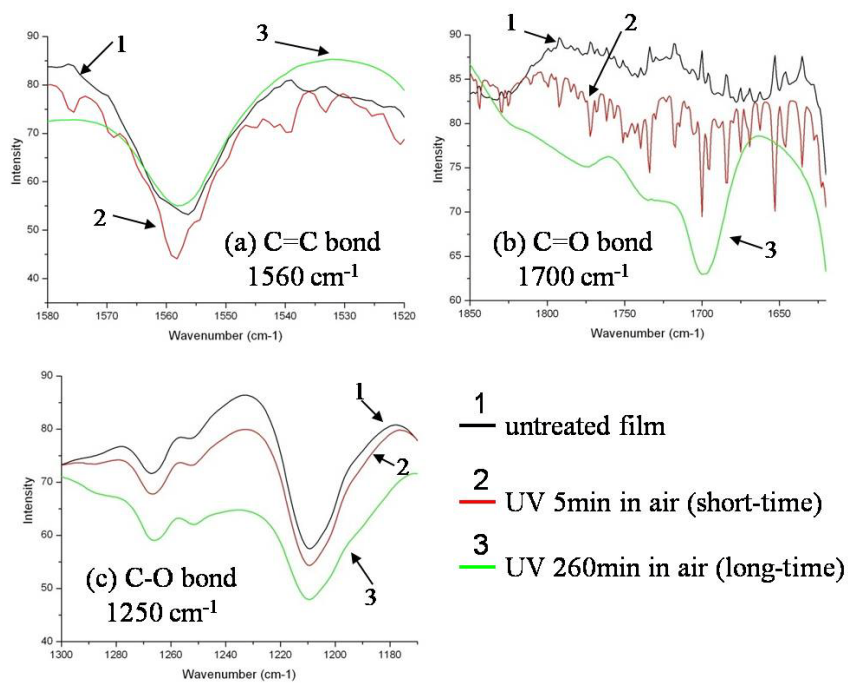


Figure 2-13: Infrared spectra of parylene-C film, measured by infrared spectrometer

A few conclusions can be drawn from above experiment results: (1) Fluorescence intensity variations of parylene-C film are related to the variation of unsaturated C=C bonds in the main chain. Analogous to parylene-N, the initial low fluorescence of parylene-C might also come from the small amount of C=C defects in the main chain generated during the deposition process [19]. (2) During short-time UV illumination, dehydrogenation dominated and an increasing amount of C=C bonds formed. This led to an increased conjugation length, which was responsible for the red shift of the fluorescence spectra from the UV range to the visible range [20]. On the other hand, photo-oxidation was limited by oxygen diffusion into the film [21,22]. During the initial illumination, although photo-oxidation also occurred, it was insignificant due to the insufficient contact between oxygen and carbon molecules. (3) During long-time UV illumination, photo-oxidation gradually became dominant. C=C bonds in the main chain were oxidized into C-O or C=O bonds, resulting in the reduction of fluorescence magnitude.

Here we present a hypothesis to explain the difference in kinetics of fluorescence change in parylene-C, parylene-D, and parylene-N. Parylene-D and parylene-N have essentially the same structure as parylene-C, modified only by the number of substitution of chlorine atoms for aromatic hydrogens. Following very similar fluorescence variation trends, with both increasing and decreasing stages, parylene-D was likely to have the same fluorescence mechanism as parylene-C. However, up to 1000 min illumination, no decreasing stage was observed for parylene-N, which was probably due to the absence of chlorine substitution. Bera et al. [23] found that during the early stage of UV-induced photo-oxidation, chloro-related photolytical photoproducts forming at the surface of

parylene-C after C-Cl bond scission could prevent the absorption of UV light during subsequent illumination. The formation of these UV-absorbing photoproducts might also be a plausible explanation for the different fluorescence behaviors observed.

During the early stage of UV illumination, dehydrogenation of the chain carbons occurred, accompanied by fluorescence increase. Oxidation at this point started from the surface and was slow, since its rate was limited by oxygen diffusion into the parylene film [22]. Fluorescence reached its peak when, for parylene-C and parylene-D, the chloro-related photolytical photoproducts near the surface prevented UV light from penetrating deeper into the film, thus greatly slowing down dehydrogenation as the surface chain hydrogens were consumed. This set the stage for fluorescence to decrease as photo-oxidation, during which the C=C double bonds became oxidized and no longer contributed to fluorescence, began to dominate.

For the non-halogen parylene-N, UV illumination was not accompanied by the formation of UV-absorbing products, thus dehydrogenation was able to continue for a much longer time by accessing hydrogens deeper in the bulk. Photo-oxidation was able to compete, but not yet dominate, during this longer time span, limiting the rate and extent of fluorescence increase. This resulted in a gradually increasing fluorescence curve throughout the 1000 min illumination. The decreasing stage of parylene-N may be expected when illumination time is sufficiently long, the chain hydrogens in the bulk become scarce, further dehydrogenation slows down, and oxidation finally becomes dominant.

2.4.5 Parylene-HT: A better choice for autofluorescence concerns

Parylene-HT replaces the chain hydrogen of parylene-N with fluorine. Since the strength of the C-F bond is much higher than that of the C-H bond, fluorine extraction is unlikely to occur during UV illumination; this was also verified by fluorescence and IR spectra. No shift of emission band was observed from fluorescence spectra during UV illumination. Reduction of spectra magnitude was in accordance with the decreasing fluorescence intensity. IR spectra of parylene-HT film showed no clear change in the regions of chain C=C, C=O, or C-O bonds, indicating that fluorine extraction and photo-oxidation were unlikely to happen under UV illumination (data not shown).

To find the fluorescence mechanism of parylene-HT film, the fluorescence spectra of parylene-HT film and its dimer precursor were compared. To measure the spectra of the dimer, we first scanned the spectra of methanol solvent, then dissolved the dimer in methanol and measured the spectra of the solution. Fig. 2-14 shows that there were two peaks for the spectra of the solution. When excitation wavelength increased, the peak location of the methanol spectra also shifted, while the other peak remained at the same location and only the intensity decreased. This meant that the former peak was the Raman spectrum of methanol and the latter was the fluorescence spectrum of parylene-HT dimer. A comparison of fluorescence spectra of parylene-HT dimer and film showed a similar peak shape and location, indicating that the fluorescence of parylene-HT film might come from the residual dimer inside the film.

We also verified this conclusion by soaking tests with methanol, toluene, and methylene dichloride. Soaking tests with these three solvents had no effect on the fluorescence of parylene-C, parylene-D, and parylene-N films. Although methanol or

toluene still failed to vary the fluorescence of parylene-HT film, methylene dichloride could effectively reduce the fluorescence intensity of parylene-HT film. After 1.5 hours soaking, the fluorescence intensity was reduced to 35% of its initial level. Therefore, methylene dichloride could dissolve and soak out the residual dimer inside the film, resulting in the reduction of fluorescence of the film. One possible explanation of the time-dependent fluorescence intensity reduction of parylene-HT film under UV illumination could be photobleaching of fluorophores in the dimer. It is also possible that the cleavage of the dimer to its monomeric form happened under UV illumination, resulting in the lost of its fluorescence property.

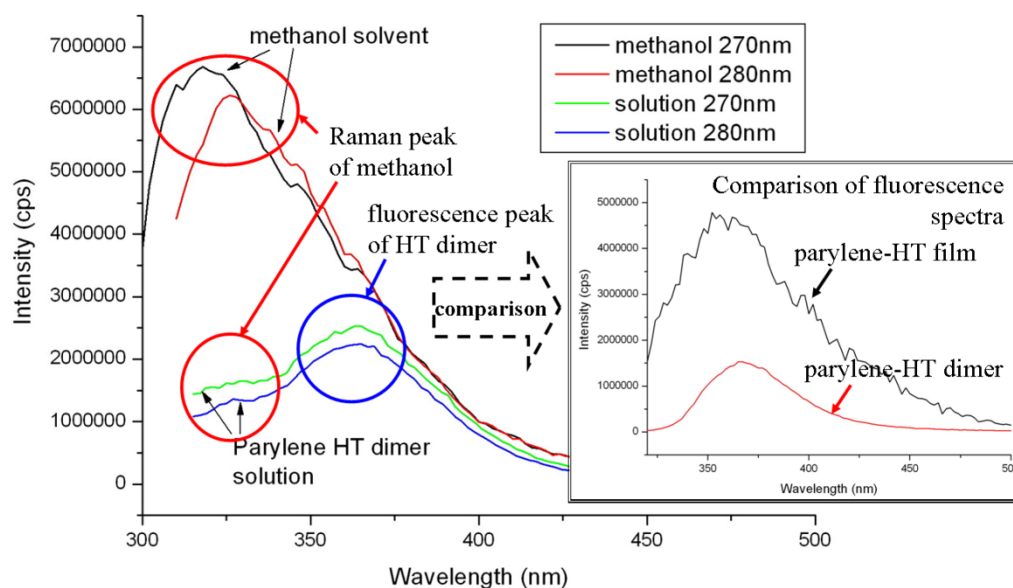


Figure 2-14: Fluorescence spectra of parylene-HT dimer and film. Dimer was dissolved in methanol. Inset compares the spectra of parylene-HT dimer and film, which have similar shape and peak location.

Overall, besides the initial autofluorescence, the undesired autofluorescence of parylene-C-based devices can also be easily induced during epifluorescence microscope

observation, UV illuminated fluorescence detection, or microfabrication process. Given this disadvantage, parylene-C may not be the best chip material if sensitive fluorescence detection is required. For these applications, parylene-HT should be considered as an alternative. Intentional UV illumination can be employed as a pre-treatment to reduce the initial autofluorescence of parylene-HT devices to a desired level. For instance, it took approximately 35 min, 140 min, and 230 min to reduce the autofluorescence magnitude to 20%, 10%, and 5% of its original level, respectively (Fig. 2-11(d)).

An example of the better autofluorescence performance of parylene-HT will be shown in Section 3.5.2, where a parylene-HT filter exhibits much better detection sensitivity than a parylene-C filter.

2.4.6 Autofluorescence induced in microfabrication process

It was noticed that for several polymers and plastics, the microchips exhibited higher autofluorescence than the raw materials from which they had been made [15]. Here we compare the autofluorescence of unpatterned parylene-C film with parylene-C based microdevices (Fig. 2-15). Several μ TAS devices, including a real-time PCR chip [18], a cell culture chamber [24], a 2D membrane CTC filter [25], a 3D membrane CTC filter [12] and a 3D splittable membrane CTC filter [26], were fabricated following different microfabrication processes as described in detail in previous publications. In all of those devices, there was parylene-C deposited on low-autofluorescence silicon substrate or parylene-C freestanding structures. The influences of other possible fluorescent materials, such as SU-8 layer, were excluded by observation of the areas without these materials. Fig. 2-15 shows that in all cases, parylene-C structures in

microdevices exhibited considerably higher autofluorescence than unpatterned parylene-C film, after being normalized to the same thickness.

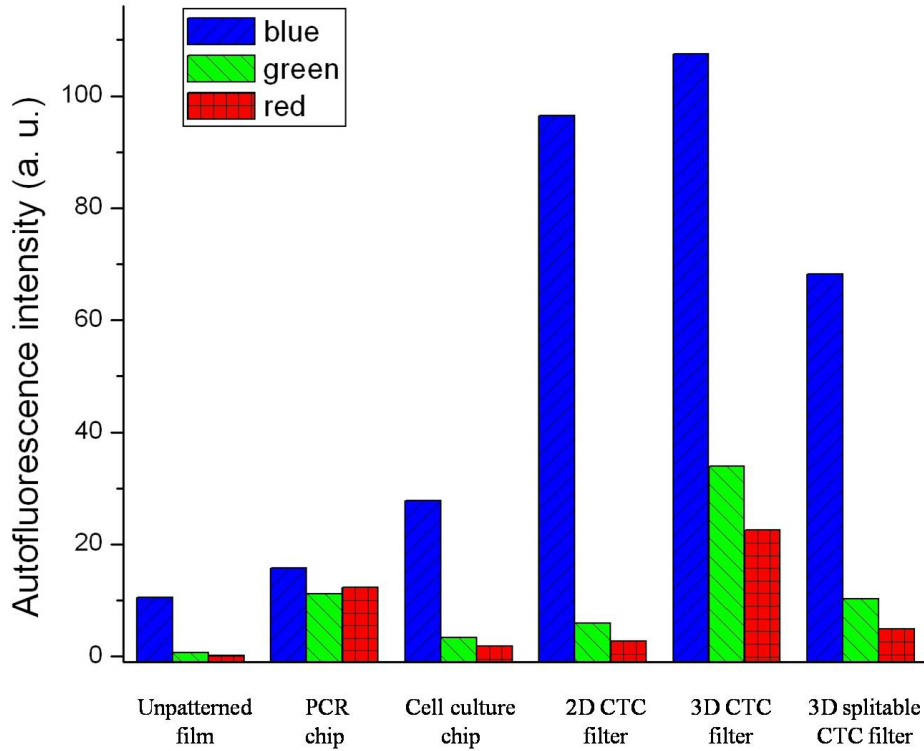


Figure 2-15: Comparisons of autofluorescence of unpatterned parylene-C film and parylene-C-based devices, including a PCR chip, a cell culture chip, a 2D CTC filter, a 3D CTC filter, and a 3D splitable CTC filter. The thickness of all samples was normalized to 5 μm . Experiments were carried out with a 20x objective. Exposure time: blue (100 ms), green (1 s), red (1 s).

The additional autofluorescence was likely induced during the microfabrication processes, especially for steps where short-wavelength light sources were used or generated, such as photolithography, plasma etching, and metal deposition in an e-beam evaporator. For example, a metal layer is usually used as the mask for parylene etching. Different deposition methods of aluminum result in very different autofluorescence in the

underlying parylene layer. If an e-beam evaporator is used, x-rays or many other short-wavelength lights with strong intensity may be released when the e-beam hits and interacts with the metal placed in the crucible [27]. Hence strong autofluorescence is observed in the parylene layer, especially when the metal deposition time is long. An alternative to solve this problem is to switch to a thermal evaporator for metal deposition.

Moreover, it was believed that heating parylene film above certain temperatures could cause crystalline phase transitions, resulting in the increase of long-wavelength fluorescence [19]. Hence several thermal processes, including vacuum annealing and molten parylene in a N₂ environment, were also suspected as sources of strong induced autofluorescence.

2.5 Hydrophilic and Hydrophobic Parylene Membranes

2.5.1 The importance of surface hydrophilicity/hydrophobicity

The surface properties of parylene play a crucial role in determining the cell or protein compatibility on parylene devices. Previous literature reports methods to alter the parylene surface hydrophilicity or hydrophobicity to enhance or reduce cell adherence [28,29]. The as-deposited parylene-C surface is usually hydrophobic, with a contact angle (CA) around 80°. Oxygen plasma treatment can be used to change the surface to be hydrophilic. Chemical or biological coatings on parylene surface are also useful in modifying the cell or protein adherence. For examples, collagen or fibronectin (FN) coating can significantly enhance the cell adherence, while hyaluronic acid (HA) shows the reverse effect [28,29]. It was found that the mechanism of such variations of cell adherence was also closely related to the changes in surface hydrophobicity. Most types

of cells prefer such hydrophilic surfaces [28]. In this section, various plasma surface treatment methods will be described and their influences on the hydrophobicity of a parylene surface will be discussed.

2.5.2 Plasma treatments and their effects on parylene surfaces

The adherence of cells on the substrates depends on both the cell-surface affinity and the surface roughness. A rough surface means the contact area between the cell membrane and the substrate is large. Therefore, this study of the plasma treatments on parylene membrane also evaluates both the surface hydrophobicity and roughness. As-deposited parylene-C has a CA of around 80° . It was reported that CF_4 plasma can lower the surface energy and further increase the CA of parylene-C [30]. Here, the effects of surface treatments on unpatterned parylene-C films with different fluorine plasmas, including SF_6 , CF_4 , and NF_3 plasma (300 W, 300 mTorr), were examined by measuring the CAs, as shown in Fig. 2-16(a). SF_6 plasma was found to be the best choice, with the ability to increase the CA of unpatterned parylene from $\sim 80^\circ$ to $> 120^\circ$ within 5 minutes (Fig. 2-16(a)).

The increase of surface hydrophobicity is usually achieved by creating micro/nano structures on the surface to increase roughness. In our experiments, micropillars with diameter (d), pitch (p), and height (h) were first created on silicon substrate using DRIE. A 10- μm -thick parylene film was then deposited on this silicon mold, allowing the transfer of such micropatterns to the parylene surface. For parylene films with micropillars, several designs with different dimensions were compared. However, at least in the range we studied, no clear difference was observed on the CA

(Fig. 2-16(b)). After SF₆ plasma treatment, the CA of the structured parylene surface was enhanced to > 150° (Fig. 2-16(b)). By comparing the CAs right after treatment and two months after treatment, we found that the effect of SF₆ plasma treatment on the hydrophobicity of parylene-C was permanent (Fig. 2-16(c)).

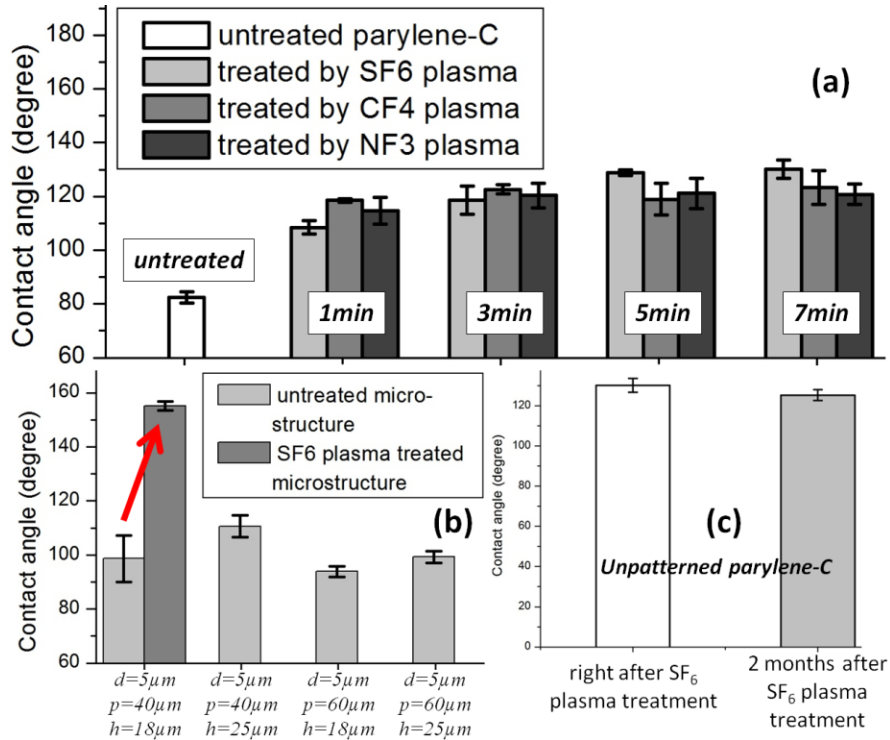


Figure 2-16: The effects of fluorine plasma treatment on (a) unpatterned parylene-C, and (b) structured parylene-C with micropillars. (c) Evaluation of the long-term effect of SF₆ plasma treatment

Fig. 2-17 shows the AFM (Veeco Instruments, Inc.) measurement of parylene's root mean square (rms) surface roughness (σ) after plasma treatments. O₂ plasma (300 W, 300 mTorr) effectively roughened parylene ($\sigma > 100$ nm), especially when photoresist was pre-coated as an etching mask and was over-etched through during O₂ plasma treatment. However, fluorine plasma only caused slight or moderate surface roughness (σ

<50 nm). Fig. 2-17(b) indicates that after O₂ plasma roughening, nanostructures appeared on the parylene surface.

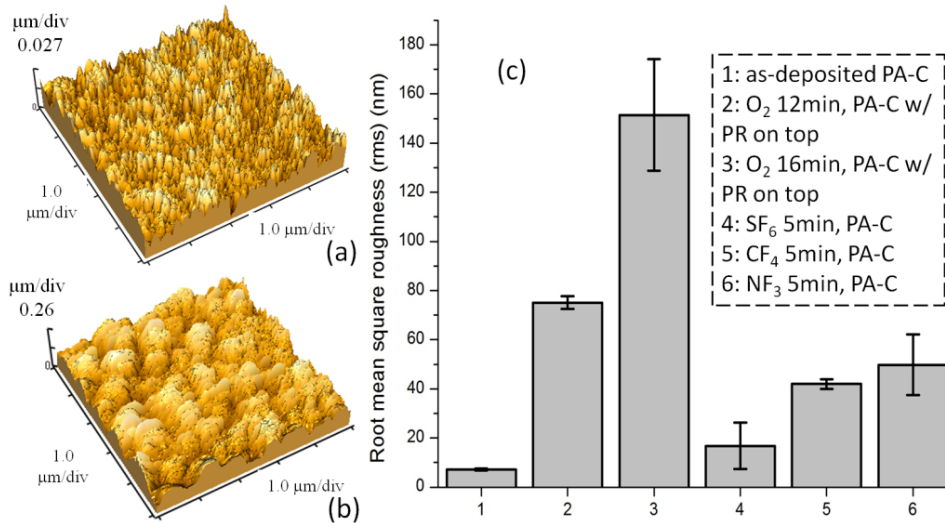


Figure 2-17: AFM evaluation of the rms surface roughness. (a) Untreated parylene-C (PA-C). (b) Parylene-C treated with O₂ plasma for 12 min, with photoresist (PR) on top. (c) Rms roughness of parylene-C with different plasma treatment conditions

2.5.3 Superhydrophobic parylene membrane

In general, superhydrophobic surfaces with a static contact angle (CA) larger than 150° can be divided into two categories [31]: superhydrophobic surfaces with low adhesion, which mimic the lotus leaf effect, and superhydrophobic surfaces with high adhesion, which mimic the rose petal effect. Both designs have numerous applications. For examples, surfaces with the lotus effect have self-cleaning features and can be adopted in low-friction fluid flow [32]. Surfaces with the petal effect can be used in the transport of liquid microdroplets over a surface without rolling and sliding, and is used inside aircraft ceilings to prevent the falling of condensed water droplets onto passengers

[32]. More importantly, superhydrophobic films also drew special attention in the BioMEMS field. Cell adhesive behavior was correlated to the superhydrophobic, superhydrophilic, and micropatterned superhydrophilic/superhydrophobic surfaces and their surface chemistry [33]. Superhydrophobic surfaces may play an increasingly more important role in the 3D cell pattern constructions and tissue engineering. For example, recently a self-folding cell origami technique was created to construct 3D cell patterns by self-folding effects when cells were seeded and cultured on certain areas patterned with different surface hydrophobicity [34].

In our work, we create a superhydrophobic parylene membrane by adopting the hierarchical micro/nano patterns in combination with oxygen and fluorine plasma treatments. The fabrication of superhydrophobic films started with DRIE etching of micropillar arrays on a silicon substrate (Fig. 2-18). After HMDS coating to reduce the adhesion between silicon and parylene, the substrate was coated with a 7- μm -thick parylene. For both the lotus leaf and rose petal models, SF_6 plasma was used to fluorinate the parylene surface and increase its hydrophobicity as shown in Fig. 2-18(e1) and (c2), respectively. However, to achieve the lotus effect, before the SF_6 plasma fluorination, ~ 21 - μm -thick photoresist was spin-coated on the substrate and an additional O_2 plasma etching step was needed to further roughen the top surface of the parylene micropillars (Fig. 2-18(c1) and (d1)). Finally, parylene films with hierarchical structures were peeled off from the silicon substrate.

Fig. 2-19(a) and (b) show the SEM (Zeiss 1550 VP FESEM) images of the front and back side of the fabricated superhydrophobic films. Since parylene is mechanically robust but flexible, no damage was observed after peeling off the film from the silicon

substrate. Corresponding to the AFM results, SEM images show that the lotus leaf model has highly roughened nanostructures on the top surface of micropillars due to O₂ plasma (Fig. 2-19(c) and (d)). In comparison, in the rose petal model, the micropillar has a much smoother top surface (Fig. 2-19(e) and (f)), with only small nanostructures.

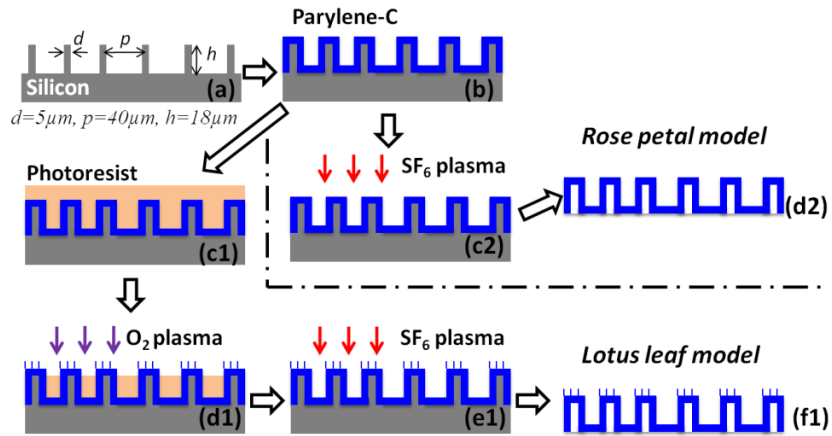


Figure 2-18: Fabrication process of two types of superhydrophobic parylene-C films

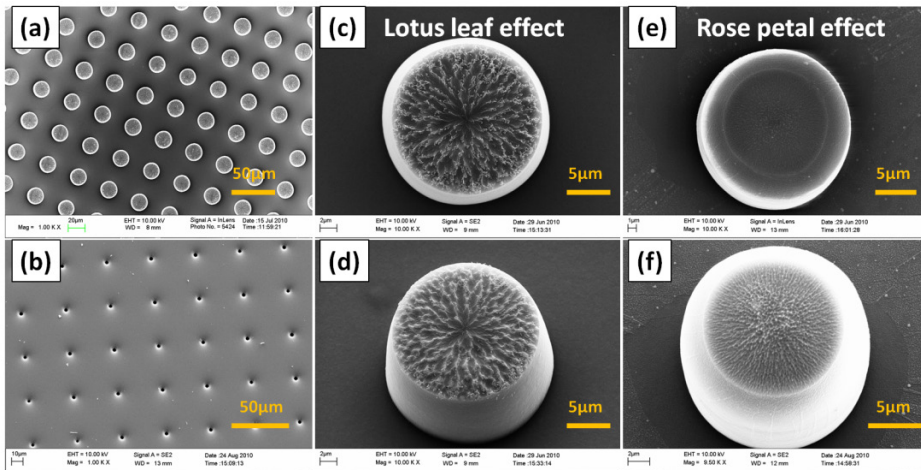


Figure 2-19: SEM images of: (a) and (b) top view of the front and back sides of superhydrophobic film; (c) and (d) top and tilted views of superhydrophobic structure which mimics lotus leaf; (e) and (f) top and tilted views of superhydrophobic structure which mimics rose petal

To evaluate the CA and contact angle hysteresis (CAH) of the superhydrophobic film with low adhesion, a deionized water droplet of 4 μL volume was dispensed by a micropipette on the top surface, and the CA was measured with a Contact Angle Goniometer (Model 100-00, Ramé-Hart Instrument Co.). The CAH is defined as the difference between the advancing and receding angles, which were measured by increasing or decreasing the volume of the water droplet while keeping the bottom contact area unchanged. The water droplet had a CA of $155.5 \pm 3.7^\circ$ on this hierarchical structure, and there were clear trapped air pockets (Fig. 2-20(a)). The low adhesion between the droplet and film was demonstrated by measuring the advancing and receding angles (Fig. 2-20(b)-(c)), and a low CAH of $\sim 6^\circ$ was calculated. All the images were taken with an eyepiece camera mounted onto the Goniometer.

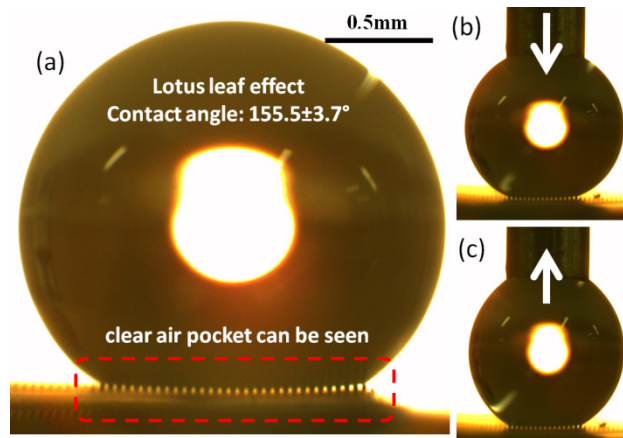


Figure 2-20: Water droplet on a superhydrophobic film with low adhesion (lotus leaf). (a) CA measurement. A clear air pocket was observed. (b) Advancing angle; (c) Receding angle

In the case of a superhydrophobic film with high adhesion, the CA was measured to be $155.1 \pm 1.7^\circ$ (Fig. 2-21(a)). However, unlike in the low-adhesion case, water could

partially impregnate the microstructures, resulting in a poorly defined air pocket. To demonstrate the high adhesion which was probably ascribed to the penetrated water, the superhydrophobic film was tilted for 90° and 180° . The droplet still adhered to the surface when placed vertically or turned upside down (Fig. 2-21(b)-(c)).

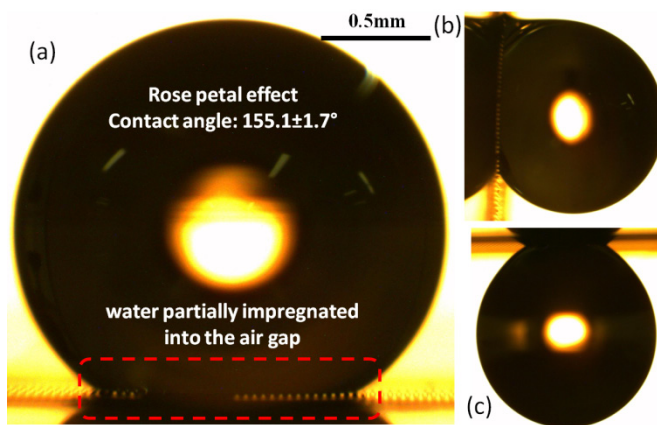


Figure 2-21: Water droplet on a superhydrophobic film with high adhesion (rose petal). (a) CA measurement; Water partially impregnated the gap. (b) and (c) droplet stayed on the film when tilted for 90° and 180°

Our parylene superhydrophobic films possess three advantages. First, flexibility becomes an outstanding feature when curved, folded, or 3D superhydrophobic films are desirable. Fig. 2-22(a)-(b) demonstrates the transparency of the superhydrophobic film, showing a unique advantage over silicon- or thick-plastic- based designs. Although the micro and nanopatterns reduced the transmittance by 10–25%, the film was still transparent, as shown in Fig. 2-22(b). Words underneath the superhydrophobic film could be clearly seen. The optical transmittance and absorptance of as-deposited parylene, parylene with micropillars only, and parylene with hierarchical patterns were measured with an 8453 UV-Visible Spectrophotometer (Agilent Technologies).

Compared with the other designs on rigid or thick substrates, our superhydrophobic thin film could be easily transferred to a curved metal rod (Fig. 2-22(c)). Unlike Teflon or hydrophobic silane-coated surfaces, which are difficult to pattern, we proved the selective patterning of superhydrophilic and superhydrophobic areas on a single film (Fig. 2-22(d)). The hydrophilic areas (the mouth and the outline of the face) were treated with oxygen plasma, having a CA $\sim 5^\circ$. The surface fluid was confined within these superhydrophilic areas. The other areas were superhydrophobic with CA $\sim 155^\circ$. The eyes were two near-spherical droplets. Deionized water was labeled by food dye. Photoresist was used as mask for the selective patterning.

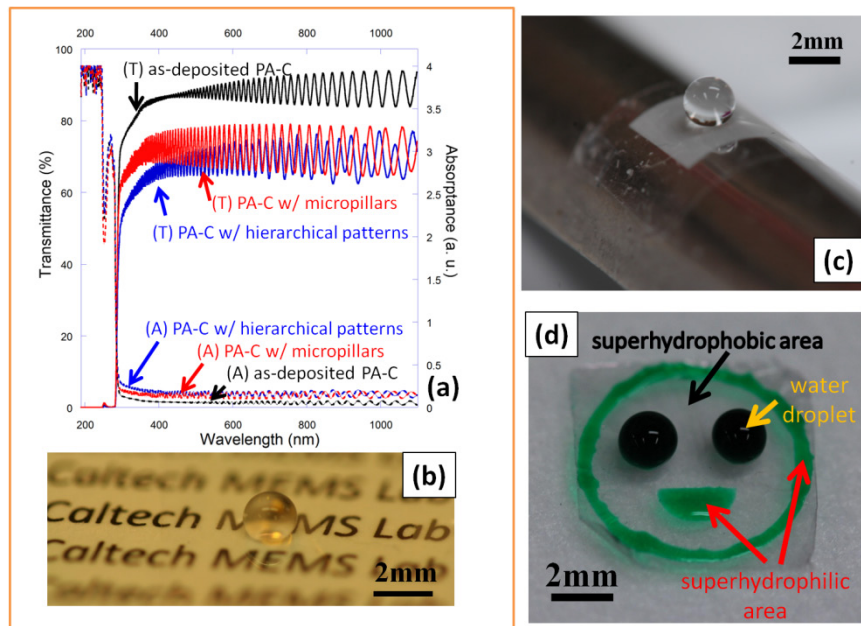


Figure 2-22: Advantages of parylene superhydrophobic film. (a) and (b) transparency; (c) flexibility; (d) selective patterning

To sum up, in this section, we propose simple methods of creating novel superhydrophobic parylene films with high and low adhesions for the biomimetic designs

of both lotus leaf and rose petal. The combination of flexibility, transparency, selective patterning, and simple fabrication makes our superhydrophobic films compare favorably to other designs.

2.6 Summary

This chapter contains the material science studies and characterizations of parylene membrane, which can be considered as the basis of the devices being discussed in the following two chapters. The mechanical properties and semipermeability of submicron parylene make it a potential candidate for therapy of age-related macular degeneration. The autofluorescence study has solved the biggest challenge, the filter background fluorescence problem, in the immunofluorescence detection of circulating tumor cells. The plasma surface treatment techniques are also very useful in culturing cells, as will be shown in Section 3.6. The superhydrophobic films have potential applications in surface non-channel microfluidics, tissue engineering, and cell/protein selective patterning.

2.7 References

- [1] www.scscoatings.com, Specialty Coating Systems (SCS)
- [2] C.Y. Shih, T.A. Harder and Y.C. Tai, Yield strength of thin-film parylene-C, *Microsystem Technologies*, vol. 10, pp. 407–411, 2004
- [3] R. Huang, Flexible neural implants, Ph.D. Thesis, California Institute of Technology, 2011
- [4] J.C.H. Lin, P. Deng, G. Lam, B. Lu, Y.K. Lee and Y.C. Tai, Creep of parylene-C film, *Proc. of Transducers 2011*, Beijing, China, 2011, pp. 2698–2701

- [5] J.C.H. Lin, MEMS for glaucoma, Ph.D. Thesis, California Institute of Technology, 2012
- [6] P.J. Chen, D. Rodger, S. Saati, M. Humayun and Y.C. Tai, Microfabricated implantable parylene-based wireless passive intraocular pressure sensors, *Journal of Microelectromechanical Systems*, vol. 17, pp. 1342–1351, 2008
- [7] D.C. Rodger, A.J. Fong, W. Li, H. Ameri, A.K. Ahuja, C. Gutierrez, I. Lavrov, H. Zhong, P.R. Menon, E. Meng, J.W. Burdick, R.R. Roy, R. Edgerton, J.D. Weiland, M.S. Humayun and Y.C. Tai, Flexible parylene-based multielectrode array technology for high-density neural stimulation and recording, *Sensors and Actuators B: Chemical*, vol. 132, pp. 449–460, 2008
- [8] W. Li, D. Rodger, A. Pinto, E. Meng, J. Weiland, M.S. Humayun and Y.C. Tai, Parylene-based integrated wireless single-channel neurostimulator, *Sensors and Actuators A: Physical*, vol. 166, pp. 193–200, 2011
- [9] C.J. Lee, J.A. Vroom, H.A. Fishman and S.F. Bent, Determination of human lens capsule permeability and its feasibility as a replacement for Bruch's membrane, *Biomaterials*, vol. 27, pp. 1670–1678, 2006
- [10] T.L. Jackson, R.J. Antcliff, J. Hillenkamp and J. Marshall, Human retinal molecular weight exclusion limit and estimate of species variation, *Investigative Ophthalmology & Visual Science*, vol. 44, pp. 2141–2146, 2003
- [11] J.K. Armstrong, R.B. Wenby, H.J. Meiselman and T.C. Fisher, The hydrodynamic radii of macromolecules and their effect on red blood cell aggregation, *Biophysical Journal*, vol. 87, pp. 4259–4270, 2004
- [12] S. Zheng, H.K. Lin, R.J. Cote and Y.C. Tai, A novel 3D micro membrane filtration device for capture viable rare circulating tumor cells from whole blood, *Proc. of Hilton Head 2008*, Hilton Head Island, SC, USA, 2008, pp. 134–137
- [13] E.K. Purcell, J.P. Seymour, S. Yandamuri and D.R. Kipke, In vivo evaluation of a neural stem cell-seeded prosthesis, *Journal of Neural Engineering*, vol. 6, pp. 026005, 2009
- [14] J.R. Webster, M.A. Burns, D.T. Burke and C.H. Mastrangelo, Monolithic capillary electrophoresis device with integrated fluorescence detector, *Analytical Chemistry*, vol. 73, pp. 1622–1626, 2001

- [15] K.R. Hawkins and P. Yager, Nonlinear decrease of background fluorescence in polymer thin-films—a survey of materials and how they can complicate fluorescence detection in μ TAS, *Lab on a Chip*, vol. 3, pp. 248–252, 2003
- [16] A. Piruska, I. Nikcevic, S.H. Lee, C. Ahn, W.R. Heineman, P.A. Limbach and C.J. Seliskar, The autofluorescence of plastic materials and chips measured under laser irradiation, *Lab on a Chip*, vol. 5, pp. 1348–1354, 2005
- [17] C. Tung, R. Riehn and R.H. Austin, Complementary metal oxide semiconductor compatible fabrication and characterization of parylene-C covered nanofluidics channels with integrated nanoelectrodes, *Biomicrofluidics*, vol. 3, pp. 031101, 2009
- [18] Q.C. Quach and Y.C. Tai, A thermally improved quantitative PCR chip, *Proc. of Hilton Head 2008*, Hilton Head Island, SC, USA, 2008, pp. 264–267
- [19] M. Kochi, K. Oguro and I. Mita, Photoluminescence of solid aromatic polymers—1. Poly(*p*-xylylene), *European Polymer Journal*, vol. 24, pp. 917–921, 1988
- [20] G. Padmanaban and S. Ramakrishnan, Conjugation length control in soluble poly[2-methoxy-5-((2'-ethylhexyl)oxy)-1,4-phenylenevinylene] (MEHPPV): synthesis, optical properties, and energy transfer, *Journal of the American Chemical Society*, vol. 122, pp. 2244–2251, 2000
- [21] J.B. Fortin and T.M. Lu, Ultraviolet radiation induced degradation of poly-*p*-xylylene (parylene) thin films, *Thin Solid Films*, vol. 397, pp. 223–228, 2001
- [22] K.G. Pruden, K. Sinclair and S. Beaudoin, Characterization of parylene-N and parylene-C photooxidation, *Journal of Polymer Science Part A: Polymer Chemistry*, vol. 41, pp. 1486–1496, 2003
- [23] M. Bera, A. Rivaton, C. Gandon and J.L. Gardette, Comparison of the photodegradation of parylene C and parylene N, *European Polymer Journal*, vol. 36, pp. 1765–1777, 2000
- [24] M.C. Liu, D. Ho and Y.C. Tai, Monolithic fabrication of three-dimensional microfluidic networks for constructing cell culture array with an integrated combinatorial mixer, *Sensors and Actuators B: Chemical*, vol. 129, pp. 826–833, 2008
- [25] S. Zheng, H.K. Lin, J.Q. Liu, M. Balic, R. Datar, R.J. Cote and Y.C. Tai, Membrane microfilter device for selective capture, electrolysis and genomic

- analysis of human circulating tumor cells, *Journal of Chromatography A*, vol. 1162, pp. 154–161, 2007
- [26] B. Lu, S. Zheng, S. Xie and Y.C. Tai, Live capture of circulating tumor cells from human blood by a splittable 3D parylene membrane filtration device, *Proc. of μ TAS 2009*, Jeju, Korea, 2009, pp. 588–590
- [27] http://en.wikipedia.org/wiki/Electron_beam_physical_vapor_deposition, retrieved Apr 15th, 2012
- [28] T.Y. Chang, V.G. Yadav, S. De Leo, A. Mohedas, B. Rajalingam, C.L. Chen, S. Selvarasah, M.R. Dokmeci and A. Khademhosseini, Cell and protein compatibility of parylene-C surfaces, *Langmuir*, vol. 23, pp. 11718–11725, 2007
- [29] C.L. Chen, S. Jinno, H. Moller, B. Rajalingam, S.H. Chao, S. Selvarasah, A. Khademhosseini and M.R. Dokmeci, Multilayer parylene-C stencils for dynamically controlling cell interactions, *Proc. of MEMS 2008*, Tucson, AZ, USA, 2008, pp. 276–279
- [30] A.H. Cannon and W.P. King, Curvature affects superhydrophobicity on flexible silicone microstructured surfaces, *Proc. of Transducers 2009*, Denver, CO, USA, 2009, pp. 362–365
- [31] S. Zhu, Y. Li, J. Zhang, C. Lu, X. Dai, F. Jia, H. Gao and B. Yang, Biomimetic polyimide nanotube arrays with slippery or sticky superhydrophobicity, *Journal of Colloid and Interface Science*, vol. 344, pp. 541–546, 2010
- [32] B. Bhushan and E.K. Her, Fabrication of superhydrophobic surfaces with high and low adhesion inspired from rose petal, *Langmuir*, vol. 26, pp. 8207–8217, 2010
- [33] T. Ishizaki, N. Saito and O. Takai, Correlation of cell adhesive behaviors on superhydrophobic, superhydrophilic, and micropatterned superhydrophobic/superhydrophilic surfaces to their surface chemistry, *Langmuir*, vol. 26, pp. 8147–8154, 2010
- [34] K. Kuribayashi-Shigetomi, H. Onoe and S. Takeuchi, Self-folding cell origami: batch process of self-folding 3D cell-laden microstructures actuated by cell traction force, *Proc. of MEMS 2012*, Paris, France, 2012, pp. 72–75

CHAPTER 3

PARYLENE MEMBRANE FILTERS FOR CANCER DETECTION

3.1 Overview

According to the American Cancer Society, cancer is projected to be the leading cause of death worldwide in 2010 [1]. Metastasis is the spread of cancer from the primary site to non-adjacent secondary sites through a series of sequential steps [2]. Current studies indicate that this metastasis process includes localized invasion, intravasation, transport through circulation, arrest in microvessels, extravasation, formation of a micro-metastasis, and dormancy, and finally angiogenesis, colonization, and formation of a macro-metastasis [2]. Cancer metastasis is still the main cause of death for patients having solid-tumor cancers. Circulating tumor cells (CTC) are tumor cells disseminated from the primary tumor into blood stream. CTCs are prognostically

critical, associated with clinical stage, disease recurrence, tumor metastasis, treatment response, and patient survival following therapy [3-5]. There is a growing number of literature demonstrating CTC to be an emerging surrogate and independent marker for assessing the risk of relapse, guiding course of therapy, and monitoring treatment [2-6]. Therefore, the detection of CTCs in patient blood is significant in the diagnosis of cancer at the early stage of metastasis. However, there are two major challenges in CTC detection. First, CTCs are extremely rare, at the level of 1 CTC in 7.5 mL of blood (or 1 CTC against 10^{10} blood cells) [2], especially at the early state of cancer metastasis. Secondly, CTCs are very fragile, and are very likely to be damaged during the detection process itself [2].

It has been shown that the diameters of most types of CTCs are in the range of 15–30 μm [2,7]. Micromachined biomedical devices are a powerful tool for cell handling, sorting, and manipulation in this scale. When traditional methods, such as density gradient centrifugation, fail to efficiently enrich CTCs due to their rarity, BioMEMS technologies offer a new chance for CTC detection with good capture efficiency, enrichment, and throughput. In this chapter, various types of parylene membrane filtration devices are introduced, and their performances in CTC capture are evaluated. Two detection methods, including immunofluorescence enumeration and telomerase activity measurement, are used after CTC capturing. Besides capturing and detection, the feasibility of further culturing of captured CTCs is also demonstrated. In the end, efforts for high-viability capturing lead to the development of models for time-dependent cell membrane damage under mechanical tensions, which not only explain the viability loss during filtration, but also predict the “safe zone” for preserving the cell

viability.

3.2 Current Technologies for CTC Detection

3.2.1 Enriching methods

Due to their rarity, the first step of CTC detection is to enrich the CTCs from the other blood cells. There are three important parameters in evaluating this enriching step as shown in Eqs. 3-1, 3-2 and 3-3. Capture efficiency means the percentage of CTCs captured by the enriching devices. Enrichment indicates the capability of the devices to remove the normal blood cells. Clearly, a large enrichment is desirable since it helps to facilitate the following CTC detection step and improve the detection sensitivity by removing the disturbance of background red blood cells (RBCs) and white blood cells (WBCs). Viability is an evaluation of the device's capability in preserving the viability of CTCs during the enriching step. Viable capture is always preferable because it offers more options in further studies of the CTCs, including genomic analysis, culturing and anti-cancer drug screening. Another important parameter is the throughput of the enriching step. Due to the rarity of CTCs, usually large volumes of samples (in the range of 1–10 mL) need to be processed to collect enough CTCs for the downstream analysis. Enriching methods with low throughput may be good enough in the laboratory to prove the feasibility, but are definitely not ideal for real clinical applications.

$$\text{Capture Efficiency} = \frac{\# \text{ of CTCs captured on device}}{\# \text{ of CTCs in original blood sample}} \quad (3-1)$$

$$\text{Enrichment} = \left(\frac{\# \text{ of CTCs captured on device}}{\# \text{ of WBCs captured on device}} \right) / \left(\frac{\# \text{ of CTCs in original sample}}{\# \text{ of WBCs in original sample}} \right) \quad (3-2)$$

$$Viability = \frac{\# \text{ of viable CTCs captured on device}}{\# \text{ of CTCs captured on device}} \quad (3-3)$$

Current CTC enrich technologies include the traditional density gradient centrifugation [8], immunomagnetic separation [9], microfluidic devices combined with immunoaffinity based selection [10], and size-based filtration [2,7,8]. The representative example of immunomagnetic separation is the CellsearchTM system, which is the only FDA-approved automated system to capture and assess CTCs for prognosis and treatment monitoring. Immunomagnetic separation usually takes advantage of specific epithelial surface antigens such as epithelial cell adhesion molecule (EpCAM). First, EpCAM-conjugated magnetic beads are added into blood sample. After incubation, CTCs are adhered to the beads and captured by collecting the magnetic beads under magnetic field. Although plenty of clinical studies substantiate its prognostic value, the assay is very expensive, labor intensive, and subject to a large range of reported capture efficiency (9%–90%) [9], mainly due to the variable expression of surface markers. An immunoaffinity-based “CTC chip” was invented in 2007 [10], where CTCs are captured with antibodies conjugated to surface of microposts in a microfluidic chamber. This CTC chip has successfully demonstrated CTC capture and detection from patient samples of multiple metastatic cancers [10,11]. While viable CTCs with high enrichment can be obtained, the capture efficiency is limited by the variability of surface antigen expression and the throughput (or the processing time) is limited by allowable maximal flow rate and incubation time.

Alternatively, capturing of CTC based on cell size has been demonstrated to be a potentially efficient, inexpensive, and quick means of CTC enrichment [8,12–14].

Circulating tumor cells (15–30 μm in diameter) are in most of the cases epithelial cells and believed to be significantly larger than the surrounding blood cells [8,12–14]. Various size-based devices can be summarized into two categories, the lateral filtration devices and the membrane filtration devices. Most lateral filtration devices are derived from microfluidic technologies. One representative example is the PDMS microdevices with asymmetrically arranged “traps” reported in [14]. Lateral filtration can ensure good capture efficiency and viability, sometimes even high enrichment, if EpCAM is pre-coated to the microfluidic channel walls as the immunoaffinity-assisted filtration [14]. However, the biggest problem of such devices is their low throughput. For the device mentioned above, flowing of 5 mL of sample through three devices in parallel at the same time takes about 2.5 h. Although this is considerably shorter than most leading techniques using immunomagnetic- or immunoaffinity-based methods, the processing time is still too long for real clinical use.

Another more advantageous size-based enriching method is membrane filtration. Unlike lateral filtration, membrane filtration has a large sample processing area, hence the throughput is usually high. Most previously reported membrane filtrations [8,12,13] are based on commercially available polycarbonate filters that are fabricated using track etching. Track etching can only generate pores at random locations. Low pore density and multiple pore fusion lead to low CTC capture efficiency ($\sim 50\text{--}60\%$) and frequent sample clogging on the filter [9]. In the remaining sections of this chapter, we will describe the micromachined parylene filters with regular high-density micro pores or slots, which have more than 90% capture efficiency. Despite its advantage in throughput, the membrane filtration method is disadvantageous for its poor enrichments. The blood

cells left on the filter can be a source of noise in the following CTC detection step. However, several approaches to improve the enrichment will be discussed in a latter section. Table 3-1 summarizes and compares the advantages and disadvantages of various CTC-enriching technologies.

Table 3-1: Comparisons of various CTC-enriching technologies

	Density Gradient Centrifugation	Immunomagnetic Separation	Immunoaffinity-Based Selection	Size-Based Filtration	
				Lateral Filtration	Membrane Filtration
Capture Efficiency	Low	Medium	Medium	Medium to High	Medium to High
Enrichment	Low	High	High	Low	Low
Viability	Usually Low	Usually Low	Depends	Depends	Depends
Throughput	Low	Very Low	Very Low	Medium	High
Cost	Medium	High	High	Low	Low

3.2.2 Detection methods

After capturing the CTCs and eliminating the blood cells, the second step is to detect the presence of the CTCs. Currently, immunofluorescence detection and telomerase-activity detection are two leading technologies. Immunofluorescence detection dominates in today's clinical applications and is largely dependent on the cell types and the expression of certain antigens. There is a large selection of immune biomarkers which usually target cytokeratins (CK) (epithelial tumor cells), EpCAM (epithelial cells), PSA (prostate cancer cells only), or any other surface antigens. These fluorescence-conjugated biomarkers are usually allowed to bind to the target CTCs before or during the sample processing. After capturing, the immunofluorescence-

labeled CTCs are visible under fluorescence microscope. However, the immunofluorescence detection is limited to the availability of immunomarkers and certain types of CTCs. For example, the immunoaffinity-based CTC chip [10] is only able to detect EpCAM-expressing tumors. Moreover, most immunofluorescence methods only enumerate the captured CTCs, in the absence of any other further information.

These limitations can be surmounted by measuring the telomerase activity from the captured cells. As a CTC biomarker, telomerase activity offers several advantages [15]: (a) it is a widely applicable tumor marker with validated diagnostic and prognostic utility in multiple cancer types; (b) it is a uniquely “functional” assay that reflects the presence of live cancer cells; (c) it can be amplified and measured accurately from small numbers of cells using quantitative PCR (qPCR) without the need to visualize or count the cells; and (d) it can be scaled-up cheaply and rapidly to yield quantitative, operator-independent results.

In the following sections, we will show the demonstration of both detection methods and the results of their clinical trials, respectively.

3.3 Parylene Membrane Filters

3.3.1 Parylene: An ideal membrane filter material

Parylene-C was chosen as the filter material because of its unique properties. Its mechanical strength ensures the integrity of the filter during pressure-driven filtration. Under low drive pressure, parylene membrane is stiff enough with little deflection, ensuring that the size of openings is almost independent from the pressure loading. It is

optically transparent in the visible range, which facilitates direct pathological observation of stained cells under microscope. It is inert to most of the chemicals and solvents used in standard chemical and biological laboratories. Moreover, its biocompatibility makes parylene-based devices suitable for further cell culture applications. Finally, high-quality pin-hole free parylene thin film can be obtained with room-temperature chemical vapor deposition (CVD), and further patterned with lithography and oxygen plasma by reactive ion etching (RIE). This machinability makes parylene superior to other filter materials, such as polycarbonate, polyester, or Teflon. The well-developed parylene microfabrication technologies are able to precisely control the size of openings, and create a much higher density of openings than the track-etching method used in manufacturing other membrane filter materials.

3.3.2 1st generation: 2D pore filter

The 1st generation of parylene membrane filter aimed to overcome the disadvantages of the track-etched polycarbonate filters by increasing the pore density and reducing the possibility of fused pores, thus improving the capture efficiency. The fabrication process started with an 8- μm -thick parylene deposition on HMDS-coated silicon wafer, followed by aluminum deposition as the etching mask. Standard lithography and wet-etching transferred the pattern on the mask to the pattern on the aluminum layer. A through-hole was made in the parylene layer by RIE with O_2 plasma. Finally, after removing the metal mask, the parylene membrane was peeled off from the silicon substrate. The pore diameter was 8 μm , which was optimal according to [13]. SEM images of the fabricated filter are shown in Fig. 3-1.

In order to test the performance of the filter, a model system was built by spiking a known number of LnCaP cancer cells into phosphate buffered saline (PBS) or blood samples. Before spiking, cancer cells were first fixed with formalin and stained with hematoxylin. A membrane filter was clamped in-between two PDMS chambers and further sandwiched between two acrylic sheets with center holes. Sample was manually driven through the filter with a syringe. The capture efficiency was measured to be $87.3\pm 7.0\%$.

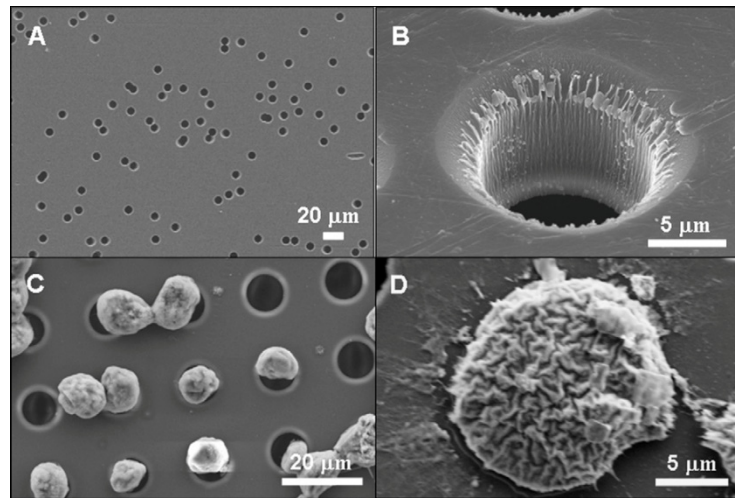


Figure 3-1: SEM images of 2D pore filters. (a) track-etched polycarbonate filters with randomly sparse pores; (b) microfabricated parylene filter with precisely defined pores; (c) LnCaP cancer cells captured on the filter; (d) a close-up view of a captured cancer cell

One problem with the 2D pore filter was that it failed to capture viable cancer cells. Before filtration, the fixation step was necessary to keep the integrity of the cells. The fixed cells, however, lost their viability, thus disallowing further analysis or studies requiring live cells. As shown in Fig. 3-2, unfixed cells were easily damaged or even totally lysed on the filter. The cytoplasm of cells was prestained with the fluorescent dye

Calcein-AM. It can be observed from the picture that the dye leaked out from the compromised cell membrane. The reason for this unpleasant cell lysis has been found to be related to both the geometry of the circular pore opening and the simple filtration setup. Precise pressure control was impossible with this manual system, making the cell membrane tension unpredictable and uncontrolled.

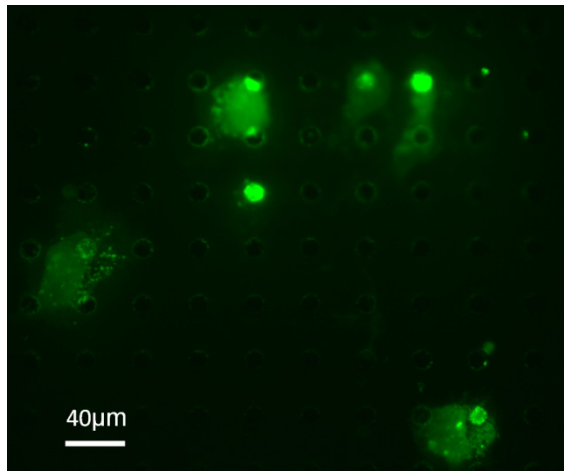


Figure 3-2: Cells were partially damaged or totally lysed after filtration

3.3.3 2nd generation: 3D pore filter

A direct suggestion from Fig. 3-2 was that the damage of captured cells was caused by the lack of mechanical support from the bottom; this gave birth to the dual-layer 3D pore filter. Through-holes were created in both the top and bottom parylene layers, with misaligned locations, as shown in Fig. 3-3. The top and bottom pores had diameters of 9 μm and 8 μm , respectively. The gap between two parylene layers was 6.5 μm , which prevented the large deformation of captured CTCs, but allowed the transportation of blood cells. In order to maintain the gap distance during filtration, each cavity was arranged into 99 hexagonal microfilter patches, as in Fig. 3-3(b).

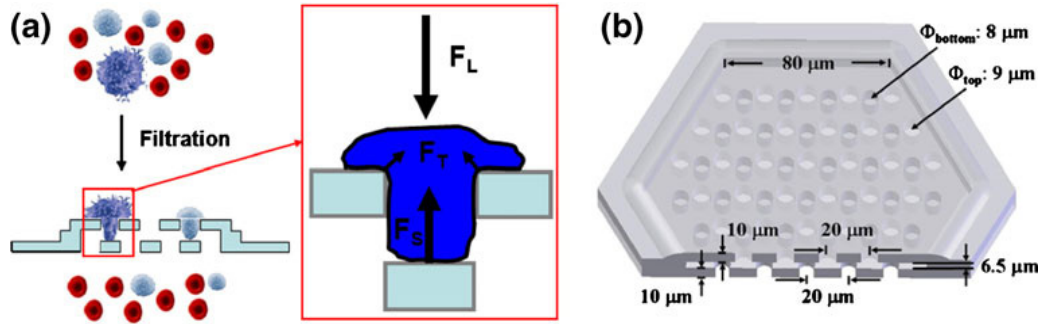


Figure 3-3: 3D pore filter design. (a) filtration process and forces on a trapped cell. (b) design of a single hexagon-shaped microfilter patch

Fig. 3-4 shows the fabrication process flow of the device. The detailed fabrication process was illustrated in [2]. Silicon was etched by tetramethylammonium hydroxide (TMAH) to form the cavity patterns, which worked as a mesh frame to provide mechanical support during handling and operation. After releasing the photoresist, the device went through a 190°C parylene annealing step to strengthen the overall structure. The fabricated device is shown in Fig. 3-5.

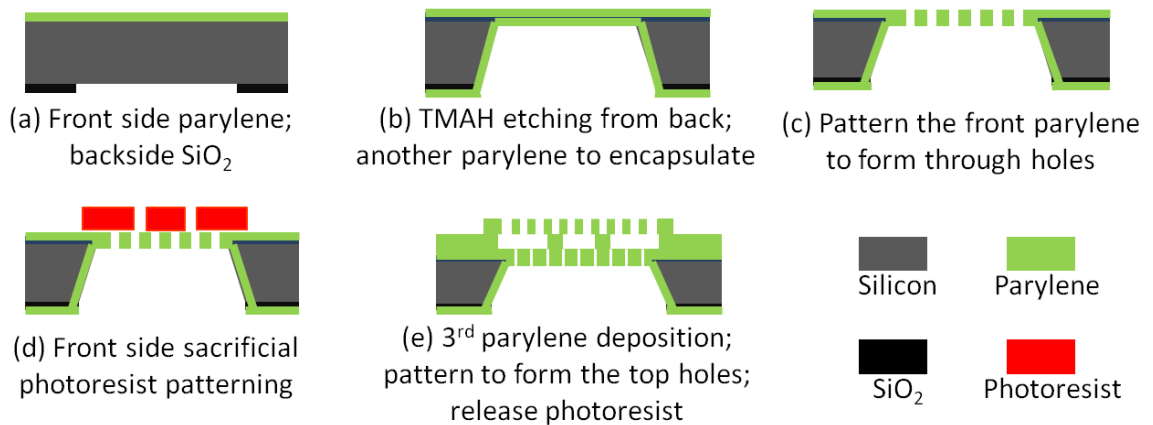


Figure 3-4: Fabrication process flow of the 3D pore filter

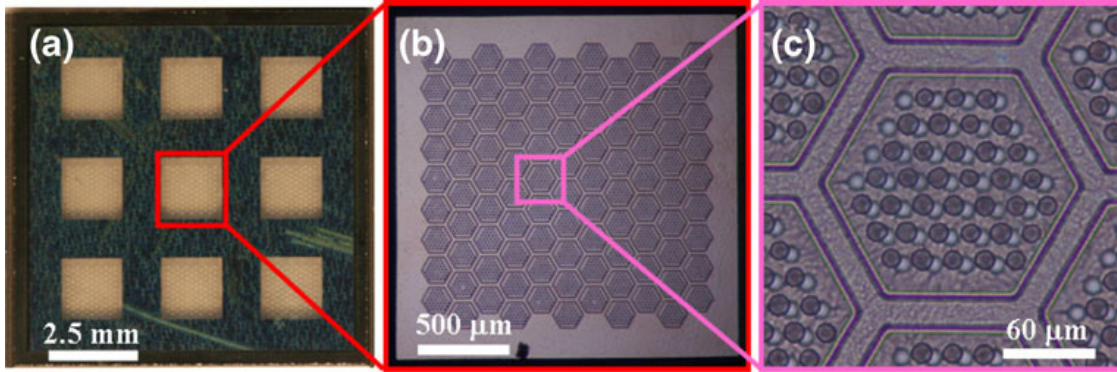


Figure 3-5: Photos of the fabricated 3D microfilter. (a) the overall device, (b) one open window, and (c) one patch

MCF-7 human breast cancer cells were stained with carboxyfluorescein diacetate, succinimidyl ester (CFDA-SE, Invitrogen) before being spiked into a 1 mL 1:10 diluted blood sample. Filtration was carried out with the setup shown in Fig. 3-6. After filtration, the capture efficiency was calculated to be $86.5 \pm 5.3\%$ by manually counting the number of fluorescence-labeled cells retained on filter.

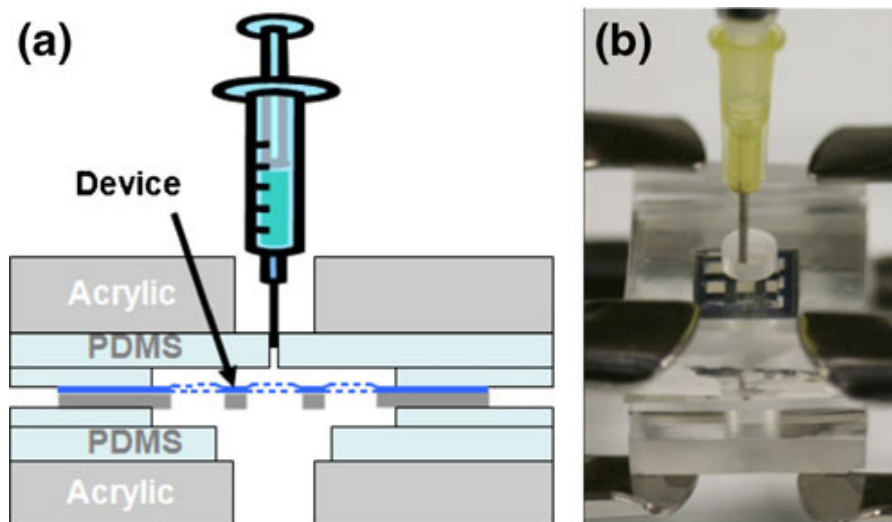


Figure 3-6: Device is assembled inside a housing cassette

A side-by-side comparison was performed between 2D and 3D microfilter devices by filtering unfixed, viable, CFDA-SE-labeled MCF-7 cells under the same flow rates. The 2D filter failed to retain intact cells as shown in Fig. 3-7(b) in comparison to a positive control prepared by pipetting a droplet of buffer containing labeled cells onto a 2D filter without filtration (Fig. 3-7(a)). Faint green fluorescence could be observed on the 2D filter coming from the edges of pores, which were later confirmed by SEM to be cell membrane remnants (Fig. 3-7(b), inset). On the contrary, the 3D filter could capture MCF-7 cells while preserving cell membrane integrity, as demonstrated by the bright green fluorescence, indicating intact cytoplasm, as shown in Fig. 3-7(c). This direct comparison clearly demonstrates the capability of the 3D filter to capture viable unfixed cells. The integrity of captured cell was further confirmed by the SEM images in Fig. 3-8.

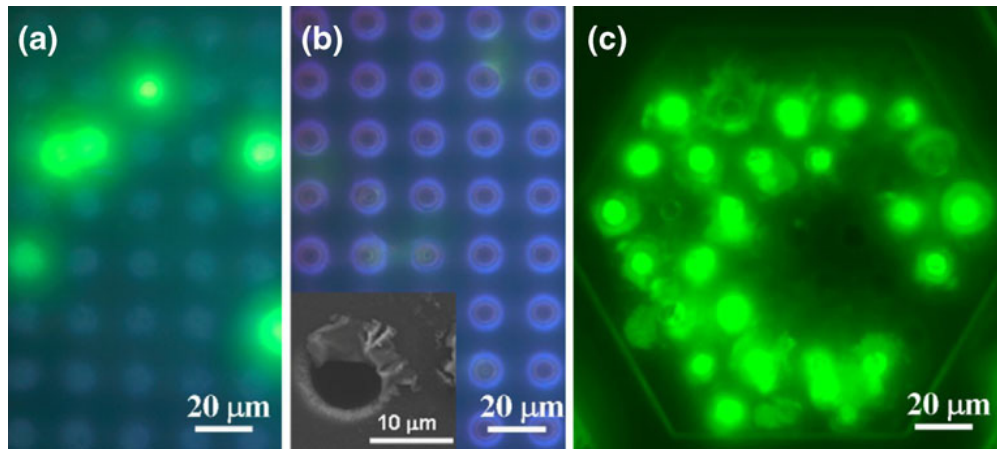


Figure 3-7: Comparison of 2D and 3D filters with unfixed CFDA-SE-labeled MCF-7 cells. (a) cells loaded on top surface of a 2D filter device. (b) cells filtered through a 2D filter device. (c) cells filtered through a 3D filter device

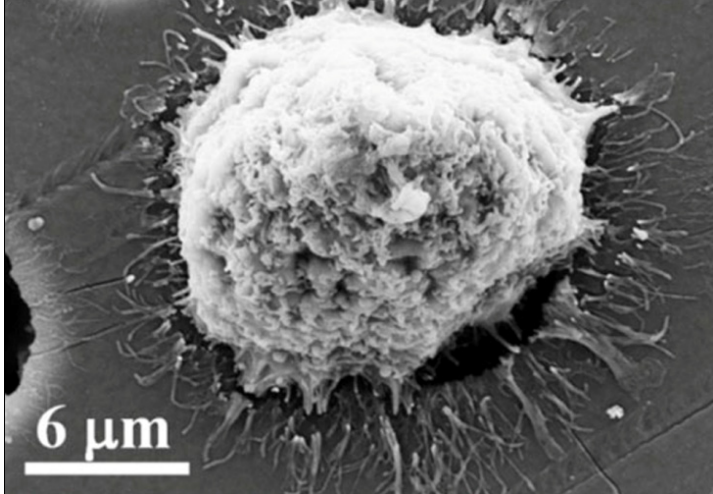


Figure 3-8: SEM image of a MCF-7 cell captured on the 3D pore filter

3.3.4 3rd generation: 3D gap filter

It would be very helpful if the captured CTCs could be released and collected for further applications, such as cell culturing, genomic analysis, or anti-cancer drug screening, which definitely disclose more information about the cancer metastasis than just the enumeration of CTCs. Although the 3D pore filter was able to capture viable CTCs, it was very difficult to release the captured cells from it. To make release possible, the 3rd generation of filter was invented. It was still a dual-layer 3D filter but the mechanism of CTC capture was different. As shown in Fig. 3-9, the new 3D gap filter had much larger pore openings in the top layer. The CTCs were trapped by the gap, rather than the holes. In addition to its novel capturing mechanism, the filter was also able to be detached into top and bottom layers to further facilitate the release of trapped cells.

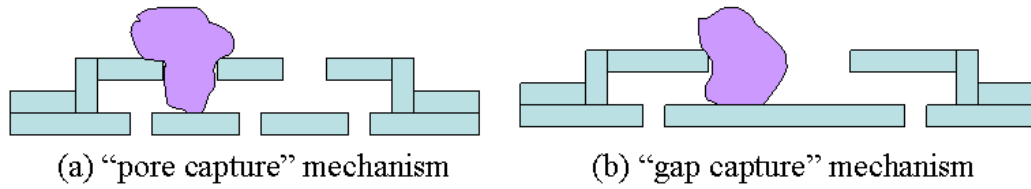


Figure 3-9: Comparison of “pore capture” and “gap capture” mechanisms

The fabrication process flow of this 3D gap filter was very similar to the previous 3D pore filter, as shown in Fig. 3-10. There were two remarkable differences. First, the device was peeled off from the silicon substrate in the last step. This all-parylene filter was fully biocompatible, which was advantageous in the CTC capture and culture applications. Secondly, in step (c), interface treatment was performed to reduce the adhesion between two parylene layers. It was found that 10% HF surface cleaning before the second parylene deposition made sure the filter could survive the handling and filtration process, but was easily separated after filtration, as shown in Fig. 3-11.

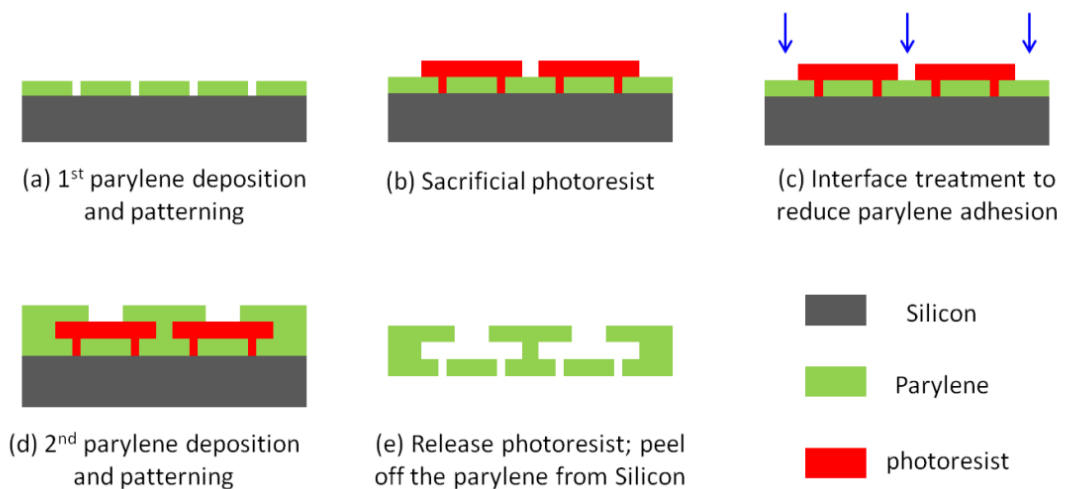


Figure 3-10: Fabrication process flow of the 3D gap filter

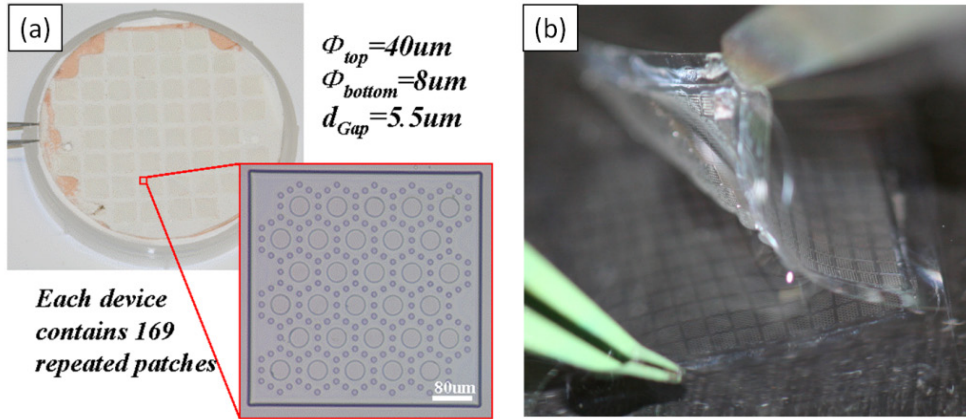


Figure 3-11: Photos of the 3D gap filter. (a) The fabricated 3D gap filter. (b) Demonstration that the filter can be mechanically separated by tweezers.

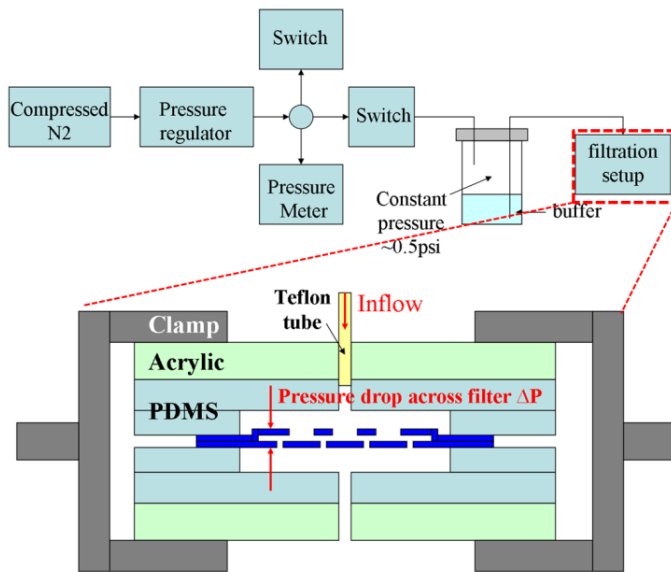


Figure 3-12: Filtration setup using constant pressure driving

For previous filters, samples were hand-pushed through the device. During filtration the transfilter pressure (ΔP) was difficult to control and cancer cells might be damaged by high cytoplasm membrane tension caused by a large ΔP . An improved experimental setup using constant pressure (~ 0.5 psi) to drive samples through the filter

was used here in order to ensure low membrane tension and high cancer cell viability (Figure 3-12).

The human DU145 prostate cancer cell line was used for testing. Capture efficiency was measured for filters with different gap sizes by adding a known number of cancer cells into PBS suspension (Table 3-2). A device with a 5.5 μm gap size was selected, which had $88.6\pm 3.8\%$ capture efficiency and could handle 7.5 mL undiluted whole blood without a clogging problem. To check the cell viability after filtration, captured cancer cells were stained on-chip with 0.4% Trypan Blue. $86.9\pm 4.4\%$ cancer cells were alive after filtration. A model system was formed by spiking Red CMTPX fluorescent dye pre-labeled cancer cells into diluted human blood. Live cells with intact membranes can keep fluorescence dye inside and will fluoresce, while dead cells become dim due to dye leakage. After filtration using the model system, cancer cells stayed alive and fluoresced brightly (Figure 3-13).

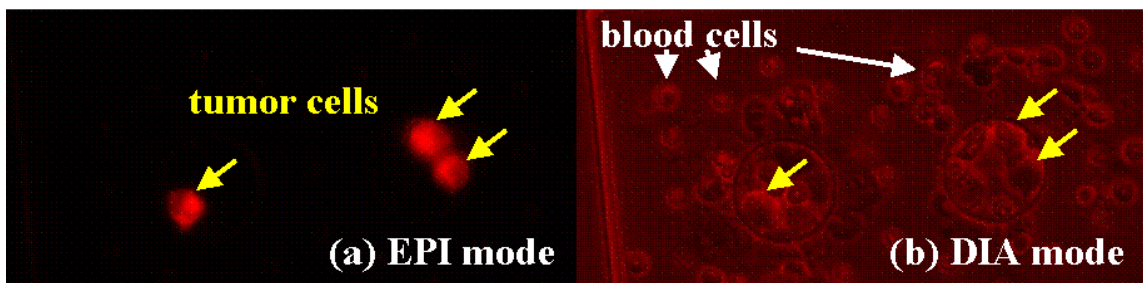


Figure 3-13: Fluorescent image of a model system testing (tumor cells spiked in 1 mL ten times diluted human blood). Only pre-labeled tumor cells could be seen in (a), while surrounding blood cells could also be seen in (b).

Table 3-2: Capture efficiency with different gap sizes

Gap size (μm)	4.24	5.50	6.00	6.67
Efficiency (%)	89.6 \pm 5.0	88.6 \pm 3.8	83.7 \pm 6.8	76.3 \pm 4.9

After filtration, two methods could be used to release the cells. Since under low drive pressure, the cells were only loosely trapped at the edge of the gap, they were easily swept off from the filter by a small brush (Fig. 3-14). An alternative method was to first detach the top and bottom layers, and then release the cells with multiple rinsing steps.

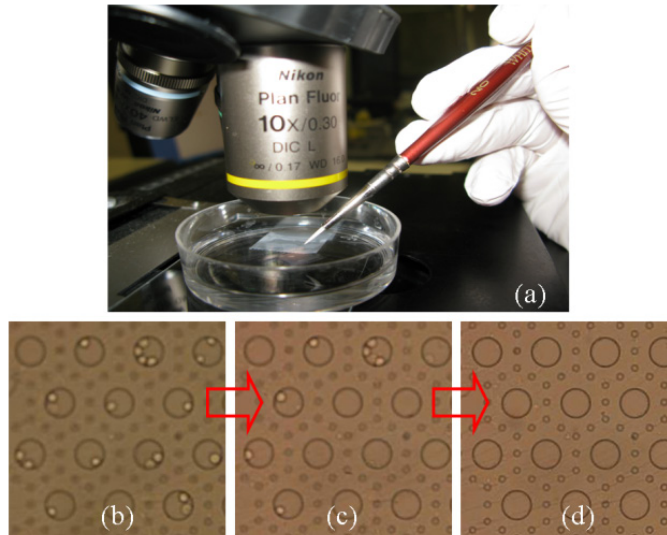


Figure 3-14: Release of trapped tumor cells from filter using a brush

Although both types of 3D filters are able to preserve the high viability of captured cancer cells, the biggest problem with the dual-layer 3D filter is its low enrichment. Compared to the single-layer filter, the top layer and the gap of the 3D filter exist as two additional barriers for blood cell passage. Many blood cells, especially some large WBCs, are retained inside the gap of filter due to mechanical blocking or by the

adhesion between cells and parylene. Fig. 3-15 shows that a large number of blood cells were also trapped on the filter, which would be the undesirable background noise in the following detection step.

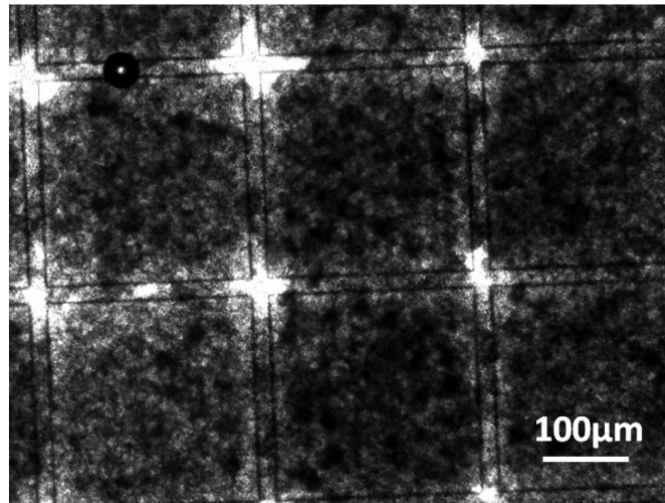


Figure 3-15: The low enrichment of the 3D pore filter

3.3.5 4th generation: 2D slot filter

Due to the low enrichment of 3D filters, the next design goes back to the single-layer 2D filter. However, the geometry of openings is changed from circular pores to rectangular slots. The slot filter is considered to be better than the pore filter in preserving the viability of captured CTCs, because the interstitial space between the slot and captured cells reduces the transfilter pressure difference [16], which in turn means a smaller tension on the cell membrane. In our design, the length of each slot was 40 μm , while the slot width was 6 μm , optimized by enumeration experiments. The open-factor, defined as the ratio of opening areas over the total area, was 18–42% depending on different applications, much larger than previous “pore” filters. The fabrication process

flow of this filter was essentially the same with the 2D pore filter. Fig. 3-16 shows the SEM image of a fabricated slot filter, as well as a constant-pressure-driven filtration system with improved membrane sealing.

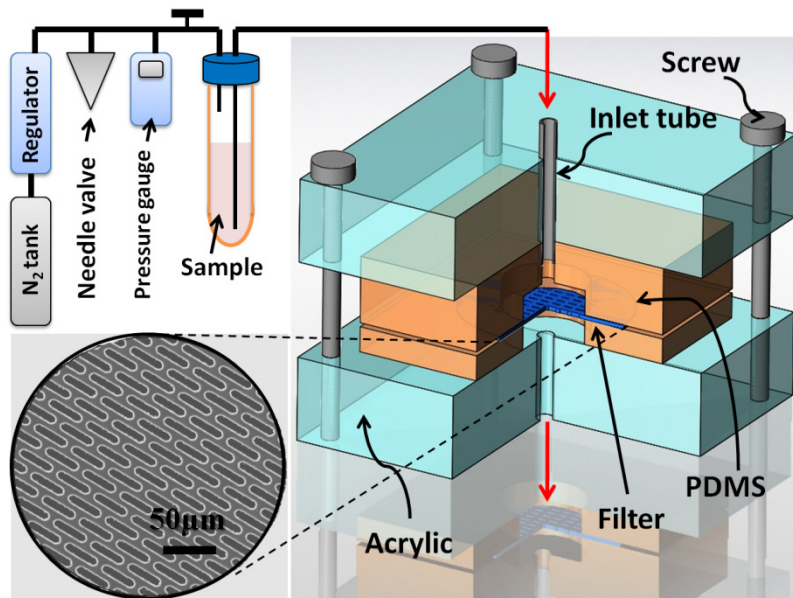


Figure 3-16: Constant-pressure-driven filtration system, the filter assembly, and the SEM image of fabricated slot filter

Human prostate cancer PC-3 cells were cultured in RPMI 1640 culture medium supplemented with 10% fetal bovine serum at 5% CO₂ and 37 °C. For filter device testing, harvested cells were first stained with Calcein-AM fluorescent dye (Invitrogen, Carlsbad, CA, USA), centrifuged, and then resuspended in phosphate buffered saline (PBS) before testing. A known number of cancer cells were spiked into 1 mL human whole blood obtained from a healthy donor. After filtration, captured cancer cells were counted under epifluorescence microscope. The viability of captured cancer cells was evaluated by on-filter staining with propidium iodide (PI) (Invitrogen). Enrichment was

determined by staining white blood cells (WBCs) captured on the filter with Acridine Orange (AO) (Invitrogen), followed by WBC counting. To observe the morphology of captured cancer cells, cells on the filter went through the paraformaldehyde-glutaraldehyde fixation, multiple rinses, dehydration, air dry, and sputter metal coating, and finally were imaged using a scanning electron microscope (SEM, JEOL JSM/6390LV).

Three kinds of slot filters with different slot widths, 5 μm , 6 μm and 7 μm , were tested for their capture efficiency, viability, and enrichment, which are defined in Section 3.2.1 (Fig. 3-17). Since the slot widths we studied were substantially smaller than PC-3 cancer cell size ($\sim 17 \mu\text{m}$ in diameter), different slot widths did not cause significant variation of capture efficiency (Fig. 3-17(a)). Cancer cell viability was evaluated by both Calcein-AM and PI staining (Fig. 3-18(a) and (b)). Viable cancer cells with intact cell membrane were able to retain Calcein-AM, and thus fluoresced bright green. Dead cancer cells with compromised cell membrane were stained by red-fluorescent nuclear dye PI, while the green fluorescence became faint due to Calcein-AM dye leakage. A remarkable drop of viability was observed when the slot width increased to 7 μm (Fig. 3-17(a)). Under flow pressure and shear stress, captured cancer cells were forced to stretch and partially deform into the slot if the slot was too wide. In this condition, the rupture of cell membrane and the internal damage of the cell were possible reasons for the drop of viability. A noticeable reduction of capture efficiency can be predicted if the slot width further increases and cancer cells are able to deform through the slot. A clear discrepancy in enrichment appeared between 5 μm and 6 μm slot widths (Fig. 3-17(b)). This difference was probably due to some large monocytes (12–20 μm) [7], which may

have threshold passage width between 5 μm and 6 μm . Based on above analysis, the filter with the 6 μm slot width was the optimal design, since it had over 90% capture efficiency and viability, with more than 200-fold enrichment.

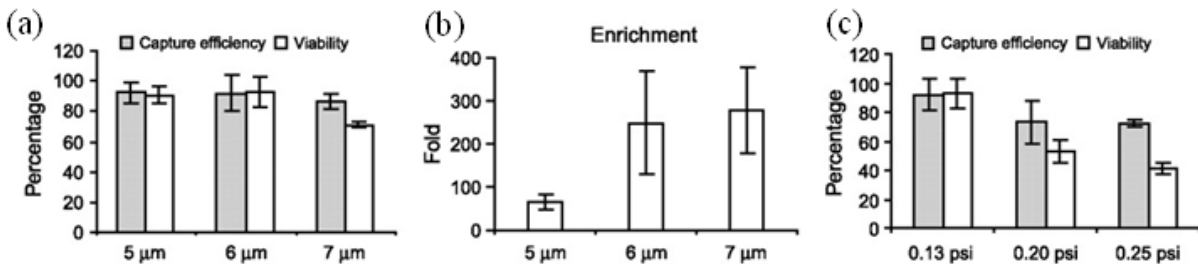


Figure 3-17: 2D slot filter characterization: (a) and (b) capture efficiency, viability, and enrichment with slot size at the same drive pressure of 0.13 psi; (c) capture efficiency and viability with drive pressure with the same slot width of 6 μm

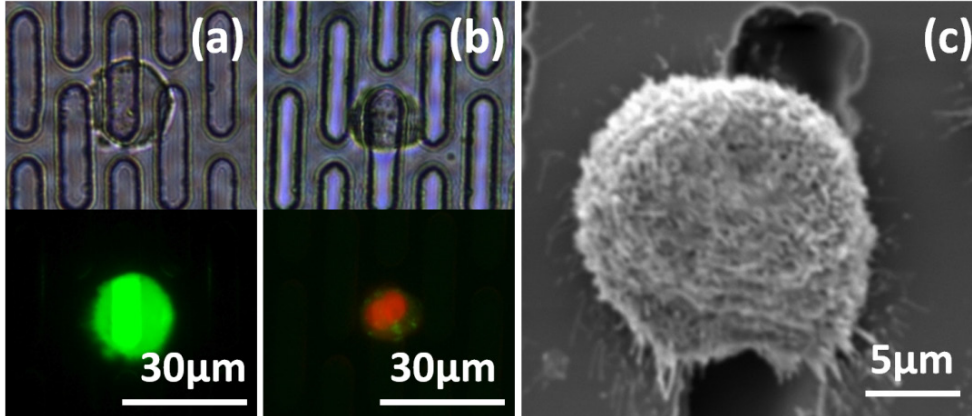


Figure 3-18: Cancer cells captured on the slot filter. (a) live cell retained Calcein-AM. (b) dead cell was stained with PI. (c) SEM image shows captured cell was still in spherical shape.

Filter performance under different drive pressures was also examined. As drive pressure increased, both capture efficiency and viability decreased (Fig. 3-17(c)). Hence

low drive pressure was critical for live cell capture. Experimentally, 0.13 psi was found to be the optimal drive pressure for high viability and successful sample processing. Filtration of a 1 mL sample under the optimal conditions took less than 5 minutes. The morphology of the captured cancer cells remained unharmed, as indicated by SEM (Fig. 3-18(c)).

3.4 Experiment Results and Clinical Trials

3.4.1 Immunofluorescence method

The clinical trials using 2D pore filters were aimed at detecting the CTCs from patient blood samples, which were performed in the collaboration with the University of Southern California and the University of Miami. The viability of CTCs was not the primary concern of these trials, since the diagnosis of cancer was mainly confirmed by the immunofluorescence enumeration. For this non-viable detecting, 2D pore filters worked and were able to generate reliable results.

Cancer cells were identified and distinguished from leukocytes based on morphology and differential antigen expression. Cancer cells are epithelial, and express cytokeratin (CK), while leukocytes are non-epithelial, and are negative for CK. Immunofluorescence was performed directly on the filter membranes for the expression of CKs. Filter membranes were placed on top of microscope slides and blocked with normal horse serum for 20 min. A cocktail of two different mouse monoclonal antibodies against CKs was used for the detection of epithelial tumor cells: AE-1 (1:600 dilution, Signet, Dedham, MA, cat. # 462-01) against low and intermediate Type I acidic keratins, and CAM 5.2 (1:100 dilution, Beckton-Dickinson) against CK 8 and 18. The

slides were incubated for 1 hour in the cocktail of primary antibodies diluted in CheMate antibody diluent (DakoCytomation). Subsequently, the slides were washed and incubated for 1 hour with fluorescent, Alexa Fluor 488 conjugated goat anti-mouse secondary antibody (Invitrogen). For samples collected from patients with castration-resistant prostate cancer, the entire procedure was repeated using rabbit polyclonal antibodies against PSA (Dako, Denmark), followed by Alexa Fluor 594 conjugated goat anti-rabbit secondary antibody (Invitrogen) to confirm that the CK positive cells were of prostate origin. Membrane on slides were coverslipped using Vectashield® (Vector Laboratories) mounting medium containing 4',6-diamidino-2-phenylindole for nuclear staining and then sealed with nail polish. Immunofluorescence images were obtained using Leica DM LB2 microscope equipped with Diagnostic Instruments 7.3.3 color camera viewed with Chroma filter sets consisting of excitation filters of 480/40 and 560/55, dichroic filters of 505 and 595 long pass, and emission filters of 535/50 and 560/55. Cells were imaged directly on filter membranes placed onto microscope slides.

Cancer cells were identified and distinguished from leukocytes by expression of CK antigens by immunofluorescence; epithelial tumor cells are CK positive, while leukocytes are CK negative (Fig. 3-19(a)). Moreover, CK-positive CTCs captured from prostate cancer patients were imaged on membrane, showing both prostate specific antigen (PSA) positive (Fig. 3-19(b)-(c)) and negative (Fig. 3-19 (d)) CTCs. We also examined negative control samples from 10 healthy individuals and none of the samples from healthy subjects had any detectable CTCs.

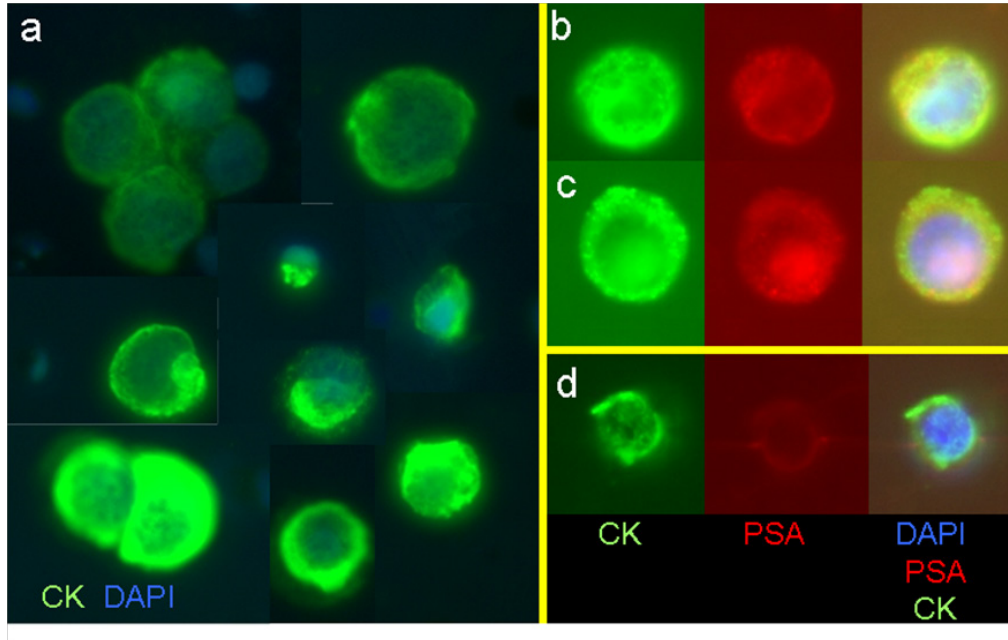


Figure 3-19: On-filter immunofluorescence staining of captured CTCs [17]

We also compared the performance of the microdevice for enumeration of cancer cells against a commercially available platform, the FDA-approved CellSearch® system [17]. As shown in Fig. 3-20, the microfilter device outperformed the CellSearch® system in terms of recovery rates for all cancer types. When CTC were detected by both methods, greater numbers were recovered by the microfilter device in all but 5 patients. Immunomagnetic bead-based and carbon micropost enrichment methods depend on the expression of a specific surface antigen, EpCAM on the target tumor cells. EpCAM is expressed by only 75% of 134 epithelial tumors [18]. In contrast, the microdevice exploits the inherent larger size of cancer cells and captures EpCAM positive and negative cancer cells. In addition, the ability to capture and characterize CTCs on a single platform simplifies the processing and prevents loss of cells, yielding high recovery rates.

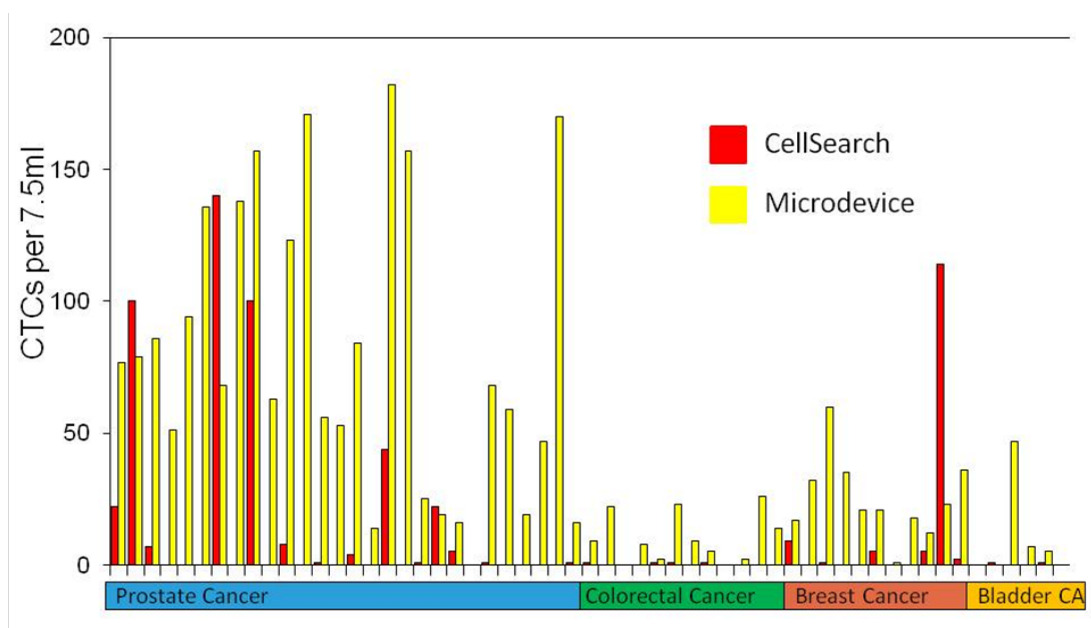


Figure 3-20: Histogram demonstrating performance comparison of membrane microfilter vs. CellSearch® assay in clinical samples [17]

3.4.2 Telomerase activity detection

Since the telomerase activity is usually only detectable from viable cells, only the 2D slot filter is applicable for this detection method. Telomerase activity from cell extracts was analyzed using a previously described real-time PCR-based telomeric repeat amplification protocol (TRAP) [19].

We tested whether telomerase activity could be detected from live-captured cancer cells by spiking DU145 prostate cancer cells into 7.5 mL of whole blood, then lysing the live-captured cells on the filter and analyzing the lysate by qPCR-TRAP (Fig. 3-21(a)). Remarkably, this method was capable of detecting as few as 25 cancer cells added to 7.5 mL of whole blood (Fig. 3-21(a), $P = 0.01$ for each spiked sample compared with blood only), and the threshold cycle (Ct) value was inversely proportional and linearly correlated with the number of spiked cells (Fig. 3-21(b)).

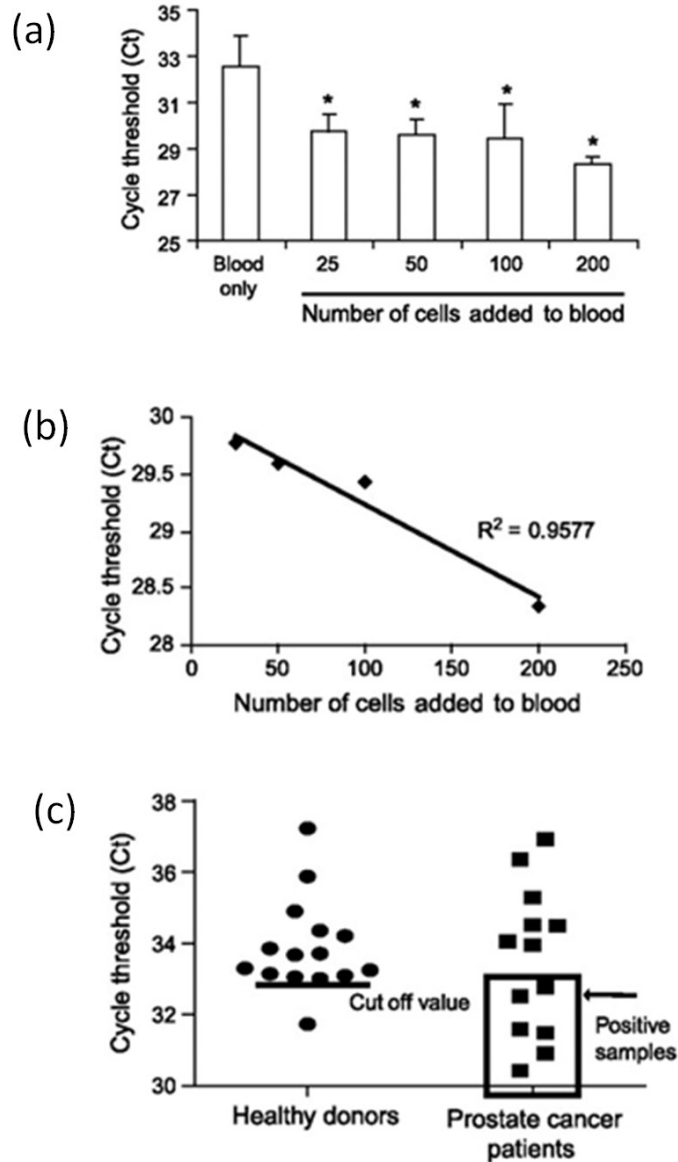


Figure 3-21: Detection of telomerase activity from live cancer cells captured on a slot microfilter. (a) telomerase activity detected from 7.5 mL blood samples spiked with a range of cancer cell numbers or blood only ($P = 0.01$ for each sample compared with blood-only sample). (b) linear correlation of Ct values with the number of cells added. All histogram results are by means of triplicate independent experiments. (c) telomerase activity of patient samples vs. healthy donor controls. The line in healthy donors indicates the calculated true negative Ct cutoff value of 33; patient samples falling within the positive range ($Ct < \text{cutoff value}$) are boxed.

We conducted a limited proof-of-principle experiment wherein blood samples from 15 healthy donors and 13 cancer patients were tested (Fig. 3-21(c)) using slot microfilter capture and qPCR-TRAP. Among healthy donors, the average Ct was 33.9 ± 1.32 . To maximize assay specificity based on this true negative cohort, we defined Ct = 33 as the cutoff threshold for a positive telomerase activity assay, thus yielding a specificity of 93% (95% confidence interval, 68–100%) within the training set of healthy donors. When a test cohort of patient samples was tested using this cutoff, 6 of 13 patients were found to have Ct values below the threshold of Ct = 33. These six patients with positive CTC telomerase activity assays had a mean Ct of 31, ~ eightfold telomerase activity relative to the mean telomerase activity of the healthy control cohort.

We also tested whether the platform would support single-cell analysis of live-captured cells. PC-3 cancer cells were captured from whole blood on microfilter, localized by immunofluorescent staining (PE-conjugated anti-CD49 antibody), and recovered individually using a micropipette mounted onto a XYZ manipulating stage (Fig. 3-22). Single cancer cells were deposited in CHAPS lysis buffer and subjected to qPCR-TRAP, which yielded a significantly elevated telomerase activity level relative to negative controls.

Measurement of telomerase activity from live CTCs on the slot microfilter constitutes a tumor biomarker strategy with broad applicability. Telomerase activity is a well-recognized cancer marker in > 90% of human malignancies [20] and therefore is ideally suited to the microfilter, which can capture CTCs across all tumor types, regardless of surface markers. Telomerase activity also constitutes a uniquely “functional” assay which reflects the presence of live cancer cells. Moreover, qPCR-TRAP can

amplify the telomerase activity signal from as few as one cancer cell, raising the prospect of applying CTC-telomerase to early detection of occult malignancy. Low-pressure slot microfiltration offers new and versatile capabilities for live CTC capture and analysis. The detection of telomerase activity highlights the potential utility of this novel platform, which can be applied to advance cancer research and enhance patient care.

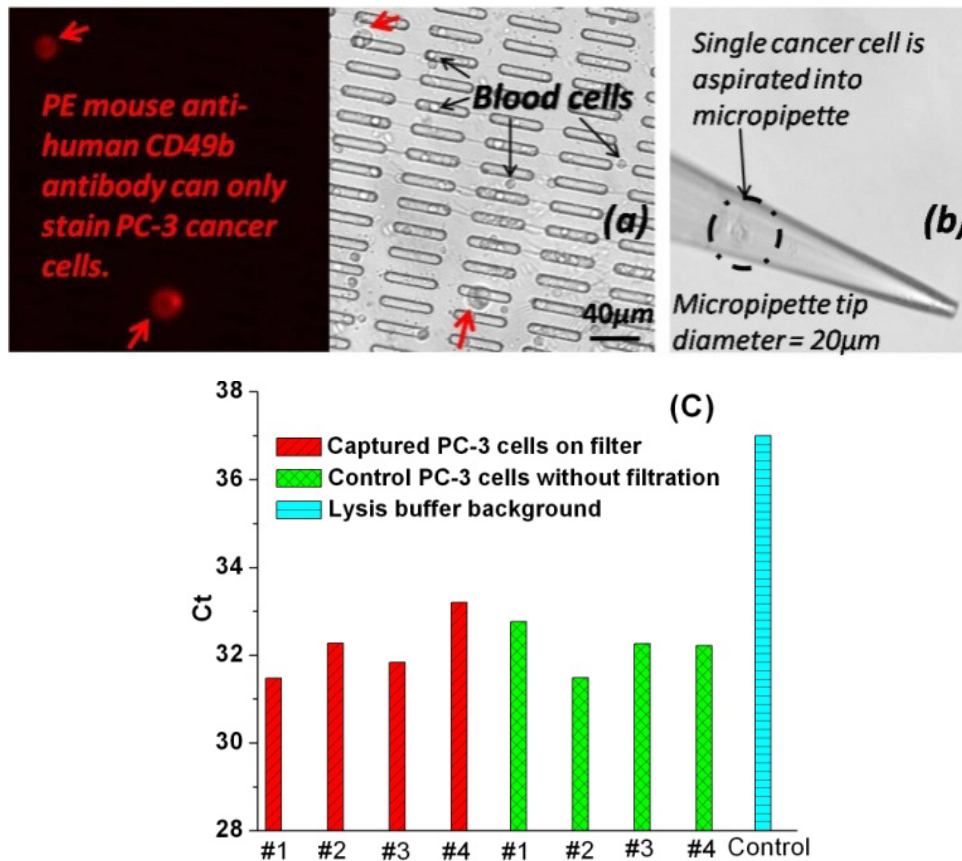


Figure 3-22: Single-cell telomerase measurement. (a) use of on-filter immunostaining to find the locations of cancer cells (red arrows: cancer cells; black arrows: blood cells); (b) single cancer cell was picked up by micropipette aspiration; (c) single cancer cell telomerase activity measured by qPCR

3.5 Discussion: Further Optimizations

Although successful clinical trials have been done with both 2D-pore-filter-based immunofluorescence assay, and 2D-slot-filter-based TRAP assay, efforts and strategies are still needed to further improve the enrichment, the detection sensitivity, the CTC viability, and the throughput.

3.5.1 Enrichment improvement

A straightforward method to improve the enrichment is to increase the open factor. By reducing the spacing between two slots and hexagonally arranging the locations of slots, a much larger open-factor can be achieved, which is favorable for high enrichment and throughput. However, if the open-factor is too large, the overall mechanical strength of the filter will be decreased. Table 3-3 compares the performances of two slot filters with 18% and 42% open factors. The enrichment was improved by one order when the open factor increases to 42%.

Table 3-3: Comparison of 2D slot filters with different open factors

Slot width	6 μm	6 μm
Open factor	18%	42%
Capture Efficiency	92.1 \pm 11.4%	92.4 \pm 7.4%
Viability	92.7 \pm 10.1%	93.8 \pm 3.4%
Enrichment	~ 200-fold	~ 2149-fold

Another possible approach is the immunoaffinity-enhanced capture. EpCAM can be first conjugated to the filter surface. After filtration, captured cells will be incubated

on-filter to allow the binding of EpCAM to cancer cells. Then the majority of blood cells can be removed by multiple rinses without the loss of target cancer cells. The increase in enrichment is at the cost of longer processing time and very expensive antibodies.

3.5.2 Sensitivity improvement

The term “sensitivity” here denotes the capability of the assay to detect the fluorescence signals or telomerase activity from CTCs. Sensitivity is closely related to the enrichment level. For immunofluorescence enumeration, reduction of blood cells will reduce the risk of false-positive staining. For telomerase activity detection, reduction of blood cells is important in keeping the background telomerase activity noise low.

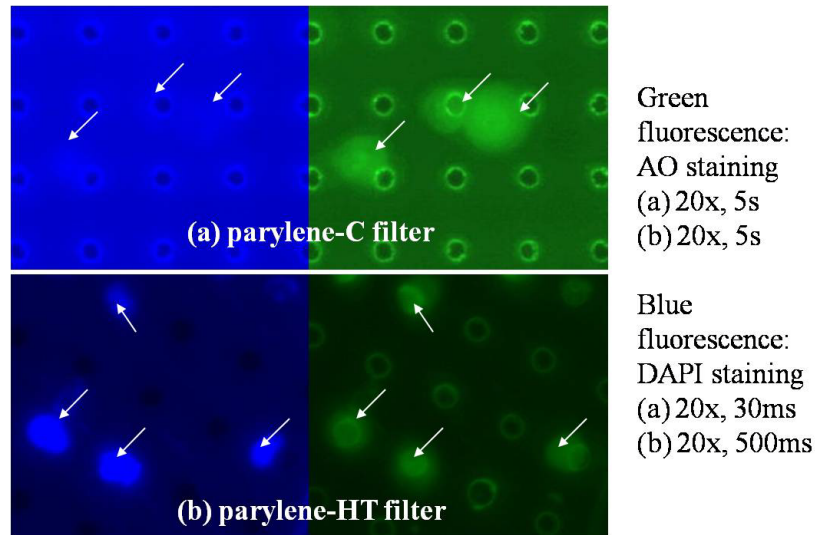


Figure 3-23: CTC filtration and enumeration experiments with parylene-C and parylene-HT membrane filters. Captured cancer cells were doubly stained with DAPI and AO. Parylene-C device had strong autofluorescence intensity, even with a much shorter exposure time. Parylene-HT device showed low autofluorescence, which ensured the successful detection of DAPI-stained cells. Green fluorescence with AO staining was only used as a reference to show captured cell locations.

Another kind of noise is introduced by the filter itself. In immunofluorescence detection, the background fluorescence can be a major reason for poor sensitivity. In Fig. 3-19, the contrast between the blue fluorescence from a DAPI-stained cell nucleus and the blue autofluorescence from the filter is not good enough. From the discussion in Section 2.4, the autofluorescence can be reduced by wisely choosing the fabrication techniques to avoid the UV or thermal processes. For example, a thermal evaporator, rather than an e-beam evaporator, should be used for the deposition of metal mask. Moreover, since parylene-HT shows much better autofluorescence performance, it can be an alternative filter material for parylene-C. Fig. 3-23 compares the performances of the parylene-C filter and parylene-HT filter. The parylene-HT filter shows much lower autofluorescence (especially for blue autofluorescence) and the captured cells can be clearly enumerated.

3.5.3 Viability improvement

Although in Table 3-3, the viability seems to be independent of the open factor, it still benefits from a large open factor. If a certain throughput (i.e., processing time) is required, a larger open factor means a smaller drive pressure is needed to process the sample. The smaller drive pressure induces less tension in the cell membrane, which in turn means a higher viability. From another angle, using the same drive pressure, the filtration time can be shortened for filters with larger open factors. In Section 3.7, the time-dependent cell membrane damage will be modeled and discussed in detail. Low drive pressure and short filtration time are two critical factors influencing viability.

3.5.4 Throughput improvement

Membrane filtration possesses the major advantage of its unbeatable high throughput in sample processing. Further improvement of throughput can result from the optimization of the filter, or of the filtration strategy. The open-factor is closely related to throughput if the drive pressure is fixed. Without changing the open factor, the throughput can be increased by processing samples through multiple filters in parallel. As long as a new filtration jig is designed with multiple chambers and nearly uniform sample delivery capability, this parallel filtration strategy can be powerful in further increasing the throughput.

3.6 CTC Culture After Capture

Due to the rarity of CTCs, the amount of CTCs captured from a patient sample may not be sufficient for further genomic or other analysis. The culture of captured CTCs is highly desirable for further studies of the cancer cells, since it can significantly increase the amount of CTCs. However, most previously published methods had problems with low viability, lack of biocompatible environment, or inability to release captured cells. Here, the slot filter has been demonstrated to have overcome these problems, for both on-filter and off-filter culture. For on-filter culture, even without any surface pre-treatment, PC-3 cells were able to adhere and proliferate on the filter surface (Fig. 3-24(a)). For off-filter culture, trapped cells were first released and collected from the filter, by multiple rinses or reverse flow (passing PBS from the back side), and then cultured in a petri-dish (Fig. 3-24(b)).

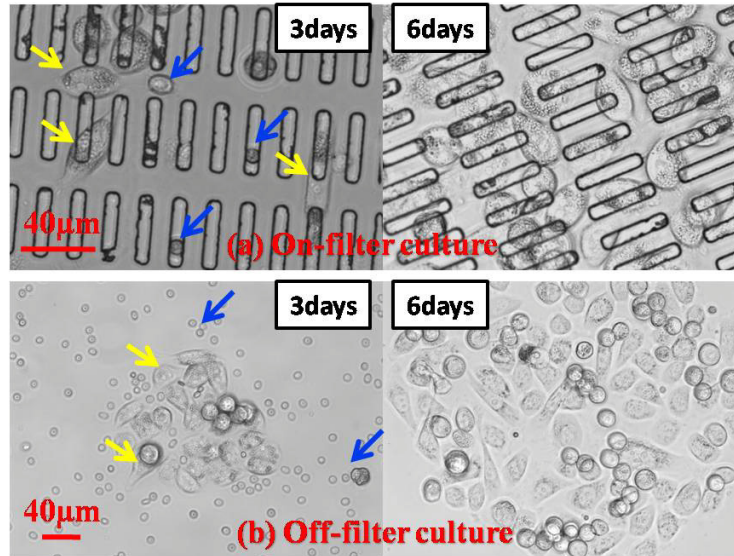


Figure 3-24: On-filter (a) and off-filter (b) cell culture of captured PC-3 cells from human blood after 3 days and 6 days in RPMI complete medium. Yellow arrows show examples of cancer cells spreading and dividing, and blue arrows show examples of remaining blood cells after filtration.

In Fig. 3-24, the cells are growing in a monolayer, which is often denoted as 2D culture. Recently, however, researchers are recognizing the limitations of 2D culture, given that it cannot fully reproduce the *in vivo* cellular microenvironment with cell-cell and cell-matrix interactions [21,22]. To better recapitulate the morphology and features the *in vivo* cells have, 3D culture models, which provide more *in vivo*-like conditions and realize the original growth characteristics of the tumors, are attracting increasingly more attention [21,22].

For on-chip 3D cell culture, cell-cell and cell-extracellular matrix (ECM) interactions should dominate over cell-substrate interaction. Therefore, we need to treat the filter surface to be resistant to cancer cell adhesion. Surface property and cancer cell adhesion evaluations of untreated parylene-C, O₂ plasma treated parylene-C, parylene-C with parylene-HT coating, and polystyrene are shown in Fig. 3-25(a)-(b). Untreated

parylene-C surface was hydrophobic. While plasma treatment could cause it to become hydrophilic, parylene-HT coating rendered the surface even more hydrophobic. After 10 hours of incubation, about 30% PC-3 cancer cells remained adhered to the untreated parylene-C surface. Although the untreated parylene-C surface could be considered as cell resistant compared to the tissue culture polystyrene control, it was still not suitable for 3D tumor culture. Fig. 3-25(c) shows that during 3D tumor culture some cancer cells adhered and proliferated two-dimensionally on the untreated parylene-C filter, which was undesirable. It was noticed that a plasma-treated parylene-C surface displayed enhanced adhesion. In comparison, a parylene-HT-coated surface heavily repelled cancer cell adhesion, reducing the cell adhesiveness to only one-third of the original level.

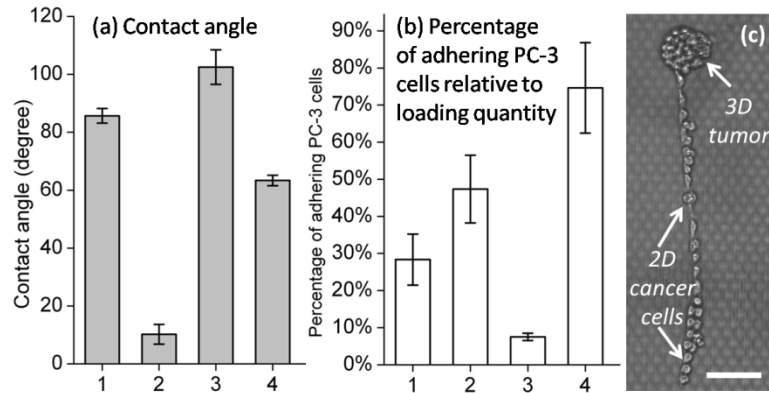


Figure 3-25: Parylene surface treatments and their influences on cell adherence. 1: untreated parylene-C surface; 2: O₂ plasma treated parylene-C; 3: parylene-C with parylene-HT coating; 4: tissue culture polystyrene substrate. (a) contact angle measurement; (b) evaluation of cancer cell adhesiveness; (c) without parylene-HT coating, some cancer cells adhered and proliferated on untreated parylene-C filter surface during 3D tumor culture with Matrigel. (scale bar: 100 μm)

Therefore, a parylene-HT-coated parylene-C filter was selected for 3D culture

after filtration. The fabrication process flow of this special filter is shown in Fig. 3-26. To demonstrate the feasibility of on-filter 3D culture of the captured cancer cells after filtration, we spiked about 30 unlabeled PC-3 cancer cells into 1 mL PBS. The sample was filtrated and cancer cells were captured on the filter. Matrigel was selected as the 3D scaffold material. A 1:1 mixture of Matrigel (BD Biosciences) and RPMI complete medium was carefully injected into the filter top chamber by a syringe pump, to prevent cell damage and undesirable bubble appearance. Gelation was allowed to occur at 37°C for 30 min. Then the filter assembly was inverted and covered with RPMI complete medium. The whole setup was left in a petri-dish and placed in an incubator. Culture medium was refreshed every day. Calcein-AM and PI live/dead cell staining was used again to determine the cellular viability of the 3D tumor. The operation procedure of the 3D culture is shown in Fig. 3-27.

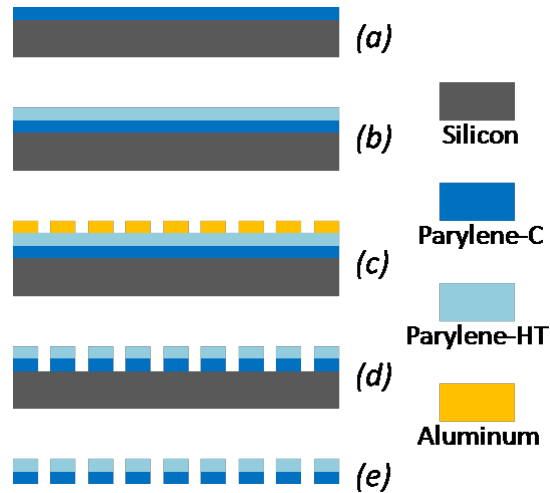


Figure 3-26: Parylene-C/HT filter fabrication process. (a) 9 μm parylene-C deposition; (b) 0.5 μm parylene-HT deposition; (c) aluminum deposition and wet-etching patterning; (d) pattern parylene layers by RIE; (e) release parylene filter from Si substrate

2D monolayer cancer cell culture without Matrigel injection was used as a control. For 2D on-filter culture, the membrane filter was disassembled after filtration and soaked in the culture medium.

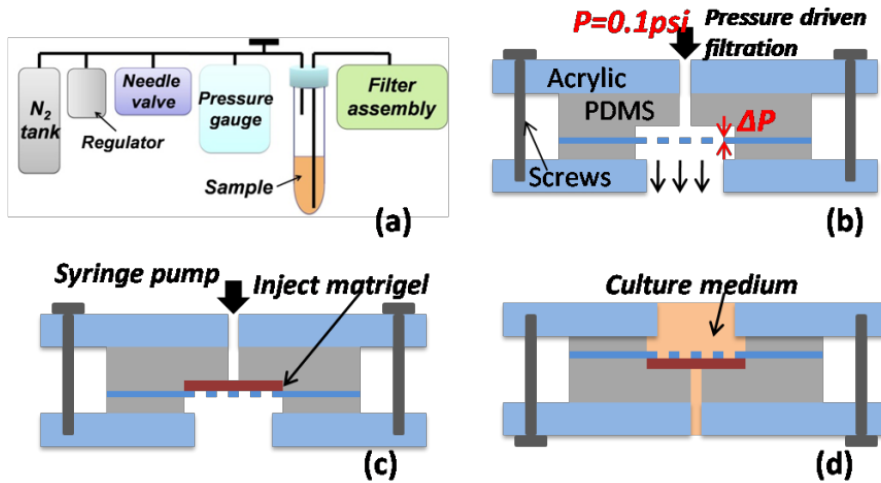


Figure 3-27: Operation procedure of 3D on-filter culture. (a) schematic of the low-constant-pressure filtration system; (b) filter assembly and filtration process; (c) Matrigel injection after filtration; (d) schematic of 3D on-filter tumor culture

Captured PC-3 cancer cells proliferated three-dimensionally into the Matrigel, and gradually formed a spherical tumor. Matrigel is a biomatrix hydrogel containing many essential components of the ECM, such as collagen, laminin, entactin, and other important growth factors which can support cellular proliferation and induce cellular differentiation [21,22]. The cellular proliferation rate was monitored in Fig. 3-28(a). On the 6th day, live/dead staining was used to evaluate the cellular viability inside the tumor (Fig. 3-28(b)–(e)). Over 90% cells stayed viable during the tumor formation.

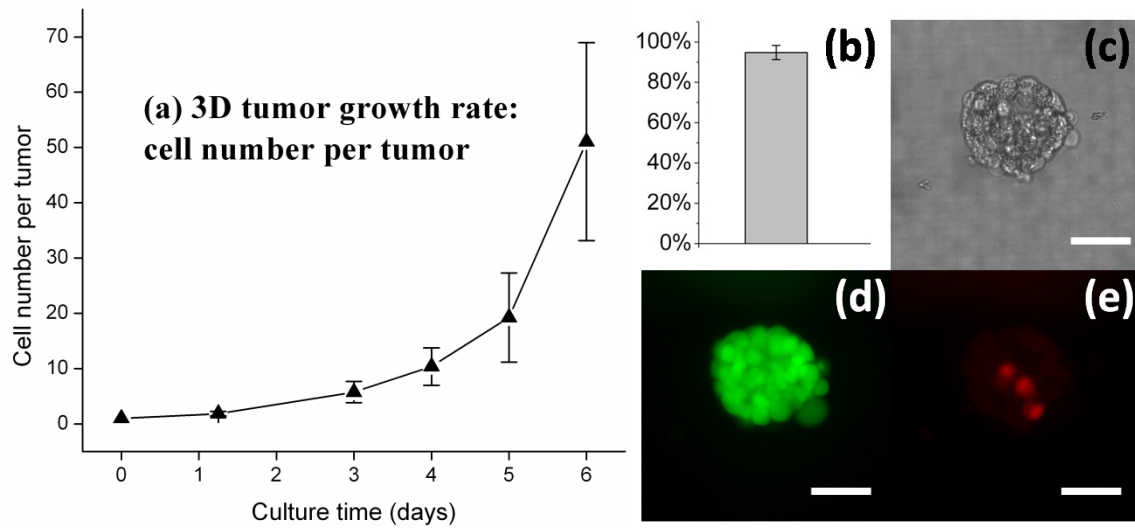


Figure 3-28: 3D on-filter cultured tumor growth rate and viability. (a) growth rate; (b) viability on the 6th day; (c)–(e) bright field and fluorescence images of calcein-AM & PI stained tumor. (all scale bars: 40 μm)

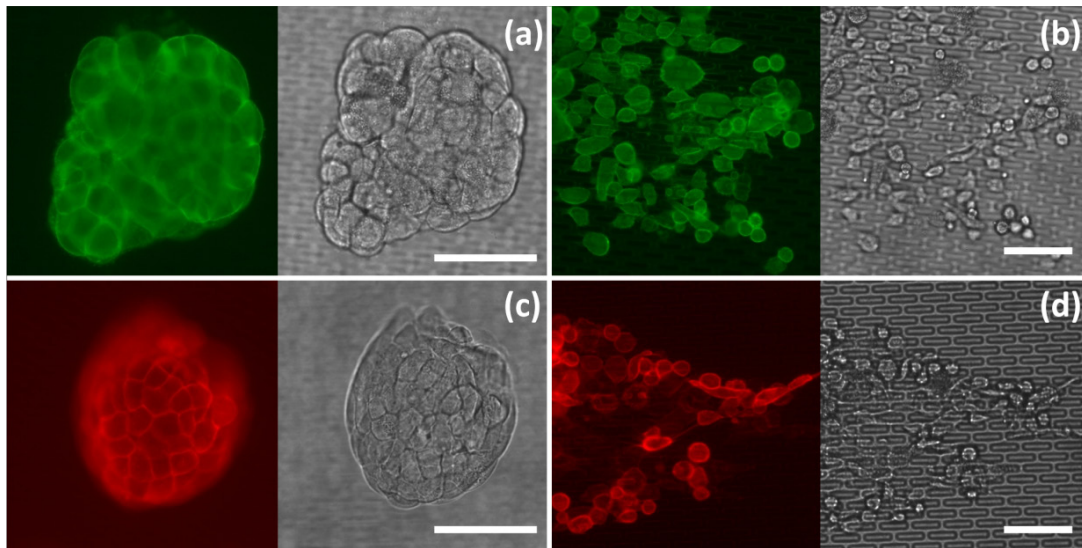


Figure 3-29: Immuno-staining of cultured 3D tumor. (a) 3D tumor stained with FITC-conjugated anti-EpCAM antibody. (c) 3D tumor stained with PE-conjugated anti-human CD49b antibody. The 2D on-filter (without parylene-HT coating) culture controls are shown in (b) and (d), respectively. (all scale bars: 100 μm)

To further investigate the structure of the tumor, after 8 days of culture we stained the cell membranes with cancer-specific immunofluorescence surface markers (Fig. 3-29). The images indicated that separate cells were adhering to form a combined structure. Cell-cell and cell-ECM interactions were clearly observed. In comparison, 2D on-filter culture was used as a control (Fig. 3-29). Cells attached to the parylene-C filter, and formed a confluent 2D monolayer after 8 days of culture.

3.7 A Biomechanical Study of Cell Membrane Damage

3.7.1 Motivation

In the previous sections, although we have successfully demonstrated the high-viability capture by 2D slot filter, we still observed that the viability could become much lower, either when high drive pressure was applied, or when long-time filtration was carried out under low drive pressure for samples with large volumes. Therefore, a study on the mechanism of CTC damage during filtration may help to further improve viability.

Previous studies have shown that cell damage is closely related to its membrane integrity [23–29]. The cell membrane consists of a lipid bilayer, which could be ruptured by membrane tension. Micropipette aspiration and osmotic expansion are two widely used methods to study cell membrane damage under tension [23–27]. However, these approaches usually require special setups with high-resolution imaging systems. In this work, we use the simpler filtration-based approach to evaluate the cell membrane damage under mechanical tension by using the parylene-C membrane slot filter for viable CTC capture. Unlike other methods focusing on a single cell, we study the cell damage by adopting a statistical approach to analyze the viability of cancer cells after filtration.

When processing samples with different volumes, a clear time-dependent viability drop has been observed, which could be reasonably explained by our cell membrane failure models. These models also agree well with previous studies on the red blood cell membrane using micropipette aspiration [25] and osmotic expansion [27]. More importantly, for the first time, we predicted a “golden zone” for viable CTC capture. Specifying drive pressure and filtration time, this can be used as guidance for future membrane filter design and operation.

3.7.2 Experiment approach

PC-3 prostate cancer cells were studied here because of their similarity in properties to those of CTCs. PC-3 cells (average diameter of 17 μm) were cultured in RPMI complete culture medium (Mediatech, Inc.) in an environment with 37 °C and 5% CO_2 . A model system was built by spiking a known number of PC-3 cells into 1:4 diluted human whole blood samples to mimic CTCs inside patient blood. Different sample volumes ranged from 1 mL to 5 mL. Before spiking, we pre-stained PC-3 cells with Calcein-AM (Invitrogen) for viability evaluation after filtration.

By adjusting the regulator and needle valve, we set the drive pressure to be 0.10, 0.13, 0.15, 0.17, and 0.20 psi, respectively. At each drive pressure, samples with volumes of 1–5 mL were filtrated, and each run was repeated three times. The filtration time was recorded accordingly. After each filtration, the filter was disassembled from the jig and stained with PI (Invitrogen). Live and dead cancer cells were observed under a fluorescence microscope. Live cells with intact membrane could retain Calcein-AM and exclude PI, while dead cells lost Calcein-AM and the compromised membrane became

permeable to PI. The viability was defined in Eq. 3-4. Please note that the definition of viability here is different from the previous one in Eq. 3-3.

$$Viability = \frac{\# \text{ of viable cancer cells on filter after filtration}}{\# \text{ of cancer cells spiked in the sample before filtration}} \quad (3-4)$$

3.7.3 Cell modeling

A cortical shell-liquid core model is introduced to represent a captured cancer cell, which simplifies the cell membrane as a thin shell, and the intracellular content as a homogeneous liquid. According to the SEM image in Fig. 3-18(c), when a cell is captured on a slot, under low drive pressure, the exterior portion can be approximated to be near-spherical. However, the small portion trapped inside the slot may deform two dimensionally. A half-ellipsoid with three principle axes of L , W , and W , is assumed, where W is the slot width (Fig. 3-30).

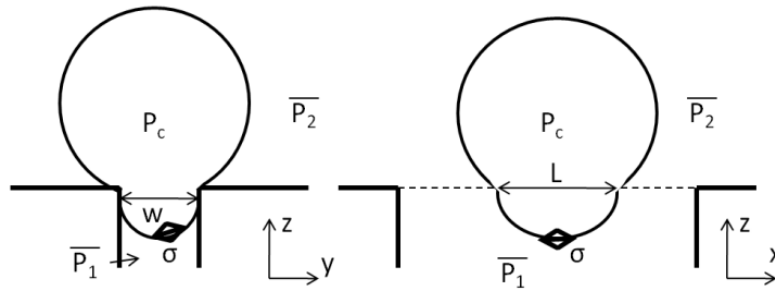


Figure 3-30: Cortical-shell/liquid-core model of a cell captured on a slot. The initial cell radius is R_0 . W is the slot width.

Previous reports have shown that the internal pressure of cells suspended in isotonic solution is only ~ 24.5 Pa higher than the external surrounding pressure [30,31].

However, when a much higher external pressure is applied, this low initial pressure will increase in response to the external pressure [30]. During filtration, since the drive pressures (0.10–0.20 psi) are much larger than the initial intracellular pressure, the intracellular pressure P_c will increase correspondingly and can be approximated by the average exterior pressure \bar{P}_2 , under the assumption that the cell volume is constant and only a small portion is deformed into the slot [30,32,33].

According to Laplace's equation, the transfilter pressure drop is:

$$\Delta P = \bar{P}_2 - \bar{P}_1 = P_c - \bar{P}_1 = \sigma(1/R_x + 1/R_y),$$

where R_x and R_y are the principle radii of curvature at a point on the ellipsoid surface, and σ is the membrane tension. Since both the minimum curvature and the largest pressure difference appear on the bottom, the maximum tension is also expected there. Assume the deformed part has a length of L in the x direction. Then L_{min} should be equal to the slot width, while L_{max} can be approximated to the cell's diameter ($2R_0$). The radii of curvature are,

$$R_x = (L/2)^2/(W/2), \text{ and } R_y = W/2.$$

Hence,

$$\Delta P = \sigma(2W/L^2 + 2/W).$$

Since $W < L < 2R_0$,

$$W\Delta P/4 < \sigma < \Delta P/[2(W/4R_0^2 + 1/W)]. \quad (3-5)$$

3.7.4 Simulation

In order to correlate the transfilter pressure drop ΔP to the drive pressure P , a 3D fluid model of slot filter filtration was built with finite-element (FEM) simulation tool

COMSOL Multiphysics (Fig. 3-31(a)). The pressure distribution was extracted from the post-processing (Fig. 3-31(b)) by a custom-coded MATLAB program. The calculated transfilter pressure drop is

$$\Delta P \approx 0.58P. \quad (3-6)$$

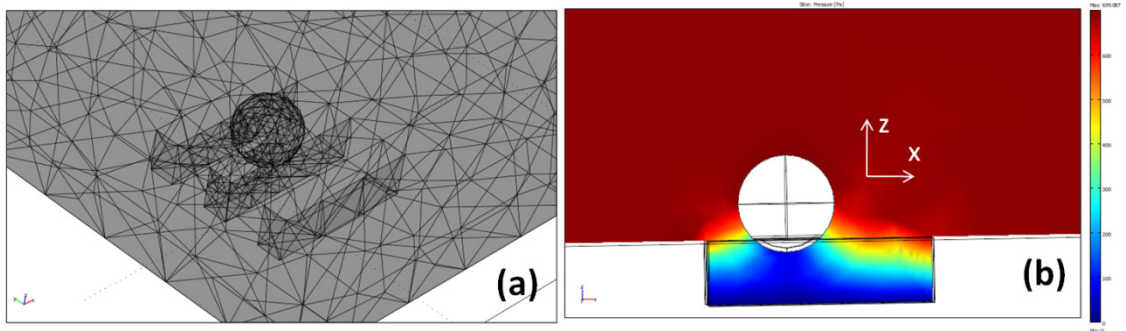


Figure 3-31: COMSOL simulation results. (a) the mesh of a 3D fluid model of a cell captured on a slot. (b) the pressure distribution around the captured cell.

3.7.5 Time-dependent viability drop

Different filtration time was achieved by filtrating samples with different volumes. The filtration time (t) was recorded for each run of samples with different volumes and drive pressure. Fig. 3-32 clearly shows a time-dependent viability drop under different drive pressures (0.10–0.20 psi), although the membrane tension was kept nearly constant during each filtration. Assuming the probability of cell lysis follows the exponential distribution [27], and that the mean time of cell lysis upon capture is τ , then the cumulative distribution function of a cell which is already dead after it has been captured for a time period of t is:

$$F(t) = 1 - \exp(-t/\tau).$$

Correspondingly, the probability of a cell still being alive after having been captured for

time t is:

$$P_{viable}(t) = 1 - F(t) = \exp(-t/\tau).$$

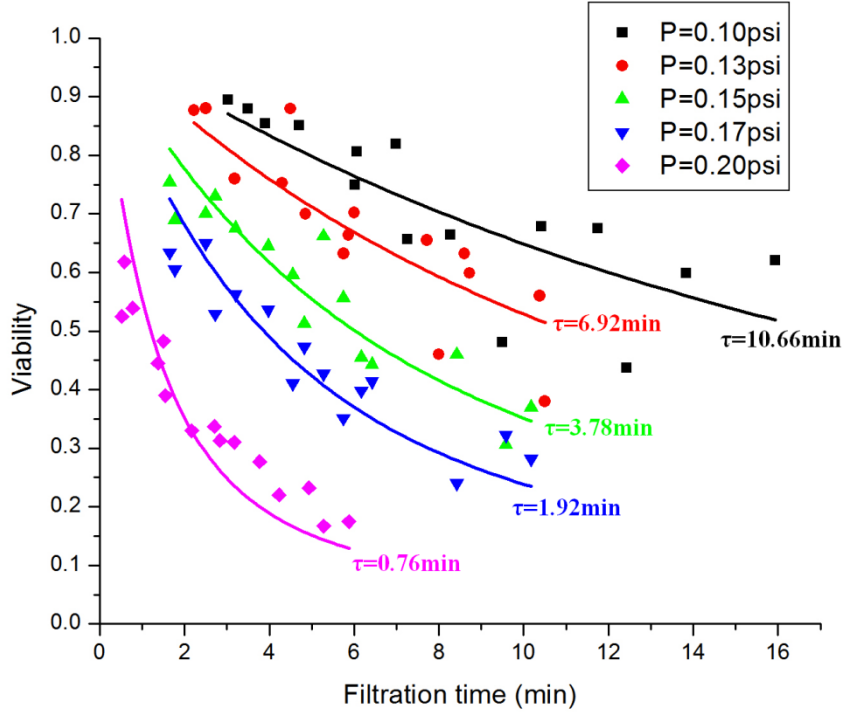


Figure 3-32: Time-dependent viability drop at different drive pressures. The mean lysis time τ was obtained by fitting data into Eq. 3-7.

Assume that at time t , the total number of captured cancer cells is N , and the spiked cancer cells are uniformly distributed in the sample. Then the time interval between two capture events is $\Delta t = t/N$. At time t , the expectation of the viability of captured cells is

$$V(t) = (1/N) \sum_{n=1}^N \exp[-(nt)/(\tau N)] = (\Delta t/t) \sum_{n=1}^N \exp[-(n\Delta t)/\tau].$$

Hence,

$$V(t) = (\pi/t)[1 - \exp(-t/\pi)]. \quad (3-7)$$

Values of τ under different drive pressures were obtained by fitting the experimental data (Fig. 3-32) into Eq. 3-7.

3.7.6 Molecular membrane failure model

In the previous literature studying the lysis of red blood cells during micropipette aspiration or membrane filtration, time-related cell lysis was observed and this phenomenon was explained by the viscoelasticity of the cell membrane under constant tension [25]. It was found that the cell membrane will rupture if the strain on the cell membrane exceeds the critical strain for lysis. The strain in the membrane, at a given tension, is a function of time, which behaves like a viscoelastic material [25]. However, the viscoelastic model itself may not be able to fully depict the underlying physical mechanism of the time-dependent viability drop, since no molecular structures are represented by the springs and dashpots. For instance, in the latter stage of the viscoelastic model, the strain increases linearly with time [25]. However, for traditional viscoelastic materials, the strain rate usually decreases with time. This discrepancy between cell membrane and other viscoelastic materials may be a result of its special structure.

From the molecular view, it is believed that under mechanical stress or tension, metastable nanosized pores appear in the lipid membrane, and the expansion of the pores beyond a critical radius leads to irreversible membrane breakdown (Fig. 3-33) [27–29]. The membrane's resistance to rupture is represented in terms of a line tension γ . The free energy E of the formation of a pore with radius R is:

$$E(R, \sigma) = 2\pi R\gamma - \pi R^2\sigma$$

where the first term on the right is the edge energy of the pore and the second term represents the work done by the tension σ . $E(R)$ reaches its maximum, $E(R^*) = E^* = \pi\gamma^2/\sigma$, when $R = R^* = \gamma/\sigma$. Therefore, if $R < R^*$, the pores tend to reseal, while when $R > R^*$, the pore tends to grow rapidly and lead to membrane breakdown. In our work, we take into consideration one more energy term (C) corresponding to the energy of exposing intracellular materials outside the membrane when nanopores exist and the loss of intracellular materials starts (Fig. 3-33). Therefore, the modified energy balance is:

$$E(R, \sigma) = 2\pi R\gamma - \pi R^2(\sigma + C).$$

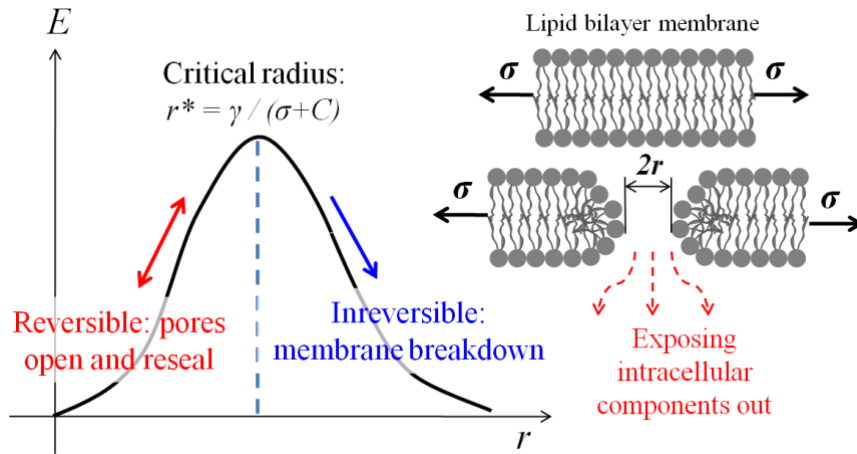


Figure 3-33: Schematic of nanopore formation in lipid bilayer membrane

Assuming the energy of pores has a Boltzmann distribution, and the probability of the rupture of cells follows the exponential distribution, there is a relation between the time constant τ of cell lysis and the membrane tension σ [27],

$$\text{Log}\tau = A + E^*(\sigma)/(k_B T) = A + (\pi\gamma^2)/[k_B T(\sigma + C)] \quad (3-8)$$

where k_B is the Boltzmann constant, T is the absolute temperature, and A is a constant.

Fig. 3-34(a) shows the fitting of time constants with tensions using Eq. 3-8. The line tension is $\gamma = 0.75 \times 10^{-11} N$, which is very close to the reported value $1 \times 10^{-11} N$ for a lipid bilayer [27–29]. The energy term for exposing intracellular material is determined to be $C = 0.00243 N/m$.

3.7.7 Griffith's membrane failure model

From another point of view, the appearance of nanosized pores and the rupture of cell membrane under tension can also be explained by the Griffith's failure theory. Although Griffith's failure theory is mainly used to study the failure of brittle materials from an atomic view in fracture mechanics [34], it also applies to cell membranes since the membrane can be considered to be composed of lipid molecules. Potential energy exists as a function of lipid molecular separation. At the equilibrium distance, the potential energy has the minimum value, and the attractive and repelling forces are balanced [34]. According to Griffith's theory, a pore can form (or an existing pore can grow) only if this process decreases or maintains the total energy,

$$dE_{total}/dr = (dU/dr) + (dW/dr) = 0 \quad (3-9)$$

where r is the pore radius, U is the work done by the tension, and W is the edge energy. Assuming E is the Young's modulus, γ is the line tension, b is the membrane thickness, and C is the energy term from exposing intracellular material outside, then the work done by the tension is

$$U = -(\pi F^2 r^2 b)/E - C\pi r^2$$

$$dU/dr = -2\pi r[(F^2 b)/E + C] = -2\pi r[\sigma^2/(Eb) + C].$$

Here F is the stress, and $F = \sigma/b$, where σ is the membrane tension. On the other hand, the edge energy is,

$$W = 2\pi r\gamma$$

$$dW/dr = 2\pi\gamma.$$

According to Eq. 3-8,

$$dU/dr = -dW/dr, \text{ and } r^* = \gamma/[\sigma^2/(Eb) + C]$$

when $r = r^*$,

$$E_{total} = 2\pi\gamma r^* - [\sigma^2/(Eb) + C]\pi r^{*2} = (\pi\gamma^2)/[\sigma^2/(Eb) + C]$$

Like in the molecular membrane failure model, a relation between the mean failure time and tension can be found as,

$$\text{Log}\tau = A + (\pi\gamma^2)/\{[\sigma^2/(Eb) + C]k_B T\} \quad (3-10)$$

where A is a constant.

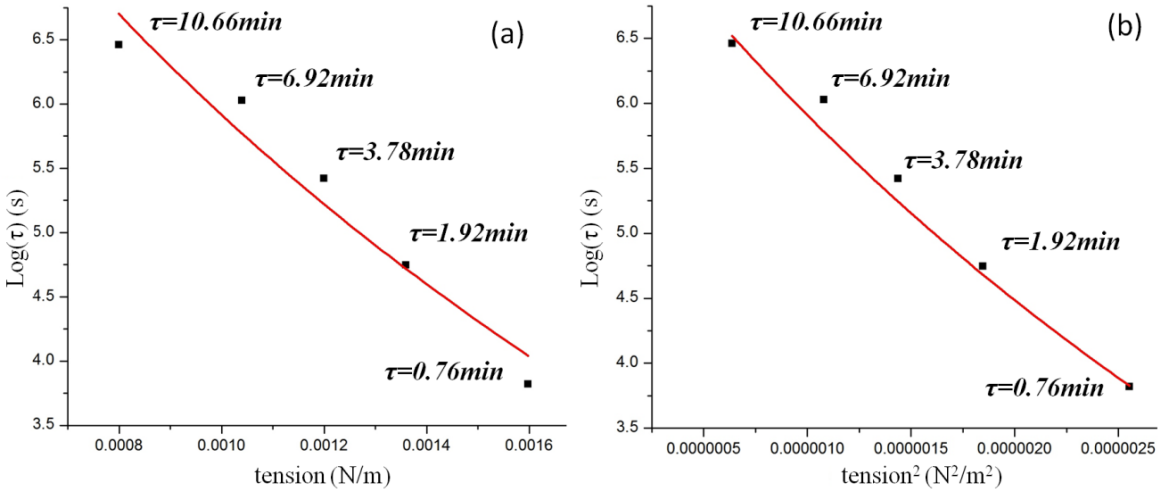


Figure 3-34: Relations between the mean cell lysis time τ and the membrane tension σ for (a) the molecular membrane failure model and (b) the Griffith's membrane failure model. Tensions were calculated by Eqs. 3-5 and 3-6, taking the median value.

From the literature, we choose the Young's modulus to be 1×10^6 Pa, and the thickness to be 4 nm [25,35]. By fitting the experimental data of the relation between $\text{Log}(\tau)$ and σ^2 into Eq. 3-10 (Fig. 3-34(b)), the line tension is found to be $\gamma = 0.57 \times 10^{-11}$ N, and the energy term of exposing intracellular material is $C = 0.00172$ N/m.

It is worth mentioning that many reports have shown that nucleated cells are able to repair their plasma membranes to reseal membrane wounding and protect themselves from rupture [36]. However, if a membrane tension is artificially imposed, the resealing can be slowed down [36,37]. At high tensions, this resealing can even be completely blocked. In this work we do not take into consideration membrane repairmen, which may be considered reasonable because the artificial tension is exerted by capture and pressure drop, which is much higher than the original tension when cells are suspended in isotopic solutions.

3.7.8 Comparison of models

The models we proposed above, which explain the mechanism of time-dependent cell membrane damage by tension, are considered to be universal and also applicable to the membrane-rupture experiments reported before. Although direct comparison with other studies on cancer cell membrane rupture is unavailable, we used our models to fit the experimental data of time-dependent red blood cell (RBC) lysis by both micropipette aspiration and osmotic pressure expansion approaches [25,27]. Table 3-4 summarizes all the fitting parameters. Although the methods are totally different, the fitted line tensions are comparable. The discrepancies between the energy terms C may be due to different

types of cells. For instance, cancer cells are able to repair their membrane by resealing, protecting themselves from rupture, while this repair mechanism may be totally different for RBCs.

Table 3-4: Fitting parameters of experimental data in our work on cancer cells by filtration, Rand's work on RBCs by micropipette aspiration [25], and Taupin's work on RBCs by osmotic expansion [27]

	Molecular membrane failure model			Griffith's membrane failure model		
	γ 10^{-11}N	C mN/m	R^2	γ 10^{-11}N	C mN/m	R^2
Our data	0.75	2.43	0.95	0.57	1.72	0.98
Rand's	1.16	2.06	0.99	2.00	23.37	0.99
Taupin's	1.41	2.37	0.98	1.36	31.00	0.87

* R^2 is the evaluation of curve fitting.

3.7.9 Prediction of the safe “golden zone”

From both models discussed above, we are able to predict a “golden zone” regarding the drive pressure and filtration time. According to Eqs. 3-5 to 3-8 and Eq. 3-10, we can correlate the viability with drive pressure and filtration time. Therefore, for a given viability, the drive pressure and filtration time place restrictions on each other. Fig. 3-35 shows that both models predict similar safe zones. Operation below a contour with viability of V can achieve a viability higher than V . These viability contours plots can help determine the proper drive pressure and the maximum sample volume for viable CTC capture. For instance, for a certain drive pressure, in order to keep a high viability, the total filtration time has its limitation. To process samples with large volume (e.g., 5–

10 mL in clinical trial), increasing the membrane filter area or using multiple filters for parallel sample processing could reduce the filtration time, allowing it to operate in the safe “golden zone”. Moreover, these models are also useful in estimating cell damage in live cell manipulation or other biomechanical applications when the membrane tension and its duration are known.

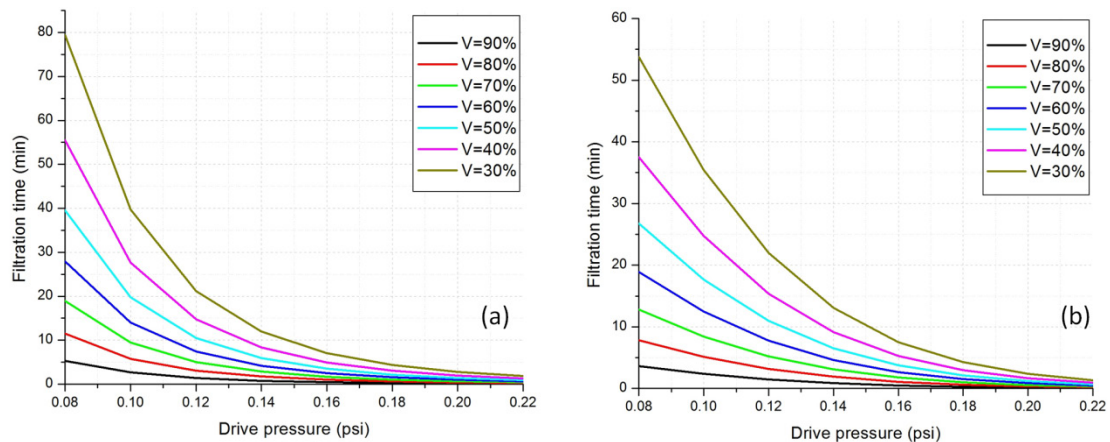


Figure 3-35: The safe “golden zones” predicted by (a) the molecular membrane failure model and (b) the Griffith’s membrane failure model.

3.8 Summary

This chapter introduces the polyethylene membrane filter based filtration system and assays for the detection of CTCs and early diagnosis of cancer. The membrane filter designs went through four generations, and finally a single-layer slot filter was able to capture viable CTCs with high capture efficiency, high viability, moderate enrichment, and high throughput. The feasibility has been demonstrated by extensive experiments. More importantly, the CTC detection methods described in this chapter have already been successfully verified in clinical trials, and the 2D pore filter has already been

commercialized. Besides CTC capture and detection, further CTC culturing is also discussed, which will be very useful for future genomic studies and anti-cancer drug screening. In the end, a deep biomechanical model of cell membrane damage under mechanical tension is presented. This model can provide guidance for future filter design and help to achieve high-viability CTC capture.

3.9 References

- [1] P. Boyle and B. Levin, *World cancer report*, World Health Organization, Geneva, 2008
- [2] S. Zheng, H.K. Lin, B. Lu, A. Williams, R. Datar, R.J. Cote and Y.C. Tai, 3D microfilter device for viable circulating tumor cell (CTC) enrichment from blood, *Biomedical Microdevices*, vol. 13, pp. 203–213, 2011
- [3] M. Cristofanilli, G.T. Budd et al., Circulating tumor cells, disease progression, and survival in metastatic breast cancer, *New England Journal of Medicine*, vol. 351, pp. 781–791, 2004
- [4] M. Cristofallini, D.F. Hayes et al., Circulating tumor cells: a novel prognostic factor for newly diagnosed metastatic breast cancer, *Journal of Clinical Oncology*, vol. 23, pp. 1420–1430, 2005
- [5] G.T. Budd, M. Cristofallini et al., Circulating tumor cells versus imaging – predicting overall survival in metastatic breast cancer, *Clinical Cancer Research*, vol. 12, pp. 6403–6409, 2006
- [6] M. Cristofanilli and J. Mendelsohn, Circulating tumor cells in breast cancer: advanced tools for “tailored” therapy? *Proceedings of the National Academy of Sciences*, vol. 103, pp. 17073–17074, 2006
- [7] S. Zheng, H.K. Lin, J.Q. Liu, M. Balic, R. Datar, R.J. Cote and Y.C. Tai, Membrane microfilter device for selective capture, electrolysis and genomic analysis of human circulating tumor cells, *Journal of Chromatography A*, vol. 1162, pp. 154–161, 2007

- [8] P. Paterlini-Brechot and N.L. Benali, Circulating tumor cells (CTC) detection: Clinical impact and future directions, *Cancer Letters*, vol. 253, pp. 180–204, 2007
- [9] O. Lara, X. Tong, M. Zborowski and J.J. Chalmers, Enrichment of rare cancer cells through depletion of normal cells using density and flow-through, immunomagnetic cell separation, *Experimental Hematology*, vol. 32, pp. 891–904, 2004
- [10] S. Nagrath, L.V. Sequist, S. Maheswaran et al., Isolation of rare circulating tumor cells in cancer patients by microchip technology, *Nature*, vol. 450, pp. 1235–1239, 2007
- [11] S. Maheswaran, L.V. Sequist et al., Detection of mutations in EGFR in circulating lung-cancer cells, *New England Journal of Medicine*, vol. 359, pp. 366–377, 2008
- [12] H.J. Kahn, A. Presta et al., Enumeration of circulating tumor cells in the blood of breast cancer patients after filtration enrichment: correlation with disease stage, *Breast Cancer Research and Treatment*, vol. 86, pp. 237–247, 2004
- [13] L. Zabaglo, M.G. Ormerod, M. Parton, A. Ring, I.E. Smith and M. Dowsett, Cell filtration-laser scanning cytometry for the characterisation of circulating breast cancer cells, *Cytometry Part A*, vol. 55A, pp.102–108, 2003
- [14] S.J. Tan, L. Yobas, G.Y.H. Lee, C.N. Ong and C.T. Lim, Microdevices for the isolation and enumeration of cancer cells from blood, *Biomedical Microdevices*, vol. 11, pp. 883–892, 2009
- [15] T. Xu, B. Lu, Y.C. Tai and A. Goldkorn, A cancer detection platform which measures telomerase activity from live circulating tumor cells captured on a microfilter, *Cancer Research*, vol. 70, pp. 6420–6426, 2010
- [16] J.S. Kuo, Y. Zhao, P.G. Schiro, L. Ng, D.S.W. Lim, J.P. Shelby and D.T. Chiu, Deformability considerations in filtration of biological cells, *Lab on a Chip*, vol. 10, pp. 837–842, 2010
- [17] H.K. Lin, S. Zheng et al., Portable filter-based microdevice for detection and characterization of circulating tumor cells, *Clinical Cancer Research*, vol. 16, pp. 5011–5018, 2010

- [18] P.T.H. Went, A. Lugli, S. Meier, M. Bundi, M. Mirlacher, G. Sauter and S. Dirnhofer, Frequent EpCam protein expression in human carcinomas, *Human Pathology*, vol. 35, pp. 122–128, 2004
- [19] T. Xu, Y. Xu, C.P. Liao, R. Lau and A. Goldkorn, Reprogramming murine telomerase rapidly inhibits the growth of mouse cancer cells in vitro and in vivo, *Molecular Cancer Therapeutics*, vol. 9, pp. 438–449, 2010
- [20] J.W. Shaw and S. Bacchetti, A survey of telomerase activity in human cancer, *European Journal of Cancer*, vol. 33, pp. 787–791, 1997
- [21] Y. Torisawa, H. Shiku, T. Yasukawa et al. Multi-channel 3-D cell culture device integrated on a silicon chip for anticancer drug sensitivity test, *Biomaterials*, vol. 26, pp. 2165–2172, 2005
- [22] T. R. Sodunke, K. K. Turner, S. A. Caldwell et al. Micropatterns of Matrigel for three-dimensional epithelial cultures, *Biomaterials*, vol. 28, pp. 4006–4016, 2007
- [23] L. Weiss and G.W. Schmid-Schonbein, Biomechanical interactions of cancer-cells with the microvasculature during metastasis, *Cell Biophysics*, vol. 14, pp. 187–215, 1989
- [24] L. Weiss, U. Nannmark, B.R. Johansson and U. Bagge, Lethal deformation of cancer-cells in the microcirculation—A potential rate regulator of hematogenous metastasis, *International Journal of Cancer*, vol. 50, pp. 103–107, 1992
- [25] R.P. Rand, Mechanical properties of the red cell membrane: II. Viscoelastic breakdown of the membrane, *Biophysical Journal*, vol. 4, pp. 303–316, 1964
- [26] R. Kwok and E. Evans, Thermoelasticity of large lecithin bilayer vesicles, *Biophysical Journal*, vol. 35, pp. 637–652, 1981
- [27] C. Taupin, M. Dvolaitzky and C. Sauterey, Osmotic pressure induced pores in phospholipid vesicles, *Biochemistry*, vol. 14, pp. 4771–4775, 1975
- [28] H. Leontiadou, A.E. Mark and S.J. Marrink, Molecular dynamics simulations of hydrophilic pores in lipid bilayers, *Biophysical Journal*, vol. 86, pp. 2156–2164, 2004

- [29] M.D. Tomasini, C. Rinaldi and M.S. Tomassone, Molecular dynamics simulations of rupture in lipid bilayers, *Experimental Biology and Medicine*, vol. 235, pp. 181–188, 2010
- [30] S.M. Kelly and P.T. Macklem, Direct measurement of intracellular pressure, *American Journal of Physiology—Cell Physiology*, vol. 260, pp. C652–C657, 1991
- [31] R.P. Rand and A.C. Burton, Mechanical properties of the red cell membrane: I. Membrane stiffness and intracellular pressure, *Biophysical Journal*, vol. 4, pp. 115–135, 1964
- [32] A. L. Zydney and C. K. Colton, A red cell deformation model for hemolysis in cross flow membrane plasmapheresis, *Chemical Engineering Communications*, vol. 30, pp. 191–207, 1984
- [33] W.M. Saltzman, An investigation of the hydrodynamic resistance of concentrated layers of erythrocytes, M.S. Thesis, Massachusetts Institute of Technology, 1984
- [34] T.L. Anderson, Fracture mechanics: fundamentals and applications, 3rd edn., CRC Taylor & Francis Group, Boca Raton, FL, ch. 2, pp. 25–30, 2005
- [35] J. C. Weaver, Molecular-basis for cell-membrane electroporation, *Annals of the New York Academy of Sciences*, vol. 720, pp. 141–152, 1994
- [36] P.L. McNeil and R.A. Steinhardt, Plasma membrane disruption: repair, prevention, adaptation, *Annual Review of Cell and Developmental Biology*, vol. 19, pp. 697–731, 2003
- [37] D.V. Zhelev and D. Needham, Tension-stabilized pores in giant vesicles—determination of pore-size and pore line tension, *Biochimica et Biophysica Acta (BBA)—Biomembranes*, vol. 1147, pp. 89–104, 1993

CHAPTER 4

PARYLENE ARTIFICIAL BRUCH'S MEMBRANE

4.1 Overview

Age-related macular degeneration (AMD) is one of the leading causes of blindness in the elderly population [1–3]. AMD is usually characterized by the degeneration of Bruch's membrane and the dysfunction of retinal pigment epithelial (RPE) cells. Bruch's membrane is a thin (2–4 μm in thickness) [2], compact layer of fibers located between the retina and vascular choroid, which is semipermeable and allows the transportation of nutrients and other necessary macromolecules from underlying blood vessels to the retina. Directly on Bruch's membrane is a monolayer of hexagonally shaped RPE cells that maintain the photoreceptors. All ionic exchange and metabolic traffic from the neural retina and RPE to the choroid capillaries, and vice versa,

must traverse Bruch's membrane [4]. One theory postulates that, in AMD, RPE cells stop degrading the waste products of photoreceptors properly, leading to the accumulation of wastes in Bruch's membrane [2]. As a result, Bruch's membrane may become thickened and change its composition, lowering permeability to nutrients and macromolecules, which can cause the dysfunction of RPE cells and loss of photoreceptors, ultimately resulting in severe vision loss.

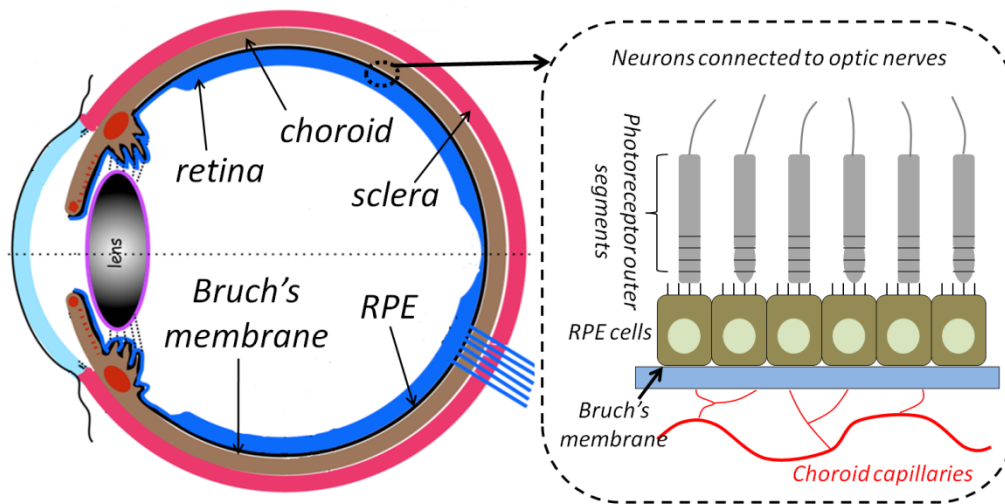


Figure 4-1: Schematics of the Bruch's membrane and RPE cells

In this chapter, first there will be a brief review of current technologies for the therapy of AMD in Section 4.1. In Section 4.2, a mesh-supported submicron parylene membrane will be proposed. A series of experiments have been done to demonstrate its feasibility as an artificial Bruch's membrane. The surgical procedure and current clinical trials will be described in Section 4.3. A 3D RPE cage will be discussed in Section 4.4. The major advantage of the RPE cage is its capability to restrict the undesirable RPE cell migration after implantation.

4.2 Existing Therapies for AMD

Replacement of the diseased RPE cells is a potential treatment of AMD [1–4]. A number of donor cell types have been studied for transplantation, including fresh, cryopreserved, cultured, or immortalized RPE cells of animal or human origin, iris pigmented epithelial cells, stem cells, retina cells, photoreceptors, and Schwann cells [4]. Irrespective of the cell type, the adhesion of the cells to Bruch’s membrane is a crucial step in the success of the transplantation procedure. However, attempts to directly transplant healthy RPE cells have been unsuccessful because the transplanted cells usually had poor adherence to the native Bruch’s membrane and failed to form a monolayer on it [2,4].

An alternative method is to transplant the *in vitro* cultured RPE cells as a pre-formed monolayer on a substitute substrate, which has been demonstrated to be a much more promising approach [1–4]. In order to be a functional replacement substrate, this artificial Bruch’s membrane must be biocompatible and possess similar permeability to a human Bruch’s membrane. It should be mechanically robust to survive the handling or implantation process. Moreover, it must also support the adherence and growth of RPE cells with similar characteristics to RPE cells *in vivo*.

Substrates made of various materials have been studied as artificial Bruch’s membranes, such as poly(DL-lactic-*co*-glycolic acid) (PLGA) [5], polydimethylsiloxane (PDMS) [6], poly(methyl methacrylate) (PMMA) [7], polyester membrane [9], human lens capsule [1], collagen type I [2,3], elastin-like recombinamers [8], and other synthetic degradable or non-degradable polymers. Most of these membranes are naturally

semipermeable for the nutrient transportation. For the membranes made of non-permeable materials, further machining is required to create through-holes. For example, the PMMA scaffold was patterned by photolithography and dry etch to have 11- μm -diameter holes [7].

Although a number of substrates have been demonstrated as potential candidates for artificial Bruch's membranes, many of them still have some shortcomings. Some biological tissues, such as lens capsule and collagen I, are difficult to handle. For example, it is difficult to obtain a large, continuous piece of lens capsule without holes or tears [1]. The 2.4- μm -thick collagen film has to be prepared on a Teflon support and this Teflon support needs to be removed before implantation, which increases the complexity of handling and may cause contamination [2]. The biodegrading substrates have the potential to leave the cells without appropriate support and the potential to cause adverse tissue reactions at the site of the transplant as they degrade [4]. Moreover, for the synthetic degradable materials, whether their breakdown products and removal influence the already compromised retina-choroid complex is still unclear [6]. Although PDMS with proper surface treatment could support RPE cell growth, ultrathin PDMS with thickness comparable to Bruch's membrane is difficult to make [6].

4.3 Parylene Artificial Bruch's Membrane

4.3.1 Submicron parylene: A potential candidate

Due to the unsolved problems with the existing substitute substrates, we are looking into the possibility of building a parylene substrate with better performance. Although parylene is widely used as a barrier protective material, we have shown in

Section 2.3 that when the thickness of parylene is reduced into the submicron range, it becomes semipermeable to macromolecules. In Section 2.3, the diffusion coefficients of macromolecules in submicron parylene have been calculated. Here we compare the permeability of 0.15 μm and 0.30 μm parylene to healthy human Bruch's membranes (aged 9–87 years) [10], and two previously reported substitute materials (lens capsule [1] and collagen [2]) in terms of diffusion flux.

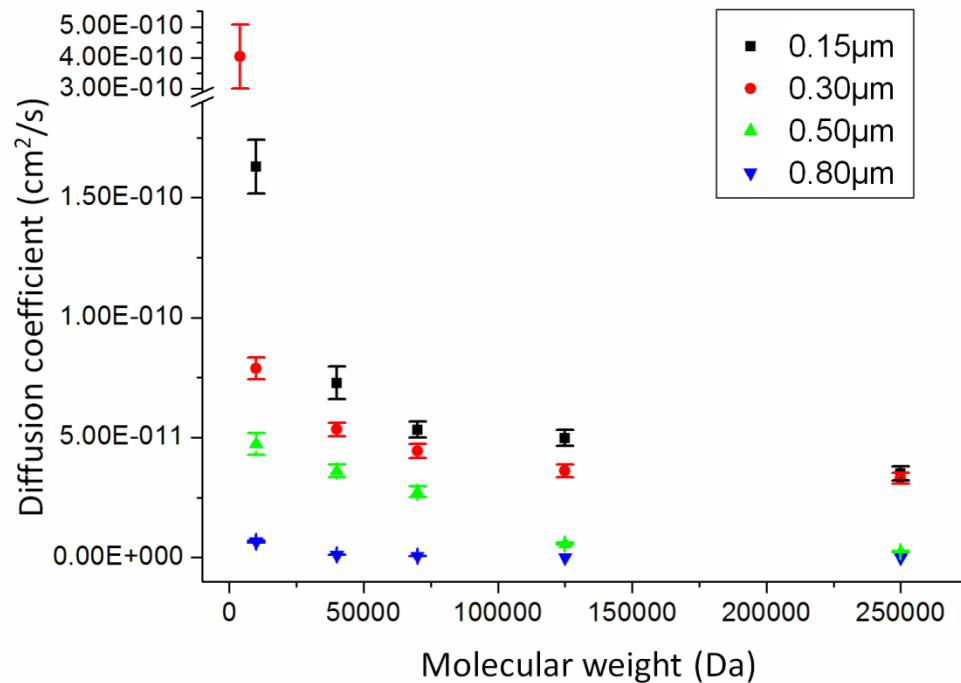


Figure 4-2: Comparisons of the permeability of 0.15 μm and 0.30 μm parylene, human Bruch's membranes, lens capsule, and collagen film in terms of the diffusion flux. The values of flux are evaluated assuming the same concentration difference across the membrane, denoted as ΔC in the y-axis.

Fig. 4-2 shows that parylene with a thickness between 0.15–0.30 μm has very similar permeability to human Bruch's membrane. In our work, 0.30 μm ultrathin

parylene is selected as the diffusion zone of the artificial Bruch's membrane. It has been reported that the MW exclusion limit of Bruch's membrane is 200 KDa [11]. Another report claimed that molecules as large as 500 KDa are able to traverse Bruch's membrane (although very slowly) [10]. We have shown in Section 2.3 that the molecular weight (MW) exclusion limit of 0.30 μm is 1008 KDa, which will theoretically allow the passage of macromolecules exemplified by carrier proteins, such as the delivery of vitamins, metals, lipids, etc. [10]

4.3.2 Perfusion cell culture experiments

To further examine permeability, perfusion cell culture experiments were done with two kinds of RPE cells (H9-RPE and ARPE-19). Human embryonic stem cells (H9) were spontaneously differentiated into H9-RPE cells, which were cultured in serum-free medium (X-VIVO 10, Lonza). ARPE-19 cells were taken from the spontaneously immortalized adult RPE cell line, and were cultured in DMEM/F12 medium (1:1) supplemented with 2 mM glutamine (Sigma) and 10% fetal bovine serum (Irvine Scientific). Before cell seeding, we coated the mesh-supported submicron parylene membrane (MSPM) (with 0.30 μm ultrathin parylene) with Matrigel (BD Biosciences) to further enhance cell adherence. H9-RPE and ARPE-19 cells were first cultured on MSPMs (with 0.30 μm ultrathin parylene) for three days. Perfusion cell culture experiments were then carried out by clamping the MSPMs in between two blind-well chambers according to the method described by [2], with the cultured cells exposed to the contents of the top chambers. Either culture medium or PBS was filled in the chambers and the cells were further cultured for 12 hrs (H9-RPE) or 36 hrs (ARPE-19) under three different conditions (medium-medium, PBS-medium, and PBS-PBS) (Fig. 4-3(a)). The

viability of RPEs was determined by Calcein-AM/propidium iodide (PI) staining (Fig. 4-3(c)–(h)). For the PBS-medium (P-M) condition, since sufficient nutrients could diffuse from the bottom to upper wells, the viability was comparable to the medium-medium (M-M) condition (positive control). However, due to the depletion of nutrients, the viability was considerably lower for the PBS-PBS (P-P) condition (negative control) (Fig. 4-3(b)). Interestingly, as observed in Fig. 4-3(c)–(h), for both the medium-medium and the PBS-medium conditions, H9-RPE cells showed good adherence on the parylene substrate. In contrast, for the PBS-PBS condition, even viable cells were in spherical shape with poor adherence.

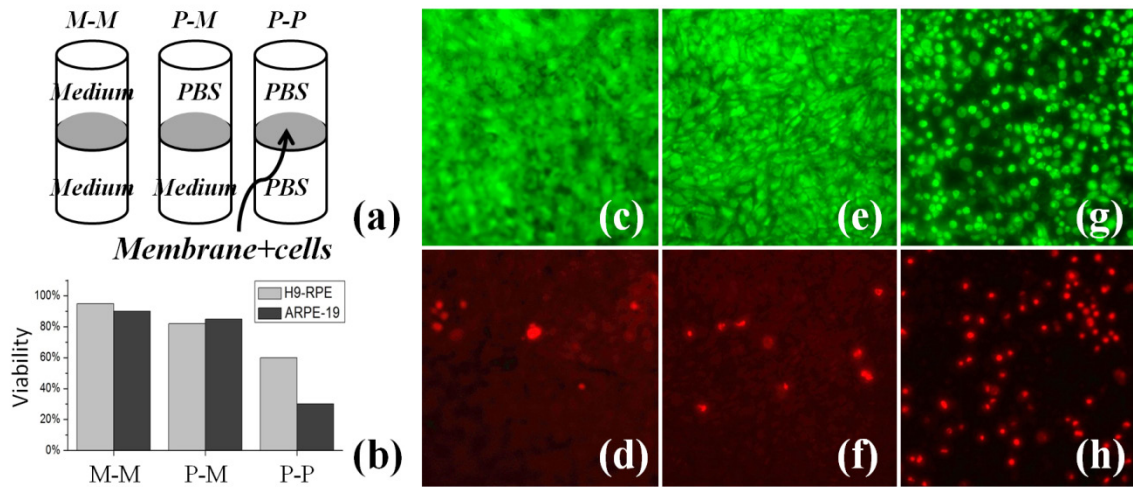


Figure 4-3: Perfusion cell viability tests. (a) blind-well perfusion setups. (b) measured viability for H9-RPE and ARPE-19 cells. (c) and (d) images of live (green) and dead (red) H9-RPE cells for medium-medium condition (M-M). (e) and (f) images of live and dead H9-RPE cells for PBS-medium condition (P-M). (g) and (h) images of live and dead H9-RPE cells for PBS-PBS condition (P-P)

4.3.3 Mesh-supported submicron parylene

As an artificial Bruch's membrane, the parylene substrate should possess both large permeability and good mechanical strength. However, submicron parylene membrane itself is fragile. In Section 2.2.2, we propose a strategy of enhancing the mechanical strength of the submicron parylene by designing a composite membrane with a thick parylene frame. Here we propose a mesh-supported submicron parylene membrane (MSPM).

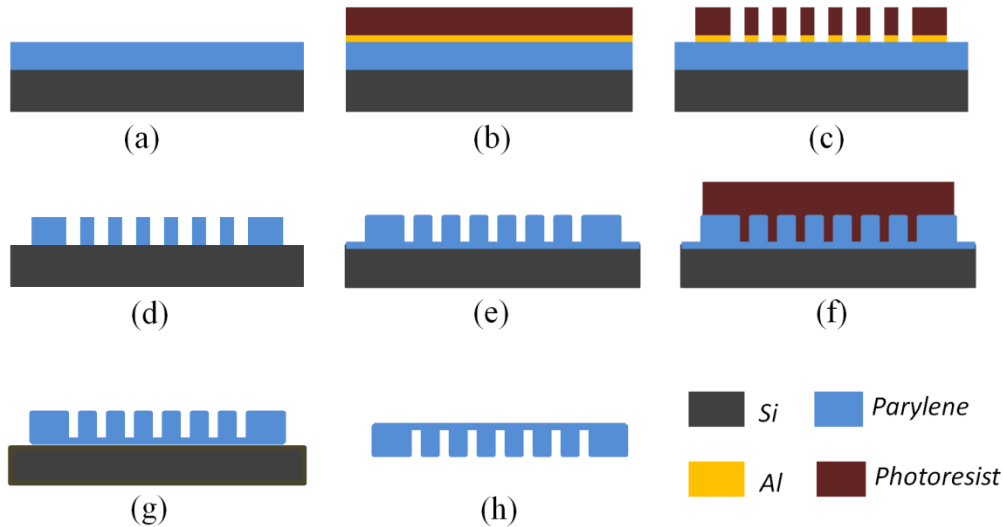


Figure 4-4: Fabrication process of the MSPM. (a) deposition of a 6 μm parylene on HMDS treated silicon. (b) aluminum coating followed by photoresist spin-coating. (c) lithography and wet-etching of aluminum to form the mask for parylene etching. (d) the mesh frame was etched by RIE. (e) deposition of a 0.30 μm parylene. (f) the MSPM was covered with photoresist after the second lithography. (g) the contour of the MSPM was formed by RIE. (h) the membrane was peeled off and flipped over.

The fabrication process (Fig. 4-4) of the MSPM started with a 6- μm -thick frame (i.e., structural) parylene deposition on the hexamethyldisilazane (HMDS) treated silicon. All the parylene depositions in this work were performed with a SCS PDS 2035CR

parlylene coating equipment (Specialty Coating Systems). The temperature settings were 180°C and 690°C for the vaporizer and furnace, respectively. The set-point of chamber pressure during deposition was 35 mTorr. HMDS coating was used because it reduces the adhesion between parlylene and silicon. Aluminum was then deposited as the parlylene etching mask. Following lithography, wet-etching of aluminum, and reactive ion etching (RIE) with oxygen plasma, parlylene was patterned with circular through-holes as a mesh frame. After RIE, diluted hydrofluoric acid (HF) was used to clean the residues inside the holes. A submicron parlylene film (e.g., 0.15–0.80 μm) was then deposited on the mesh frame. The second lithography was done to cover the whole device with photoresist. The contour of the device was formed by etching away ultrathin parlylene in the undesirable regions. Finally the whole membrane was peeled off and flipped over. Both sides of the membrane were treated with low-power oxygen plasma (power: 50 W, chamber pressure: 200 mTorr, duration: 1 min) for better cell adherence. Fig. 4-5 shows the SEM images of the front side, back side, and cross section of the MSPM.

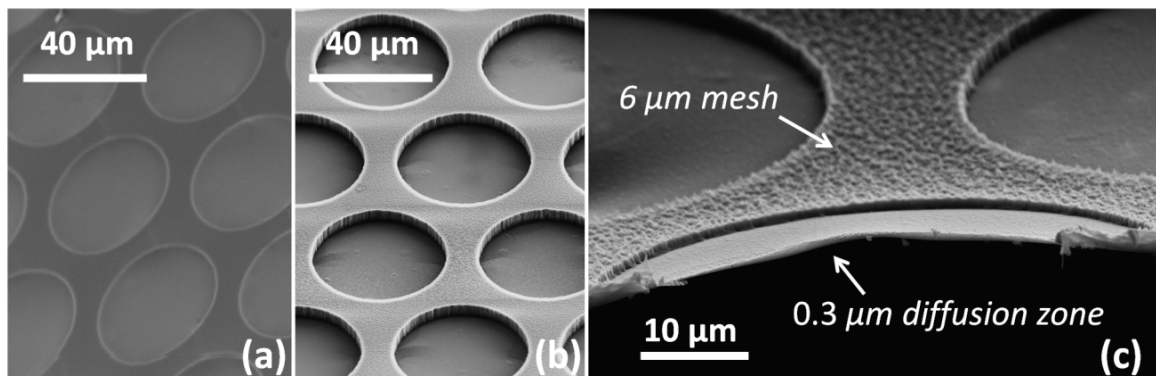


Figure 4-5: SEM images of (a) the front side, (b) the back side, and (c) the cross section of a MSPM with 0.30 μm ultrathin parlylene

4.3.4 Mechanical optimization

A “thin parylene ratio” (TPR) was defined as the ratio of the overall equivalent area of submicron parylene to the area of the entire MSPM. MSPMs (with 0.30 μm ultrathin parylene) with different TPRs were designed by varying three parameters, including the diameter of the circular submicron region (d), the separation between two circles (s), and the arrangement of these circles (i.e., rectangular or hexagonal arrangements) (Fig. 4-6(a)). The mechanical properties of these MSPMs were characterized by membrane deflection tests under different N_2 pressures (Fig. 4-6(b)). The exposed membrane was circular with a 1.8 mm diameter. The deflection and breakdown of the MSPMs were observed and evaluated under a microscope.

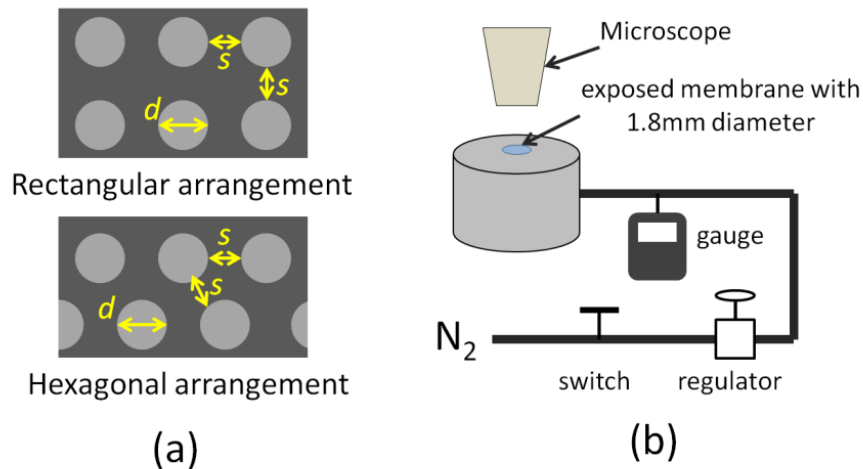


Figure 4-6: Membrane deflection experiment. (a) illustration of the MSPMs with the submicron regions in rectangular and hexagonal arrangements. (b) schematic of the membrane deflection setup

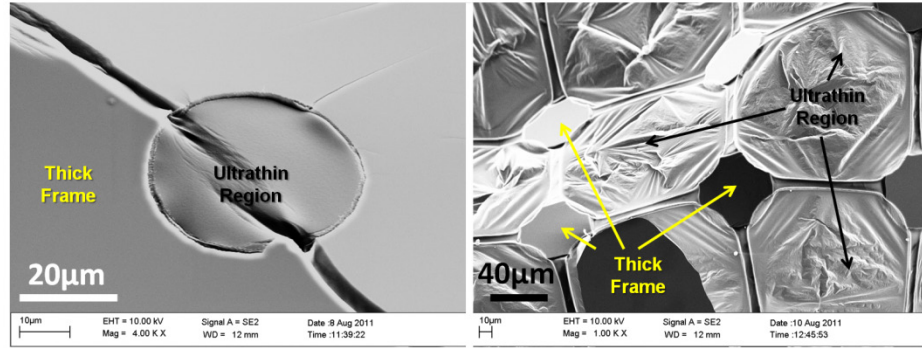


Figure 4-7: A wrinkled MSPM (a) and a broken MSPM (b)

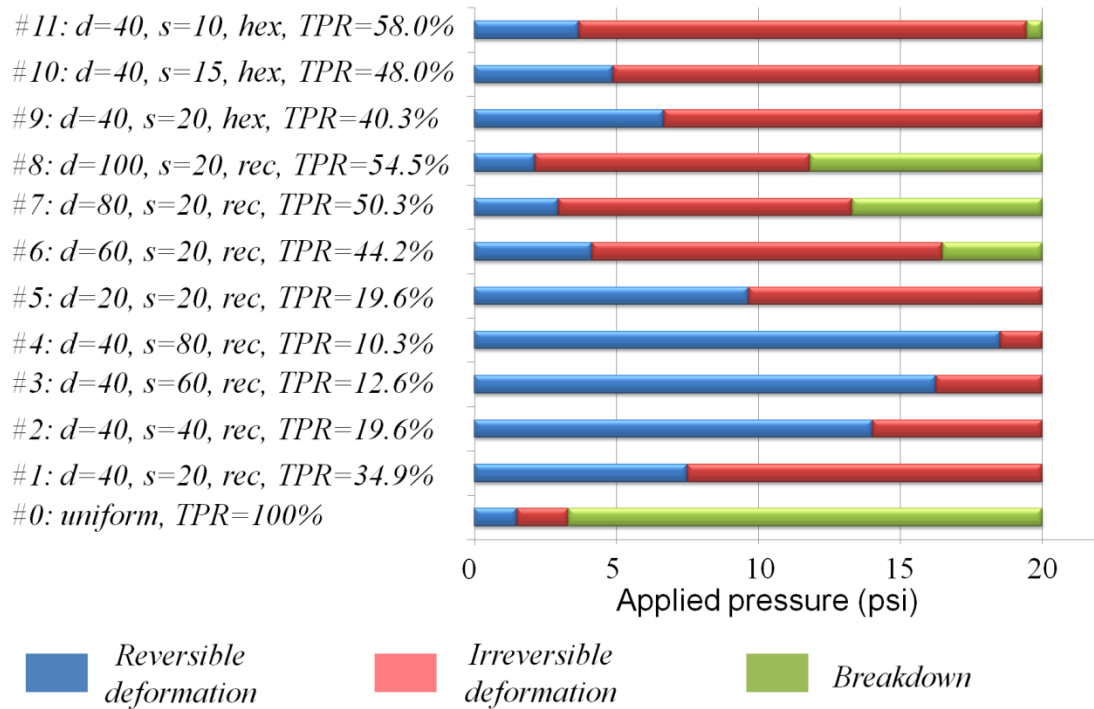


Figure 4-8: Yielding pressures and breakdown pressures for different MSPMs. d is the diameter of each submicron region and s is the separation between two submicron regions. The units of the values of d and s are all in μm . Measured pressure range was 0–20 psi. (hex: hexagonal arrangement, rec: rectangular arrangement)

The mechanical properties of the MSPMs were evaluated in terms of their yielding pressures and breakdown pressures. The yielding pressure was defined as the

minimum pressure that could create wrinkles and irreversible deformation. The breakdown pressure was recorded at the moment the membrane broke. Fig. 4-7 shows the wrinkled and broken MSPMs. The submicron parylene could be stretched a lot before breakdown. From the testing results in Fig. 4-8, several conclusions can be drawn. First, compared to the uniform 0.30 μm parylene, the MSPMs show improved mechanical strength. Secondly, increasing the area of each submicron region or decreasing the separation between two submicron regions will result in weaker mechanical strength. Finally, by comparing #1 and #9, as well as #6 and #10, we found that the hexagonal arrangement of submicron regions is more advantageous than the rectangular arrangement, because better mechanical strength can be achieved for MSPMs with even larger TPRs. In our current design (#11), the separation between each two circular submicron regions is reduced to 10 μm . This separation is less than the average diameter of adhering RPE cells, so the diffused nutrients can reach every cell. Hexagonal arrangement of the submicron regions is adopted so a large TPR ($\sim 58\%$) is achieved without losing mechanical strength. In on-going surgical trials on rats, not a single broken MSPM has been found during handling and culturing experiments.

4.3.5 RPE cell culture on the MSPM

To validate that the MSPM can support RPE cell growth with *in vivo*-like characteristics, H9-RPE cells were seeded on the Matrigel-coated MSPM (with 0.30 μm ultrathin parylene) and cultured for one month. One day after seeding, cells were well adhered and spreading on the substrate (Fig. 4-9(a)). After one week, cells were growing to confluence (Fig. 4-9(b)). After four weeks, cells formed hexagonal shapes and some

of them became pigmented (Fig. 4-9(c)). H9-RPE cells cultured on the MSPM were fixed in 4% paraformaldehyde and stained with the anti-ZO-1 antibody (Millipore) to visualize the morphology and tight junctions among the cells. The anti-Zo-1 staining of cells cultured for four weeks further demonstrated their hexagonal shapes and intercellular tight junctions, which are signs of typical epithelial-like morphology (Fig. 4-9(d)). The formation of microvilli on the apical surface of RPE cells is an important characteristic of their polarization and functionality.

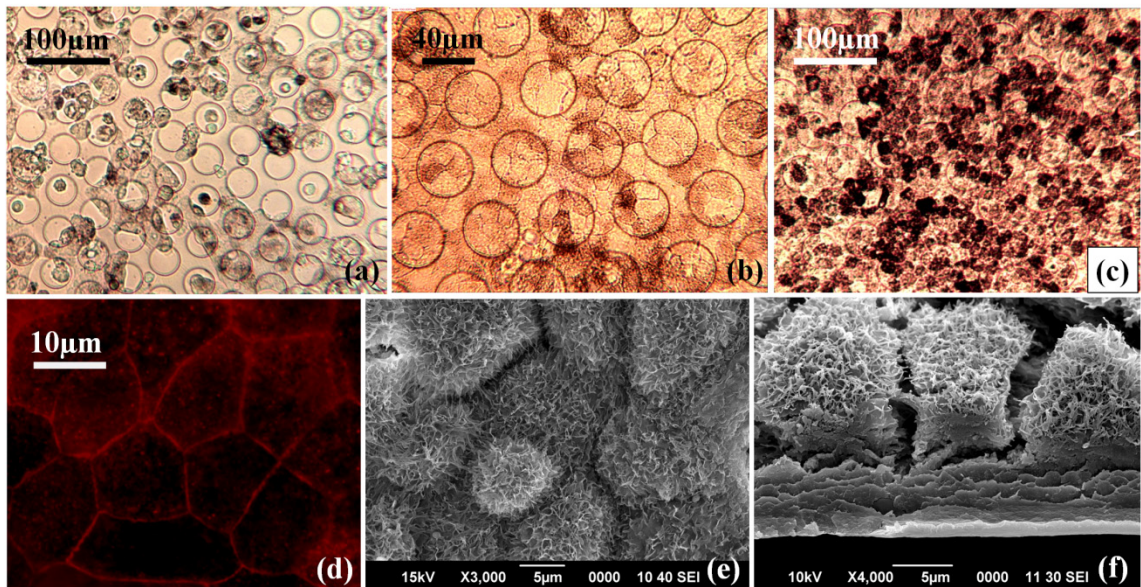


Figure 4-9: H9-RPE cell culture on the MSPM. (a) one day after seeding, cells adhered and spread on the MSPM. (b) after one week, cells became confluent. (c) after four weeks, cells started to show pigmentation. (d) anti-Zo-1 staining shows cells with hexagonal shapes and the tight junctions among cells. (e) and (f) the top and cross-sectional SEM images show the formation of microvilli on well-polarized cells.

After the fixation, dehydration, and conductive coating of the samples, the samples were ready for SEM imaging. Both the top view (Fig. 4-9(e)) and cross-

sectional views (Fig. 4-9(f)) of the SEM images of cells cultured for four weeks show clear microvilli. Therefore, the RPE cells cultured on the MSPM are well polarized and able to develop microvilli for interdigitation with the photoreceptor outer segments.

4.3.6 Comparison of MSPM and porous membrane

Both the commercial track-etched polyester porous membrane [9] and the micromachined PMMA porous membrane (with 11- μm -diameter pores) [7] have been considered as substitute substrates. Nutrients can be transported through the pores to nourish the cells. However, most of the porous membranes have very low open factors (i.e., the ratio of opening area to the overall membrane area). Once cells have partially migrated into the pores, nutrient transportation could be significantly reduced in the non-porous regions. Moreover, the porous topologies are not like the real Bruch's membrane, which may influence cell adherence and morphology. In contrast, the front side of our MSPM is flat (Fig. 4-5(a)), which contributes to the *in vivo*-like RPE monolayer. The large TPR (58%) ensures an even distribution of nutrient transportation.

To validate this conclusion, control experiments were done with parylene porous membrane and the MSPM. The fabrication process flow of the parylene porous membrane was very similar to that of the 2D pore filter. To prevent cell migration into the holes, the diameter of the hole was only 1 μm . It was very difficult to directly etch such a small hole in parylene membrane thicker than 5 μm . Alternatively, we first created large holes with diameter of 5 μm , and then used the fill-in technique to deposit another 2 μm thick parylene onto the porous membrane to reduce the diameter to 1 μm .

Due to the conformal coating property of parylene, the shape and uniformity of the holes were good (Fig. 4-10).

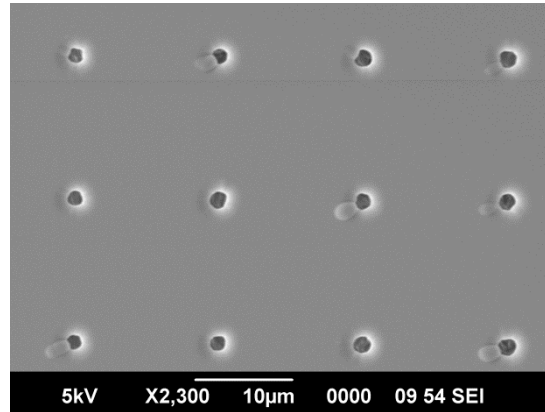


Figure 4-10: Porous parylene substrate with through holes (1 μm in diameter)

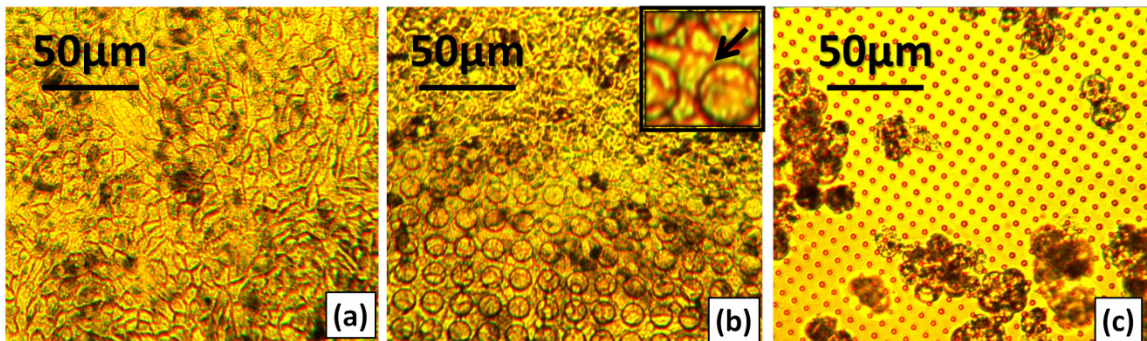


Figure 4-11: Comparisons of the morphologies of RPE cells on different substrates. *In vitro* culture of H9-RPE cells (a) in tissue culture dish, (b) on the MSPM and (c) on a porous parylene membrane with 1 μm pores. The inset of (b) shows RPE cells have tight junction and hexagonal shapes (arrowed).

Fig. 4-11 compares the cell morphologies when cultured on different substrates. H9-RPE cells developed into hexagonal shapes (Fig. 4-11(b) inset) and formed a compact monolayer on the MSPM, which was similar to the cells cultured in a tissue culture dish (Fig. 4-11(a)). However, due to the porous topology, cells cultured on porous parylene

membrane with 1- μm -diameter pore arrays showed much worse adherence and developed abnormal, multilayer morphology (Fig. 4-11(c)).

4.4 Animal Trials

4.4.1 The “lollipop” design

In our current animal trials on rats and pigs, the MSPMs are cut into rectangular shapes with curved edges and rounded corners to match the shapes of the macular. To make the handling and operation easier during device manufacturing, cell culture, a handling stem is also added to device, making the total shape of the device look like a “lollipop”. Fig. 4-12 shows the current designs of the rat’s and pig’s lollipops and their dimensions. To differentiate the front and back sides, there is a titanium mark on the upper-left corner on the rat’s lollipop. Titanium is considered to be non-toxic. Moreover, this metal marker is ultimately encapsulated inside two parylene layers, so it should not cause any problem after implantation. For the pig’s lollipop, since its dimension is relatively large, an asymmetrical bump is made on the stem, which helps to distinguish the front and back sides.

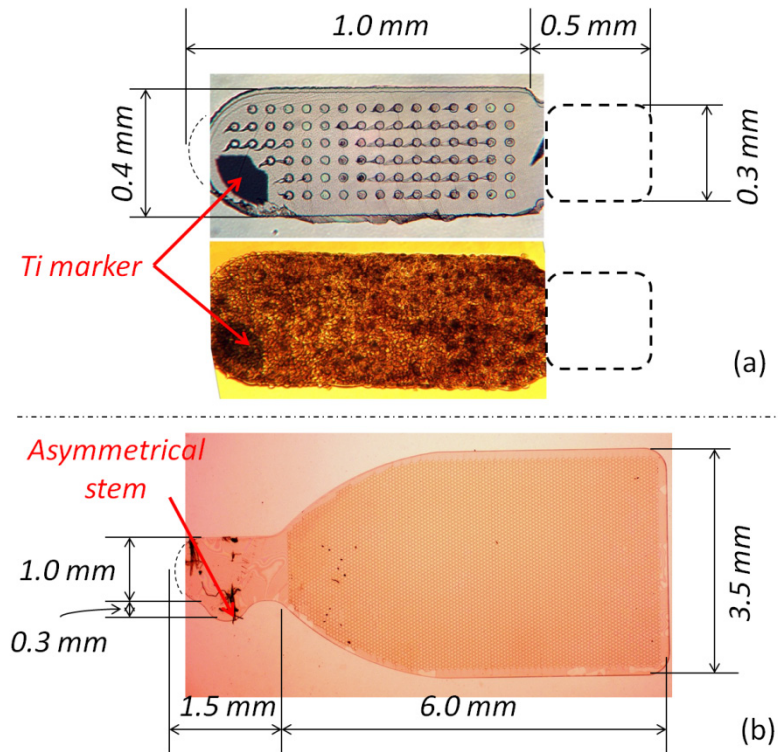


Figure 4-12: Current designs of (a) rat's and (b) pig's lollipops and their dimensions

4.4.2 Mechanical implantation platform

During the implantation process, the surgeons found it was difficult to directly insert the lollipop into the sub-retina region, since friction could cause the lollipop to be seriously curved. To overcome this problem, we proposed a novel mechanical implantation platform device.

The platform device was made of parylene (10 μm thick) containing SU-8 barriers (30 μm high) arranged along the edges in the shape of 'U' (Fig. 4-13). The discontinuous barriers ensured that the entire platform was still flexible, and would not cause retinal damage during the implantation. The space inside the barriers acted as the "substrate loading chamber" where the lollipop for implantation was placed.

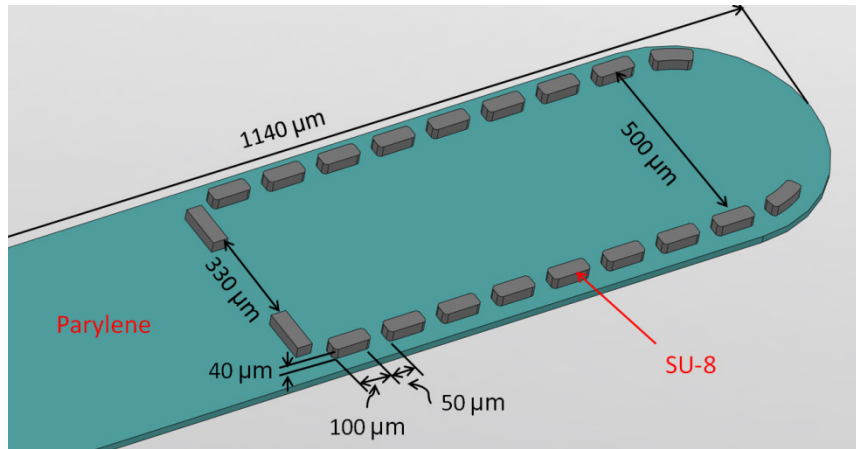


Figure 4-13: Diagrammatic sketch of the implantation tool. The device consisted of a parylene plate (a) and SU-8 barriers (b) arranged in the shape of a 'U'. The lollipop for implantation was placed in the middle of the 'U'-shaped area (substrate chamber).

Here is a brief description of the surgical process [12]: After the conjunctiva was opened, extra ocular muscles were maintained on traction for eyeball fixation. A small incision (approximately 1–1.2 mm) was cut trans-sclerally at the temporal equator of the host eye, until the choroid was exposed. Puncture of the anterior chamber released some of aqueous humor to reduce intraocular pressure. Using a 32 gauge steel needle, about 10 μ l of balanced salt solution (BSS) was injected into the subretinal space to create a focal retinal detachment. Using a fine scissor, the choroid was cut while the retina remained intact. During implantation, the lollipop containing hESC-RPE cells was loaded on the platform device with the surface of the lollipop coated with cells facing upward. Using a fine forceps, the platform (along with the lollipop) was gently pushed into the subretinal space through the choroidal incision. During this process, the cell-coated surface of the lollipop always faced the vitreous side of the retina. The lollipop was released into the subretinal space by holding it in place using a forceps and gently pulling out the platform device from the incision. Once the placement of the implant was confirmed based on

microscopic fundus examination, the incision was sutured (10/0 nylon surgical suture, REF 03199, S&T, Neuhausen, Switzerland) and antibiotic drops were applied on the eye. The animals were allowed to recover in a thermal care incubator.

The lollipop could be easily loaded inside the substrate chamber (between the vertical barriers). The barriers prevented the implant moving away from the chamber during the process of implantation. After surgery, the retina remained intact and no vitreous leakage was observed [12]. No signs of subretinal hemorrhage or lens damage were apparent [12]. SD-OCT examination performed in RCS rats at one week after implantation demonstrated subretinal placement of the implant and reattachment of the retina [12]. All these evidence support the capability of this mechanical platform implantation tool to facilitate the surgery.

4.4.3 Microfluidic implantation tool

Another type of implantation tool is a parylene/SU-8 surgical inserter (Fig. 4-14 and Fig. 4-15). Unlike the previous tool, based largely on mechanical release of the lollipop using forceps, this microfluidic tool uses liquid injection to flush out the lollipop. The fabrication process flow of this microfluidics inserter is shown in Fig. 4-14. Briefly, a 10- μm -thick parylene was deposited on an HMDS or photoresist coated silicon wafer. A 20 μm -thick photoresist was then spin-coated and patterned as the sacrificial layer. We used the first SU-8 layer to construct the channel and chamber, and used the second SU-8 layer to form a $\sim 25\text{-}\mu\text{m}$ -high protection barrier wall on top. The outline of the inserter was defined by the laser cutting of the parylene substrate. Finally, the whole structure

was released (acetone was used to remove sacrificial photoresist), and the fabricated device is shown in Fig. 4-15.

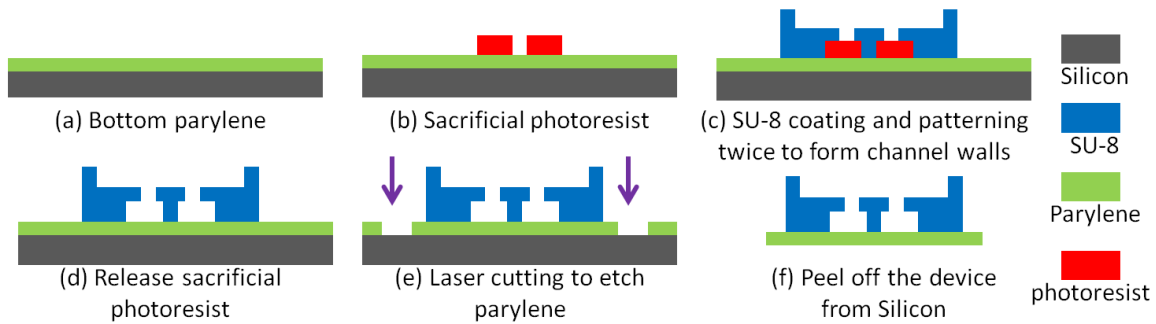


Figure 4-14: Fabrication process flow of the microfluidic implantation tool

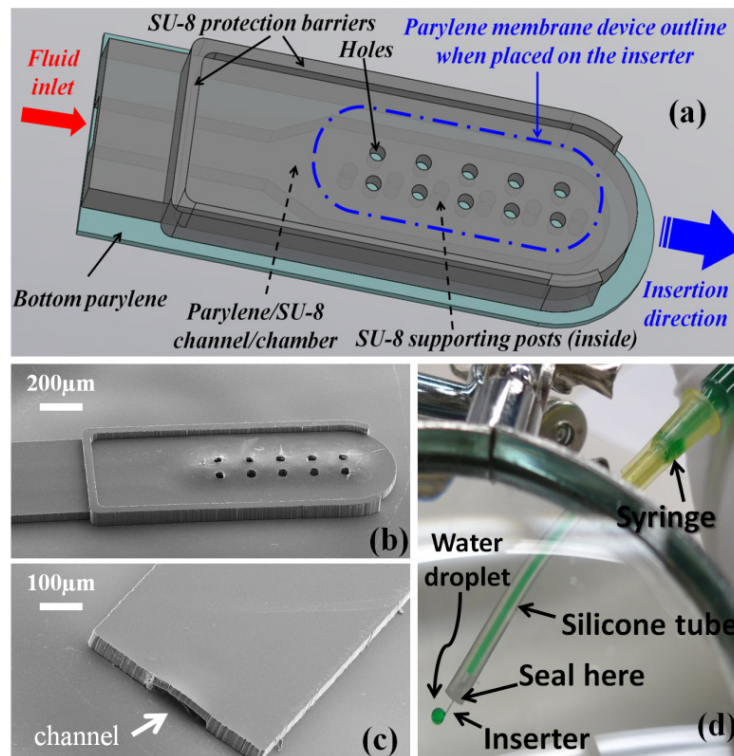


Figure 4-15: The microfluidic implantation tool. (a) schematic and working principle. (b) and (c) SEM images of the tip and tail (taken before laser cut). (d) assembling and sealing method

The lollipop can be fitted onto the top cavity due to parylene-to-parylene stiction. Surrounding SU-8 barrier walls were able to protect the lollipop and RPE cells from being damaged during the implantation. Fig. 4-15(d) shows that the inserter was packaged into a silicone tube and connected with a syringe. After insertion, balanced salt solution was injected into the tail of the SU-8 channel/chamber and flushed out of the holes to release the lollipop, as demonstrated in Fig. 4-15(d).

The cell culture, retina cut, and detachment steps were very similar to the previous description in Section 4.4.2. Fig. 4-16 shows the implantation procedure of a lollipop with cultured cells into a rat's eye. The lollipop was first placed in the protective cavity of the implantation tool due to parylene-SU-8 stiction. Then the implantation tool was inserted into the incision on the retina, and the lollipop was released at the sub-retinal region by injecting the balanced salt solution into the microchannels in the tail. During the implantation process, no damage of the submicron membrane or scratching of the RPE cells was observed.

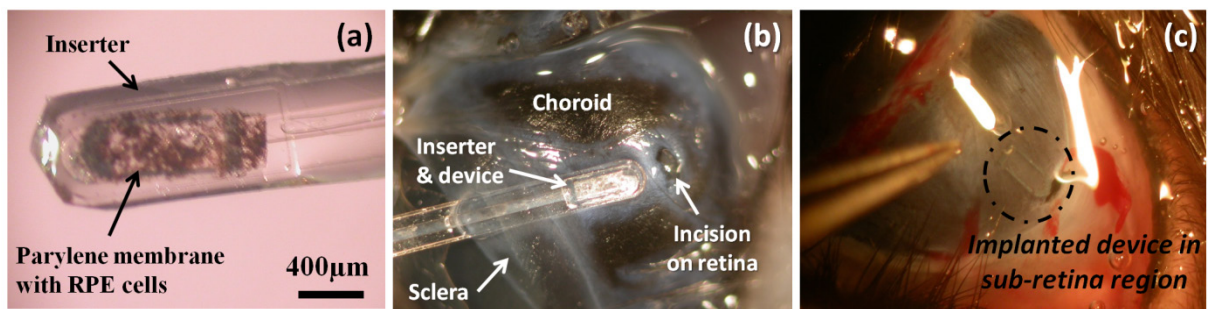


Figure 4-16: Implantation of a lollipop device into a rat's eye. (a) fit the lollipop with cultured RPEs onto the inserter. (b) insert the lollipop. (c) the lollipop implanted into the sub-retinal region. The outline of the device is highlighted with a titanium ring just for easy observation.

4.4.4 Post-implantation staining and imaging

One week after implantation, the rat was sacrificed and hematoxylin-eosin (H&E) staining showed the histology of the sub-retinal region. Fig. 4-17 shows that the RPE cells still adhered well to the lollipop *in vivo*. Therefore, the lollipop functioned well as an artificial Bruch's membrane, supporting and nourishing the implanted RPE cells.

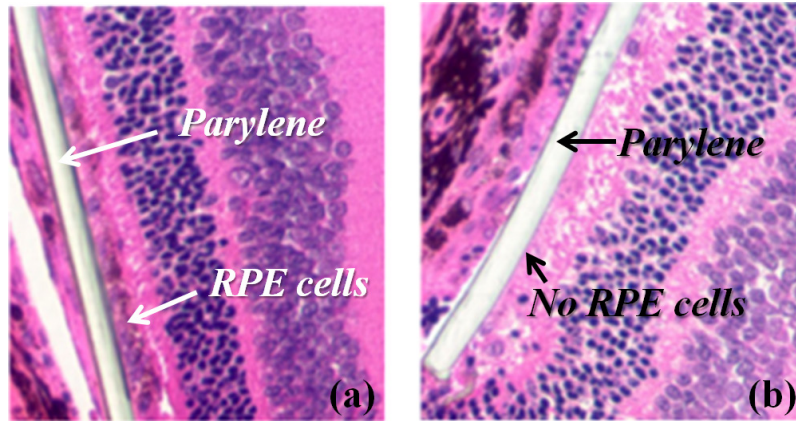


Figure 4-17: Hematoxylin-eosin staining one week after implantation. (a) MSPM with *in vitro* cultured RPE cells. (b) MSPM without RPE cells (control)

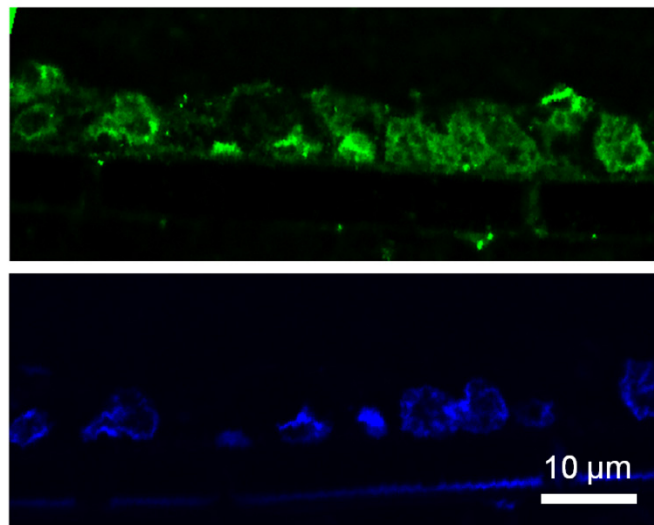


Figure 4-18: Immunofluorescence staining of the cross-sectional view of RPE cells

Besides the H-E staining, immunofluorescence staining was also done with the RPE cells implanted into the rat's eye. Fig. 4-18 shows the immunofluorescence staining of the cross-sectional view of RPE-65 cells growing on the parylene lollipop under a 40X magnification. It further confirms that the cells were in one monolayer with well-organized morphologies.

4.5 RPE Cage

4.5.1 Motivation

In previous sections, we mainly focused on the single-layer parylene substrate. Although current animal trials have already demonstrated its feasibility as an artificial Bruch's membrane, one potential problem is that the stem-cell-derived RPE cells may be able to migrate away from the substrate into other tissues. For example, if the cells migrate into the vitreous cavity, diseases such as proliferative vitreoretinopathy are likely to be induced, which may eventually result in serious retinal detachment [13].

To prevent possible cell migration, we propose here a 3D RPE scaffold (i.e., a cage) by assembling a parylene "fishnet" cover onto a mesh-supported submicron parylene bottom so that the cells are constrained inside the cage (Fig. 4-19). However, such a cage must satisfy several requirements. First, the cage's bottom must be as permeable as Bruch's membrane to allow nutrient transportation to nourish the cells inside. Secondly, the bottom must be mechanically robust for bending and stretching to survive handling and surgery. Moreover, the cage's top fishnet should be able to block cell migration but allow the microvilli to connect to the outside photoreceptors. Finally, under such constraints, cells should still be able to proliferate inside with normal

morphology and develop microvilli on the apical surface. The first two requirements are automatically satisfied since we continue adopting the previous MSPM design as the bottom layer. Therefore, in this section, we mainly focus on the design of the fishnet-like top cover, the assembling procedure, and the cell culture experiments inside the 3D RPE cage.

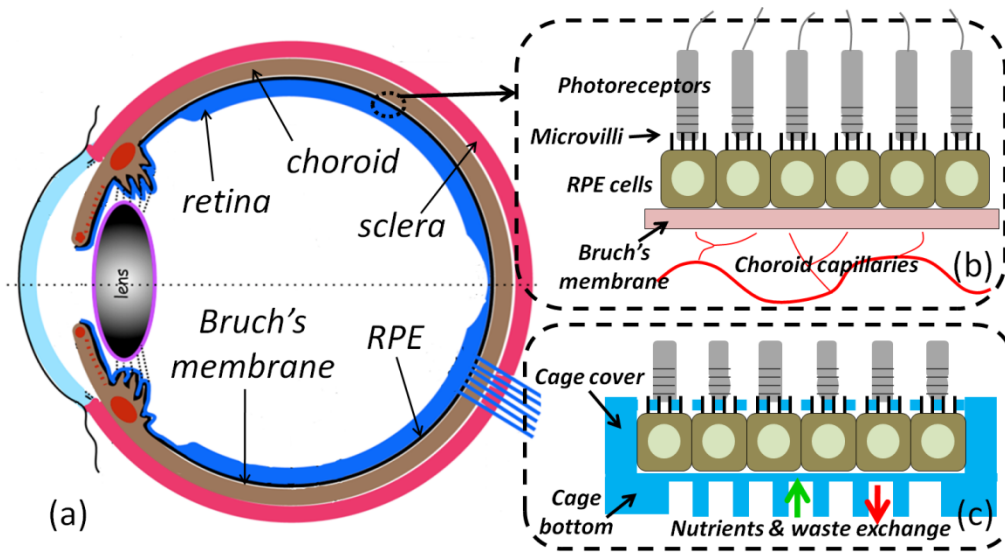


Figure 4-19: The concept of the RPE cage. (a) illustrations of the human eye, (b) Bruch's membrane, and (c) the schematic of the RPE cage

4.5.2 Cage design and fabrication

The design and fabrication process flow can be divided into two parts, the top cover and the bottom substrate. The design and fabrication of the bottom layer, the MSPM structure, have already been described in Section 4.3.3.

Once sealed inside a cage, RPE cells need to develop microvilli to connect to photoreceptors above (Fig. 4-19). Therefore, the cage's top cover should have a fishnet-like structure, exposing the microvilli but blocking migration of the whole cells. The gap

between the top and bottom was 6 μm , determined by the height of adhering polarized cells. To determine the size of the opening, cell migration experiments were carried out with the transwell setup. Porous parylene membranes with 8- μm -diameter and 4- μm -diameter holes were fabricated using the same method of fabricating 2D filters. Platelet-derived growth factor (PDGF) was added to the bottom well, which was a stimulus for cell migration (Fig. 4-20). Holes with 8- μm -diameter are widely used as a semi-barrier to evaluate RPE cell migration [13]. The percentage of migrated cells through 4- μm -diameter holes was significantly reduced (to 0.5%), which could be considered a good barrier.

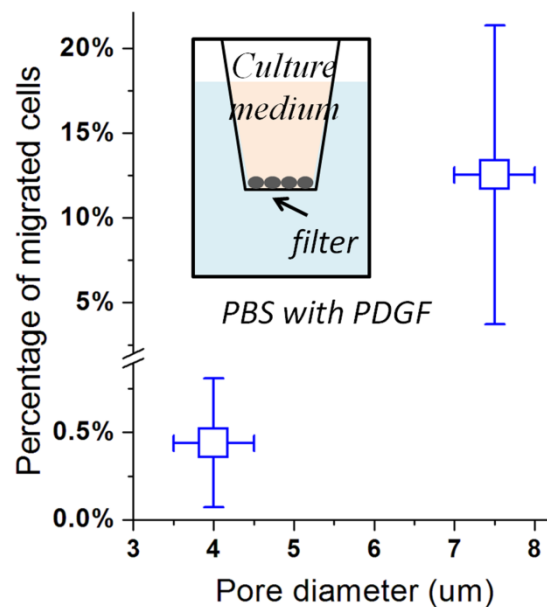


Figure 4-20: Cell migration experiments. The inset shows the transwell setup.

A 1- μm -thick fishnet with 4- μm -diameter holes was adopted as the cage's top cover. The edge of the cover was 6 μm thick, and was used as a spacer when the top was placed onto the bottom substrate. Fig. 4-21 shows the fabrication process of the top

cover. First, a 1- μm -thick parylene was deposited and patterned into a fish-net-like structure with through-holes. Then the porous region was covered with sacrificial photoresist. A 6- μm -thick parylene was then deposited. After patterning, only the edge of the second parylene layer remained. Finally the membrane was released and flipped over. Fig. 4-22 shows the SEM images of the top cover and a close-up view of the opening.

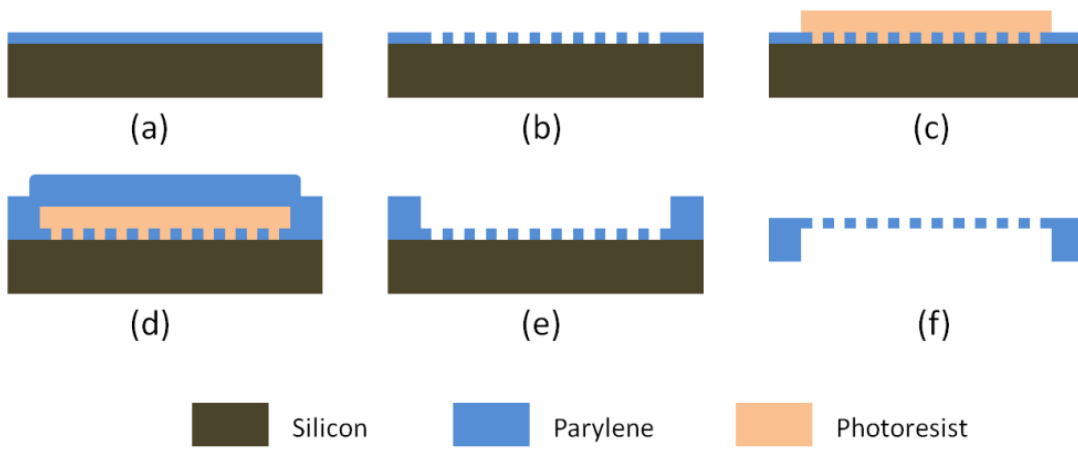


Figure 4-21: Fabrication process flow of the cage's top cover.

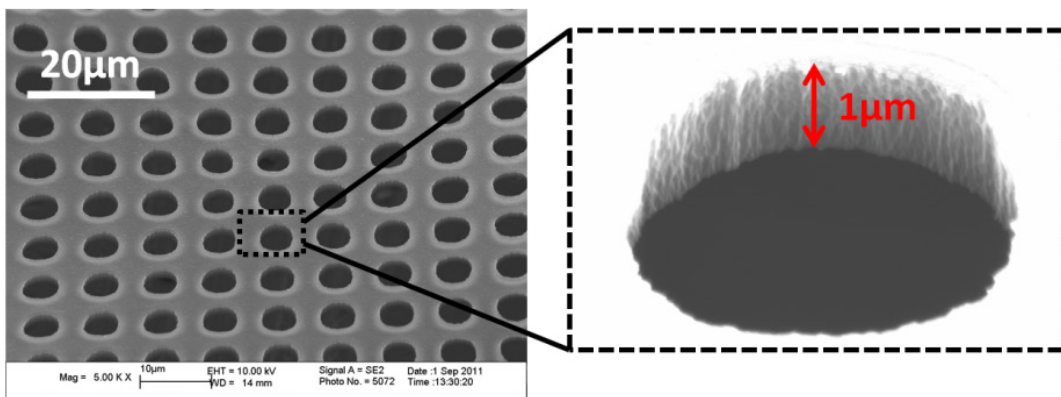


Figure 4-22: SEM image of the cover and a close-up view of the opening

4.5.3 Cage assembling

For the *in vitro* culture experiments, first a parylene ring was placed on the bottom substrate before cell seeding to protect the assembling region (Fig. 4-23(a)). After the cells evenly spread on the substrate and became confluent, the parylene ring was removed to expose the non-cell region (Fig. 4-23(b)). The cover was assembled to the non-cell region on the bottom using Matrigel (BD Biosciences) as “biological glue” (Fig. 4-23(c)). Undiluted Matrigel was used here because it was sticky enough to glue two parylene surfaces together in either wet or dry environment, especially after incubation at 37°C. The culturing process was continued until the cells were polarized with microvilli exposed through the top cover openings (Fig. 4-23(d)).

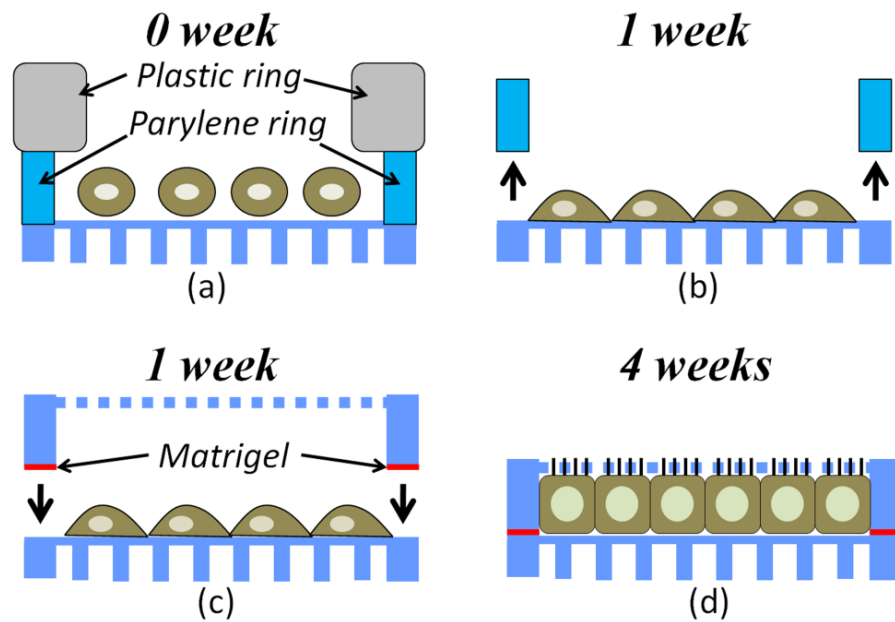


Figure 4-23: The assembling and operation procedure of the cage for *in vitro* cell culture

4.5.4 Preliminary results

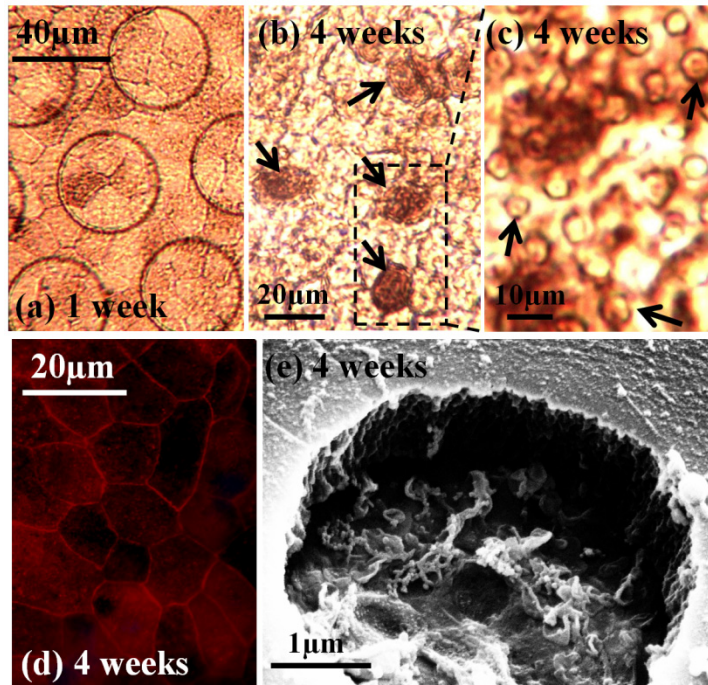


Figure 4-24: RPE cell culture experiments inside the 3D cage. (a) before placing the cover, cells adhered and spread on the bottom. (b) and (c) Cells were well polarized and started to show pigmentation (arrows). (b) photo focused on the cells and (c) photo focused on the cover openings (arrows). (d) immunostaining of the junction protein Zo-1 showing that cells formed a confluent monolayer and formed hexagonal shapes with tight junction. (e) cells remained under the cover and microvilli formed on the apical surface of polarized cells.

Fig. 4-24 shows the *in vitro* RPE cell culture results. One week after seeding, the cells became confluent on the bottom substrate (Fig. 4-24(a)). Then the top cover was placed on the bottom. After four weeks, cells started to become polarized and pigmented inside the cage (Figs. 4-24(b)-(c)). Cells were fixed and stained with anti-ZO-1 antibody (Millipore) to visualize the morphology and tight junctions among the cells. Fig. 4-24(d) indicates that the cells were in a monolayer with hexagonal shapes and intercellular tight

junctions, which are good signs of typical epithelial-like morphology. After the fixation, dehydration, and conductive coating of the samples, the cage was observed using SEM. Fig. 4-24(e) shows that a polarized cell was constrained inside the cage. The microvilli were clearly visible on the apical surface of the cell and exposed through the cover's opening. Once implanted, cells cultured inside the cage can form interdigitation with photoreceptors through these exposed microvilli.

4.6 Summary

In this chapter, we have successfully demonstrated the feasibility of using a mesh-supported submicron parylene membrane as an artificial Bruch's membrane for the stem-cell therapy of age-related macular degeneration. First, the MSPM possess similar permeability to native healthy human Bruch's membrane. Secondly, MSPM achieves a much better mechanical strength than the uniform submicron parylene. By optimization of the thin-part ratio, the mechanical strength can be further improved. Thirdly, Matrigel-coated MSPM allows good RPE cell adherences. Cells are able to proliferate with normal *in vivo*-like morphologies. More importantly, cells with good polarization can develop the microvilli on the apical surface, allowing the interdigitation between the RPE cells and photoreceptors. To prevent potential RPE migration, a parylene 3D RPE cage is proposed. Preliminary results on the RPE cage show that the RPE cells inside the cage can also develop into normal morphology and functions, despite the constricts of the top fishnet-like cover. All in all, the parylene substrate has the potential to be a promising candidate for stem-cell therapy of age-related macular degeneration.

4.7 References

- [1] C.J. Lee, J.A. Vroom, H.A. Fishman and S.F. Bent, Determination of human lens capsule permeability and its feasibility as a replacement for Bruch's membrane, *Biomaterials*, vol. 27, pp. 1670–1678, 2006
- [2] J.T. Lu, C.J. Lee, S.F. Bent, H.A. Fishman and E.E. Sabelman, Thin collagen film scaffolds for retinal epithelial cell culture, *Biomaterials*, vol. 28, pp. 1486–1494, 2007
- [3] G. Thumann, A. Viethen, A. Gaebler, P. Walter, S. Kaempf, S. Johnen and A.K. Salz, The *in vitro* and *in vivo* behavior of retinal pigment epithelial cells cultured on ultrathin collagen membranes, *Biomaterials*, vol. 30, pp. 287–294, 2009
- [4] C. Sheridan, R. Williams and I. Grierson, Basement membranes and artificial substrates in cell transplantation, *Graefe's Archive for Clinical and Experimental Ophthalmology*, vol. 242, pp. 68–75, 2004
- [5] G.G. Giordano, R.C. Thomson, S.L. Ishaug, A.G. Mikos, S. Cumber, C.A. Garcia and D. Lahiri-Munir, Retinal pigment epithelium cells cultured on synthetic biodegradable polymers, *Journal of Biomedical Materials Research*, vol. 34, pp. 87–93, 1997
- [6] Y. Krishna, C.M. Sheridan, D.L. Kent, I. Grierson and R.L. Williams, Polydimethylsiloxane as a substrate for retinal pigment epithelial cell growth, *Journal of Biomedical Materials Research*, vol. 80A, pp. 669–678, 2007
- [7] S. Tao, C. Young, S. Redenti, Y. Zhang, H. Klassen, T. Desai and M.J. Young, Survival, migration and differentiation of retinal progenitor cells transplanted on micro-machined poly(methyl methacrylate) scaffolds to the subretinal space, *Lab on a Chip*, vol. 7, pp. 695–701, 2007
- [8] G.K. Srivastava, L. Martin, A.K. Singh, I. Fernandez-Bueno, M.J. Gayoso, M.T. Garcia-Gutierrez, A. Girotti, M. Alonso, J.C. Rodriguez-Cabello and J.C. Pastor, Elastin-like recombinamers as substrates for retinal pigment epithelial cell growth, *Journal of Biomedical Materials Research Part A*, vol. 97A, pp. 243–250, 2011

- [9] C.J. Lee, H.A. Fishman and S.F. Bent, Spatial cues for the enhancement of retinal pigment epithelial cell function in potential transplants, *Biomaterials*, vol. 28, pp. 2192–2201, 2007
- [10] A.A. Hussain, C. Starita, A. Hodgetts and J. Marshall, Macromolecular diffusion characteristics of ageing human Bruch's membrane: Implications for age-related macular degeneration (AMD), *Experimental Eye Research*, vol. 90, pp. 703–710, 2010
- [11] D.J. Moore and G.M. Clover, The effect of age on the macromolecular permeability of human Bruch's membrane, *Investigative Ophthalmology & Visual Science*, vol. 42, pp. 2970–2975, 2001
- [12] Y. Hu, L. Liu, B. Lu, D. Zhu, R. Ribeiro, B. Diniz, P.B. Thomas, D. Hinton, M.S. Humayun, Y.C. Tai and B.B. Thomas, A novel approach for sub-retinal implantation of ultrathin substrates containing stem cell derived RPE monolayer, *Ophthalmic Research* (in press)
- [13] C.M. Chan, J.H. Huang, H.S. Chiang, W.B. Wu, H.H. Lin, J.Y. Hong and C.F. Hung, Effects of (-)-epigallocatechin gallate on RPE cell migration and adhesion, *Molecular Vision*, vol. 16, pp. 586–595, 2010

CHAPTER 5

CONCLUSIONS

My advisor, Dr. Yu-Chong Tai, often reminds me that the goal of PhD research is not just fancy ideas or good publications. The ultimate goal is to make a practical device, and bring it from the laboratory to the market. This is exactly what I have done in my PhD research, contributing to the commercialization of two parylene membrane biomedical devices. This thesis investigates into these two “practical devices”, the parylene membrane filters for cancer detection and the parylene artificial Bruch’s membrane for age-related macular degeneration (AMD). The word “practical” does not mean it is not scientifically innovative or theoretically profound. Every practical biomedical device is inspired by real needs, and backed by a series of theoretical studies

and experiments to demonstrate its feasibility, as well as by efforts in optimization and endeavors in clinical trials.

The motivation for creating the parylene membrane filters rises from the challenge of detecting extremely rare circulating tumor cells (CTC) from patient blood. We have developed a complete theory of time-dependent cell membrane damage under mechanical tension, as the theoretical background for the CTC capture. Four generations of filters have been created. In the end, the 2D slot filter is found to be the best design, with high capture efficiency, high viability, moderate enrichment, and high throughput. The 2D pore filter has been clinically tested in many hospitals and research centers in the US and Europe. It has already been commercialized by Tronics. During the commercialization process, the autofluorescence problem was successfully solved by using the results of the autofluorescence study.

The motivation for creating the parylene artificial membrane for AMD rises from the demand for a substrate that is micromachinable to have similar mechanical properties and permeability to the native human Bruch's membrane. For the first time, through a series of diffusion experiments, we show that parylene, which is widely believed to be a barrier material, can be semipermeable when its thickness is reduced to the submicron range. Sometimes the inspiration comes from the problems or challenges. For example, difficulty in the surgical process gave birth to the parylene-based implantation tools. The problem of the undesirable migration of stem-cell-derived retina pigment epithelial (RPE) cells gave birth to the idea of a 3D parylene cage. The parylene lollipops have been tested for clinical trials at the University of Southern California, the University of California at Santa Barbara, and the Geron Corporation.

Further improvements and optimizations are still needed for both devices. For example, precise control of the thickness of submicron parylene can be a challenge to be addressed in the future. However, the initial success at this time does give us confidence that the parylene membrane device can be a powerful tool for practical biomedical applications. It can also be anticipated that parylene MEMS technology will evolve into more interesting and useful membrane device derivatives in the near future.

